MODELING OF NUCLEATE BOILING DURING FREE JET IMPINGEMENT

EXPERIMENTAL STUDY AND MODELING OF NUCLEATE BOILING DURING FREE PLANAR LIQUID JET IMPINGEMENT

By

Ahmed M.T. Omar, BSc., MSc.

A Thesis

Submitted to the School of Graduate Studies

in Partial Fulfilment of the Requirements

for the Degree

Doctor of Philosophy

McMaster University

Doctor of Philosophy (2010) McMaster University

(Mechanical Engineering) Hamilton, Ontario, Canada

TITLE: **Experimental Study and Modeling of Nucleate Boiling During Free Planar Liquid Jet Impingement**

AUTHOR: Ahmed Mohamed Tawfik Omar B.Sc., M.Sc., (Mechanical Power Engineering Dept.) Cairo University, Cairo, EGYPT.

SUPERVISORS: Dr. Mohamed S. Hamed
Dr. Mamdouh Shoukri

NUMBER OF PAGES: 224 pages (i-xix, 1-205)

ABSTRACT

Determination of boiling heat transfer rate during liquid jet impingement cooling (LJIC) depends on the intensity of bubble generation that is dependent on many flow and surface conditions such as jet velocity, liquid temperature, and surface superheat. Many empirical correlations have been developed previously to determine the total wall heat flux under various LJIC flow velocity, subcooling and surface superheat. However, only few studies have been able to model the governing heat transfer mechanisms associated with LJIC. In many industrial applications, there is a need to determine the effect of any changes in processing parameters on the total rate of heat transfer. Mechanistic heat transfer models can fulfill such need and allow for efficient model modifications at minimum cost and time.

Three models have been developed in this study that address the underlying physics associated with jet impingement heat transfer in both single phase and nucleate boiling regimes. The first model accounts for the effect of bubble generation on the overall heat transfer rate at the jet stagnation by introducing a bubble-induced diffusivity (BID). The BID is added to molecular diffusivities in the momentum and energy Equations. The BID model adopts an analogous approach to the eddy diffusivity concept used in turbulence flow modeling. The BID model has been developed to provide a cost effective simulation tool of boiling heat transfer during LJIC by considering bubble generation effect on the overall heat transfer rate while avoiding the need to simulate extremely small time and length scales associated with phase change.

The second model is a scenario identification procedure (SIP) that has been developed to predict the bubble growth termination (BGT) scenario. Considering the effect of jet velocity, water subcooling and surface superheat, the SIP identifies whether a bubble would locally collapse or slide by identifying the most probable equilibrium condition (thermal or dynamic) that the bubble would reach first. The main objective of the SIP is to avoid any inaccurate assumption of the probable BGT scenario. In this case, such procedure could improve the predictions of a more comprehensive wall heat flux model of the areas affected by various heat transfer mechanisms.

The third model is a mechanistic wall flux partitioning (WFP) model that has been developed to predict the local wall heat transfer rate over the distance between jet stagnation and ten times the jet width. The WFP model assumes that primary heat transfer is due to sensible heating of liquid by forced convection and transient conduction. The WFP model incorporates a unified single-phase heat transfer model that is capable of capturing the observed secondary peaks downstream of stagnation. The WFP model also incorporates a sub-model that predicts abrupt changes in the liquid film thickness due to the formation of hydraulic jumps.

The development of these three models have been carried out using experimental data obtained from a set of experiments that has been conducted to investigate the variation of the heat transfer rate and bubble dynamics under a planar free liquid jet. Investigation of bubble dynamics has been conducted using both intrusive optical probe and non-intrusive high speed imaging of the flow filed. The experiments have been conducted at atmospheric pressure, considering jet velocity of 0.4 to 1.7 m/s, degree of water subcooling of 10 to 28 ^{o}C, degree of wall superheat of -25 to 30 ^{o}C. Such variations have been studied along a heated surface between stagnation and ten times the jet width. Experiments were conducted using a 1 mm × 8 mm planar jet impinging on a heated horizontal flat copper surface. The distance between the jet and the heated surface was 10 mm. The experimental data have been used to develop a group of sub-models for single-phase heat transfer, bubble diameter, bubble population density, bubble release frequency, and bubble growth time. These sub-models have been used in the closure of the aforementioned models.

The three models have been validated using independent experimental data. The BID model is capable of predicting stagnation heat flux within -15% and +30%. The SIP model was able to predict the right bubble growth termination scenario of 80% of the investigated cases. The WFP model is capable of predicting the local total wall heat flux within ± 30%

DEDICATION

To the 'Princess' of My Heart; My Wife… 'Amira'.

ACKNOWLEDGEMENTS

First of all praise to God the greatest, the most merciful, the all beneficent, the omniscient, who guided the man to know which he did not know.

The work on this thesis has been inspiring, often exciting, sometimes challenging, but always interesting. This thesis has been possible by the help of many people, who made it an enjoyable experience. I wish to express my sincere gratitude to my supervisors Dr. Mohamed S. Hamed, and Dr. Mamdouh Shoukri, who guided this work and helped whenever I was in need with their encouragement, continuous support, and many fruitful discussions. I would also like to express my sincere thanks to my PhD supervisory committee members Dr. Amad Abdul-Razzak and Dr. Sumanth Shankar for their valuable suggestions and remarks through all the tasks of this study. I would also like to thank Dr. Ross L. Judd for the valuable discussions and suggestions.

I am also indebted to the technicians of Mechanical Engineering Department at McMaster University; Dave Schick, Ron Lodewyks, Jim McLaren, Mark McKenzie and Joe Verhaeghe, for their help in constructing the experimental test facility. Thanks are also due to my friends and colleagues; Dr. M.E. Shawkat, Dr. Kareem Aly, Mohammed A. El Sayed and Graham deCatanzaro for their technical assistance.

Last but not least, I cannot express my full and deepest gratitude to my wife and my parents for their never ending love and support.

NOMENCLATURE

Roman Symbol	Definition	Units
ΔT	Temperature difference	^{o}C
A	area	m^2
c_p	Specific heat	J/kg. ^{o}C
C_v	Voltage threshold constant	
c_ε	Constant in chapter 4 for the decay of bubble induced diffusivity	
D (or d)	Diameter	m
f	Frequency of bubble release	Hz
G	Water mass flux	kg/m^{2}s
g	Gravitational acceleration =9.8	m/s^2
h	Heat transfer coefficient	W/m^2.^{o}C
h_{fg}	Latent heat of vaporization	J/kg
H_n	Nozzle to heater distance	m
Ja	Jacob number= $(\rho_l c_{pl} \Delta T)/(\rho_v h_{fg})$	
k	Thermal conductivity	W/m ^{o}C
L_{slid}	Bubble sliding distance	m
N	Decay function of the additional diffusivity	
N"	Bubble population	m^{-2}
P	Pressure	N/m^2
Pr	Prandtl number (ratio between the momentum diffusivity to thermal diffusivity)	
q"	Heat flux	W/m^2
Re	Reynolds number	
S_b	Bubble spacing	m
T	Temperature	^{o}C
t_g	Growth time	s
t_w	Waiting time	s
u	Velocity component parallel to flow direction(x-direction)	m/s

v	Velocity component normal to flow direction (y-direction)	m/s
V	Voltage	Volt
V_n	Jet velocity	m/s
We	Weber number	
Greek Symbols	**Definition**	**Units**
α	Molecular thermal diffusivity	m^2/s
δ	Liquid layer thickness	m
ε	Additional diffusivity due to bubble generation	m^2/s
ε^+	Ratio of the total diffusivity, including the bubble induced diffusivity to the molecular diffusivity.	--
η	Dimensionless coordinate, y/ δ	
θ	Dimensionless temperature difference: $(T-T_\infty)/(T_{sat}-T_\infty)$	
λ	Shape factor of the single phase heat transfer coefficient	
ν	Molecular kinematic diffusivity	m^2/s
ρ	Density	kg/m^3
σ	Surface tension	N/m
φ	Angle of contact	Degree
ψ	Stream function	m^2/s
Ψ	Dimensionless stream function $(=\psi\sqrt{C/\varepsilon_{\max}})$	
Subscripts	**Definition**	
∞	Free stream condition	
avg	Average value	
b	Denoting a bubble related quantity	
c	Characteristic	
col	Collapsing without sliding	
eff	Effective value	
ev	Evaporation	
exp	Experimental	
f	Property value at average liquid film temperature	
g	Growth	

h	Denoting thermal energy
hj	Hydraulic jump
hyd	Hydraulic
i	Initial
j	Jet related value
l	Liquid
m	Momentum related quantity
max	Maximum value
max	Maximum value
min	Minimum value
mod	modified
$model$	Model predicted value
nb	Nucleate boiling quantity
o	Values at the stagnation (x=0)
ONB	Onset of nucleate boiling
s	Surface
sat	Saturation
$slid$	Sliding
sp	Single phase value
sub	Subcooled
sup	Superheat
t	Turbulent
tot	Total
v	Vapour
w	Wall for temperature or heat flux and jet width for fluid flow
ε	Related to bubble-induced diffusivity

Superscripts	**Definition**
‘	First derivative
‘ ’	Second derivative

CONTENTS

LIST OF FIGURES

LIST OF TABLES

Chapter 1

INTRODUCTION AND LITERATURE REVIEW

1.1 Background

Forced convection boiling (FCB) is one of the most efficient cooling configurations that have been used for centuries in many applications. It is characterized with the generation of vapor bubbles on a heated surface during the flow of subcooled or saturated liquid in its vicinity. The vapor generation occurs when the heated surface temperature exceeds that required for the onset of the liquid phase change. Vapor generation in FCB is cyclic in nature and so it promotes flow agitation, and liquid/surface contacts upon vapor collapse, which enhance the rate of heat transfer from the heated surface to the fluid bulk.

The degree of surface superheat represents the difference between the heated surface temperature and the liquid saturation temperature. The degree of superheat is a key factor that determines the vapor generation intensity and hence the extent of its effect (improvement) on the overall heat transfer rate. Figure 1.1 illustrates two boiling curves, starting at the boundary between the single phase forced convection heat transfer and the onset of boiling, showing the variation of heat flux with the degree of surface superheat for two different FCB configurations. These configurations are: (a) parallel flow boiling, and (b) jet impingement boiling. In both cases, at low superheat, small isolated bubbles grow intermittently at distant locations on the surface known as the active nucleation sites. This mode is known as partial nucleate boiling. As the degree of superheat is increased, nucleation at more active sites is sustained and heat transfer is improved, which is represented by a steeper boiling curve slope in what is known as fully developed nucleate boiling. The maximum heat transfer rate in the nucleate boiling regime is known as the critical heat flux (CHF). Denoted by points C1 and C2 on Figure 1.1; the CHF marks the end of the nucleate boiling regime beyond which an unstable transition boiling regime starts. In transition boiling, bubbles attain big enough sizes to merge and form large vapor patches that reside for relatively longer time and so blanket the heated surface. Blanketing causes reduction in liquid-surface contact frequency and hence deterioration in the heat transfer rate until the heat transfer rate drops to a minimum value at a surface temperature known as the Leidenfrost point; denoted by points L1 and L2 in Figure 1.1. Any further increase in surface superheat beyond the Leidenfrost point causes a stable vapor film to spread and cover the entire surface marking the onset of the film boiling regime. In film boiling, direct radiation heat transfer from the surface to the liquid bulk across the vapor blanket assists in increasing the overall heat transfer rate.

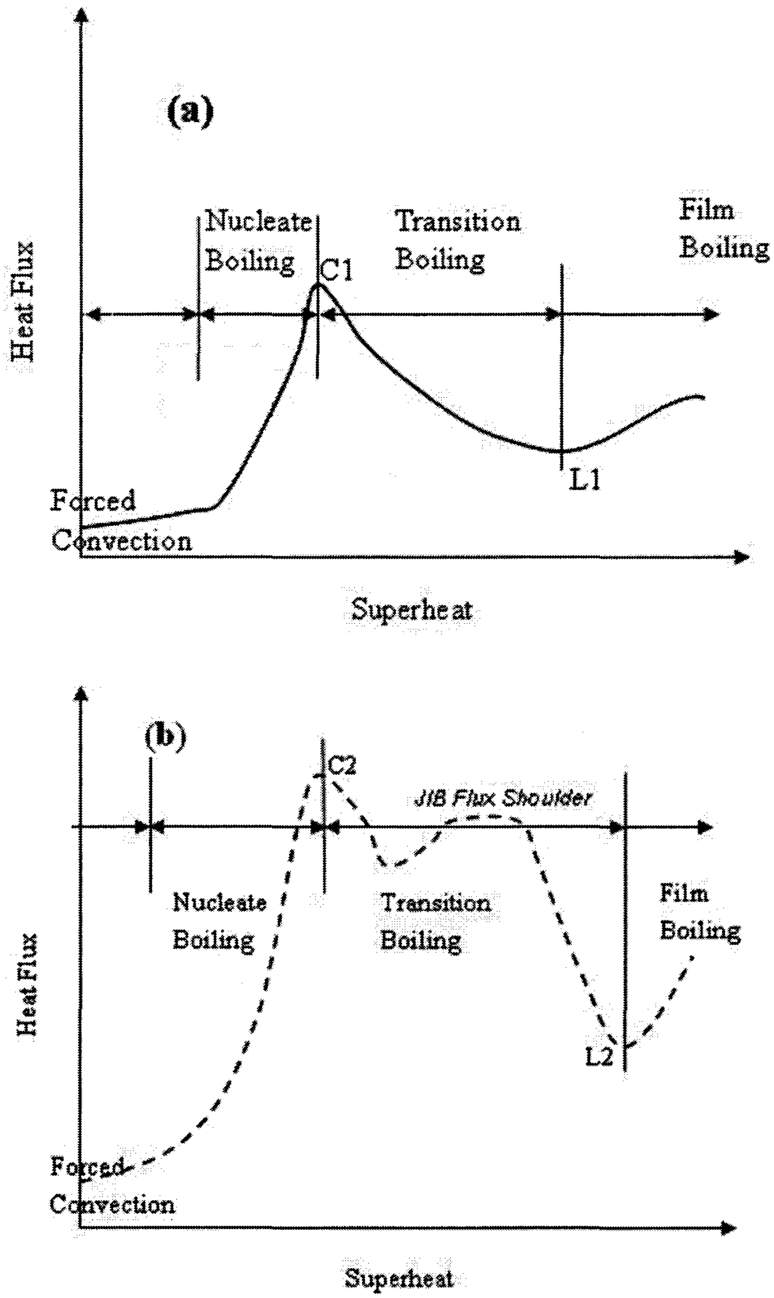

Figure 1. 1 Schematic of the boiling curves of two FCB configurations: (a) Parallel Flow Boling, PFB, and (b) Jet Impingement Boiling, JIB.

The sequence of boiling regimes shown in Figure 1.1 is typical for various FCB configurations. However, the range of surface superheat for each boiling regime and the corresponding level of attainable heat flux are different due to the difference in other parameters, such as the liquid temperature, the flow velocity, and/or flow direction. The effect of flow momentum on the overall heat transfer rate depends on the direction of flow with respect to the surface.

From this perspective, FCB can be classified into: 1) Parallel Flow Boiling (PFB) where the liquid flows parallel to the heated surface, and 2) Jet Impingement Boiling (JIB) where the liquid is admitted in the form of a jet normal to the heated surface. The use of JIB is common in cooling processes in various applications because of the desirable effect of flow momentum on the rate of heat transfer. Jet impingement provides a means to suppress the formation of large vapor patches on the heated surface that may impose an adverse condition to the heat transfer, especially in the transition regime, Ishigai et al. (1976) and Robidou et al. (2002). Robidou et al. (2002) investigated the boiling curve of JIB under steady state conditions and showed that significantly high heat transfer rate can be sustained in transition boiling over a wide range of surface superheat forming what was called a *flux shoulder* prior to dropping at the Leidenfrost point. This phenomenon of *flux shoulder* of JIB was attributed to the defragmentation of vapor patches by jet impingement, Seiler-Marie et al.(2004). Such feature renders JIB an attractive cooling configuration for applications where high heat transfer rates are required with optimal use of the cooling fluid and/or space permitted for cooling system installations, Incropera et al. (1993).

JIB is thus used in many applications such as in heat treatment of metallic sheets, continuous casting processes, cooling of electronic chips, and also had been implemented in the emergency core cooling of nuclear reactors to mitigate the consequence of Loss of Coolant Accidents (LOCAs).

Various parameters affect the design and performance of a JIB cooling system. These parameters include the jet parameters and the surface parameters. The former include: jet shape, size, velocity, liquid temperature, number of jets, and jet spacing. The later include: surface temperature, material, curvature, speed, etc. The development of a predictive tool of the heat transfer rate of JIB enables the design of effective cooling systems. These tools can also be used to analyze operational modifications of existing systems due to changes in application requirements.

FCB is governed by a number of coupled mechanisms that contribute in different extents to the overall heat transfer rate of FCB. Understanding the underlying physics and nature of such contributing mechanisms is essential in developing predictive models that incorporate these mechanisms and the effect of their interactions. This can be achieved by conducting experimental investigations that capture boiling details under variable flow conditions for the configuration of interest, i.e., PFB or JIB.

Two modeling approaches have been used to develop predicting tools of the heat transfer rate of FCB: 1) Global modeling, and 2) Subscale or mechanistic modeling. The choice of the modeling approach depends on the level of details to be accounted for in the model and the availability of relevant experimental data to support model development and validation.

In the global approach, two levels of modeling have been identified in the available literature. The first level has been adopted in large number of previous studies of JIB, Incropera et al. (1993). At this level, the overall heat transfer rate is presented in the form of empirical correlations as a function of jet velocity, subcooling and surface superheat. No explicit representation of the effect of bubble dynamics was made. Rather, the empirical constants are adjusted to realize agreement between model prediction and a set of experimentally obtained heat transfer data. Although this approach is simple, its applicability is limited to the experimental conditions used to develop the empirical correlations. Therefore, it cannot cope with design or operational changes.

The second level of global modeling incorporates the effect of boiling (bubble dynamics) in single-phase heat transfer correlations by introducing some empirical or mechanistic relations. Unlike the first level of global modeling, only few studies were conducted implementing this approach. Timm et al. (2003) incorporated a bubble-induced *additional diffusivity* into the diffusion terms of the conservation Equations.

They solved these Equations for the case of a planar water jet impinging on a horizontal steel plate initially heated to 900 °C. In this study only a qualitative description of the variation of the additional diffusivity with surface superheat was provided. Mikielewicz et al. (2007) incorporated a *blowing parameter* into the convective terms of the conservation Equations to account for bubble protrusion effect on the flow field of a single round jet impinging on a disc subjected to constant input heat flux. However, they did not provide experimental validation of this approach.

Such hybrid empirical/analytical global modeling approach could be used to model JIB without overlooking the underlying physics, especially the effect of bubble interactions with the mean flow. The approach is flexible to accommodate changes in application requirements. However, lack of information about the variations of bubble dynamics with JIB flow parameters has limited the development of this type of models.

In subscale modeling, mechanistic representations are developed for the various heat transfer mechanisms (partitions) between the heated surface and the fluid bulk. Each heat transfer mechanism (partition) takes place at a certain portion of the heated surface for a certain period of time. The overall heat transfer rate is then determined by time averaging of these individual heat transfer mechanics. The parameters that characterize each heat transfer mechanism are either: (1) independent or controlled parameters, such as flow velocity and temperature, which do not need to be modeled; or (2) dependent parameters, such as the heat transfer coefficient and bubble dynamics parameters, which are defined by other independent and/or dependent parameters, and hence need to be modeled prior to obtaining the various heat transfer partitions.

The main advantage of subscale modeling is that it provides comprehensive insight and implementation of the underlying physics into the model by accounting for each possible mechanism separately and by representing it in a mechanistic form. Subscale modeling allows one to examine the sensitivity of each heat transfer mechanism to certain changes of the cooling process configuration. Mechanistic models have an important feature in that they require less validation as compared to that required for empirical models, Basu (2003) and Warrier et al. (2005). This is preferred in situations where experimentation is costly, or difficult to conduct repetitively as in the case of the nuclear industry.

The majority of the available studies on mechanistic modeling of boiling heat transfer focused on pool boiling, Judd and Hwang (1976), and on PFB configuration, Basu (2003). There is a lack of similar studies for JIB. Since the basis of JIB is similar to PFB, one could be guided by the findings of the studies carried out on PFB. However, the difference in the flow field between JIB and PFB must be addressed and taken into account.

Various assumptions have been made regarding the representation of the responsible heat transfer mechanisms in modeling of pool boiling and PFB, Bowering (1962), Judd and Hwang (1976), and Basu (2003). Early investigations attributed all the heat transfer from the surface due to evaporation only, Griffith (1958). Recent studies attributed the heat transfer to sensible heating of liquid while evaporation has been neglected or considered as a secondary heat transfer mechanism, Del Valle and Kenning (1985), Basu (2003), Seiler-Marie (2004). These assumptions could be used as guidelines for JIB modeling where there is a scarcity of representative mechanistic modeling work. Detailed experiments of JIB are necessary to support the adopted model and identify primary heat transfer mechanism(s).

Various assumptions of the expected bubble motion into the fluid bulk upon reaching the bubble maximum diameter have been made in the case of PFB heat transfer. Bubble motion is important as it defines the area of the heated surface that would be affected by the different heat transfer mechanisms. Two main approaches have been postulated to model the bubble growth termination process and the consequent behavior of the bubble in the fluid bulk: The first approach adopted the assumption of Thermally-controlled growth Unal (1976). The second approach assumed that growth termination is inertia-controlled, Klausner et al. (1993). More details of both approaches will be presented in the next section. The thermally-controlled approach assumes that the bubble would collapse in place and the area affected by the bubble is in the order of the bubble projected area. The inertia-controlled approach assumes that the bubble would slide along the surface and in this case the affected area would be different from that in the thermally-controlled termination case. The existing models overlook the fact that both scenarios could take place at different locations of the flow field or under various flow conditions, as reported by Basu (2003). This shortcoming would affect the predictability of the existing heat transfer mechanistic models. So, there is a need to develop a systematic scenario identification procedure (SIP) of the most probable scenario of the bubble growth termination process in order to remedy such shortcoming.

In modeling of free JIB, where there is an interface between the jet liquid stream and ambient air, there is a possibility of formation of a *hydraulic jump* in the liquid film downstream the jet stagnation point. This phenomenon takes place to build up a hydrostatic pressure for the liquid flow to overcome wall friction or any obstacle to the flow along its path, Okishi (1996). A hydraulic jump is characterized by a rapid increase in liquid film thickness and a decrease in flow velocity downstream of the jump. Although hydraulic jumps have been extensively discussed in fluid mechanics textbooks for single phase parallel flow in open channels, they have not been addressed in the context of free JIB modeling. It is postulated here that accounting for the effect of the hydraulic jump in JIB modeling would improve the predictability of the SIP, which in turn would improve the predictability of the mechanistic models of the JIB heat transfer.

In conclusion, incorporation of the physical aspects of JIB heat transfer in global or in subscale mechanistic models would provide flexible, efficient predictive tools of heat transfer for various applications. However, the development of such models requires comprehensive experimental investigations to provide detailed information about the interaction between jet flow and generated bubbles on the heated surface. Some guidelines exist in previous PFB modeling studies relevant to the modeling assumptions of the primary heat transfer mechanisms. However, modeling of JIB involves some unique features of free surface JIB flow field that do not exist in PFB heat transfer.

1.2 Literature Review

1.2.1 Introduction

In this section, a literature review is presented of previous work relevant to FCB modeling. The focus of this review is on the previous studies that provided global or subscale models to predict heat transfer under any of the two FCB configurations, i.e., under JIB or PFB. As the existing models were developed using experimental data, this review is focused on the details of the various experimental techniques of the heating method used to induce boiling and on the techniques used to investigate bubble dynamics.

The objectives of the current research have been identified and presented at the end of this chapter. These objectives have been identified based on the existing gaps pertaining to JIB modeling.

1.2.2 Review of Jet Impingement Boiling (JIB) Modeling

As mentioned before in section 1.1, two approaches have been adopted in FCB modeling, a global approach and a subscale (*mechanistic*) approach. The amount of work using each approach varied for PFB and JIB. As the focus of the current research is on JIB, only previous studies of PFB with modeling and or experiments relevant to JIB have been reported here.

1.2.1.1 Global modeling of JIB

The main objective of all JIB studies is the determination of the heat transfer rate from a heated surface to the liquid. Empirical correlations have been developed to describe the various modes of JIB heat transfer: single phase (Furuya et al. (1995), and Lienhard (1998)), onset of nucleate boiling (ONB) and the corresponding superheat as function of jet velocity and degree of subcooling (Vader et al. (1992), Viskanta et al. (1993), and Zhou and Ma (2004)), and fully developed boiling heat (Ma and Bergles (1986), Furuya et al. (1995), and Bartoli et al. (1997)). Special attention has been given to the development of critical heat flux (CHF) correlations under JIB conditions (Katto and Shimuzu (1979), Katto and Yokoya (1988), Furuya et al. (1995), and Liu et al. (2004)). Most of these studies were conducted using impinging water jets. Fewer studies developed empirical correlations for other fluids such as R-113, Ma and Bergles (1986) and Zhou and Ma (2004).

In the single-phase regime, the jet impingement heat transfer coefficient has been correlated to Reynolds number, Re, and Prandtl number, Pr, using a power form similar to the case of laminar boundary layer flows, i.e.,

$$h \sim (Re^{a}.Pr^{b}) \tag{1.1}$$

Deviations from Re and Pr exponents in the case of laminar flow over flat plate, i.e., from a = 0.5 and b = 0.33, was attributed to the effect of jet stream turbulence. Reynolds number was defined using the jet velocity and either the heater characteristic dimension; i.e., diameter or length, as in Shafer et al. (1991) or the jet hydraulic diameter, as in Duckle and Hollingsworth (1996).

In the fully-developed nucleate boiling regime the heat flux was correlated to the wall superheat in a power form, i.e.,

$$q''_{fullydeveloped} \sim \Delta T_{\sup}^{c} \tag{1.2}$$

Postulations have been made that the heat flux is independent of flow conditions as bubble-induced heat transfer mechanisms dominated the forced convection mechanism, Ma and Bergles (1986). Wide range exists for the values of the exponent c used in correlating the fully developed wall heat flux to the surface superheat. Bartoli et al. (1997) reported a wide range of *c* between 1.8 and 4.2 which is an indication that the assumed form in Equation (1.2) lacks generality.

In the partial boiling regime, the corresponding surface temperature associated with the onset of boiling (ΔT_{ONB}) has been determined from the analysis of slope changes of the boiling curve. The boiling curves are obtained from the measurements of interior temperatures just below the exposed heated surface. The exposed surface temperature and the associated wall heat flux are then obtained by extrapolating the interior temperature measurements and the gradient of their distribution normal to the flow direction, respectively. The surface superheat at the onset of nucleate boiling (ONB) was determined from the first change of boiling curve slope. Vader et al. (1992) and Incropera et al. (1993) have determined the heat flux by recording the current and volt across the heated surface while the corresponding surface temperature was still obtained from extrapolation of interior temperature readings to plot the boiling curve for given jet impingement conditions. They have also compared the values of ΔT_{ONB} obtained from the slope changes with those corresponding to first appearance of bubbles as detected by visual observations of the flow field. The ONB heat flux has been obtained by interpolation of heat flux values of single- phase regime and fully developed nucleate boiling regimes, Ma and Bergles (1986), Carry (1992) and Zhou and Ma (2004).

Generally, although empirical correlations are simple in form and require direct substitution to obtain average or local values of the heat flux, their applicability is limited to certain flow parameters.

A further insight of the governing physics has been introduced into global modeling of JIB via the incorporation of empirical correlations of bubble dynamics into the conservation Equations of single-phase impingement jet flows, Timm et al. (2003) and Mikielewicz et al. (2007). The work of Timm et al. (2003) on analytical/empirical global modeling of JIB was based on the analytical model developed by Zumbrunnen (1991) of single-phase heat transfer to a planar water jet on stationary and moving plates, which was developed to determine heat transfer during heat treatment of steel sheets on run-out tables. Timm et al. incorporated the effect of boiling into the momentum and energy Equations by introducing an additional diffusivity to the molecular diffusivity in the diffusion terms. This is similar to the concept of using eddy diffusivity in turbulence modeling, White (1991). The advantage of this approach is that addressing the bubble-induced effect in a single term adds only minimal complication to the solution procedure of the conservation Equations, while accounting for the complicated interactions within the flow domain due to boiling. This approach has thus the potential to obtain the heat transfer rate of JIB at less computational cost than that of using more complicated two-phase models.

Timm et al. (2003), used experimental heat flux values to determine the corresponding additional diffusivity values by assuming constant bubble diameter in the order of 10^{-4} m, and bubble life time in the order of 10^{-4} s. Variation of the additional diffusivity with surface superheat has been presented only for the case of a 10 mm thick planar free water jet (with no mentioning of the jet depth) impinging on a steel sheet initially heated to 900 °C. Water velocity was varied from 3 to 11 m/s while water subcooling was kept constant at 75 °C.

Detailed modeling of the bubble-induced diffusivity has not been reported in Timm et al. (2003) although it was suggested in that study that the bubble induced diffusivity should be modeled in terms of time and length scales related to bubble generation, i.e.: bubble life time and diameter. The length scale to be used in such models should represent the dependence of the bubble-induced diffusion on nucleation intensity and its extent within the flow domain where it has a significant role.

It is concurred here that while using a constant length scale might be appropriate for determining single-phase heat transfer, using a bubble dynamics dependent length scale would be more appropriate for modeling bubble-induced heat transfer in JIB. A possible length scale could be the bubble diameter. The dependence of such length scale on the bubble dynamics requires a detailed experimental investigation to be carried out of the bubble dynamics under specific JIB conditions, which is one of the main objectives of this study.

1.2.1.2 Subscale mechanistic modeling of JIB heat transfer

The subscale, mechanistic, modeling approach provides an alternative means of quantifying wall heat flux based on the governing physical mechanisms. This approach facilitates model development and modifications based on physical reasoning, rather than adjusting a set of coefficients or exponents as in the case of empirical models. In FCB, various heat transfer mechanisms take place at different parts of the heated surface, either simultaneously or sequentially. The mechanistic modeling approach of these mechanisms has been referred to in the literature as wall *flux partitioning*. Time averaging of heat transfer rates, *partitions*, due to the various mechanisms provides the overall wall heat flux under any given cooling conditions, Basu (2003). Various scenarios were considered in partitioning the wall heat flux in boiling heat transfer.

In pool boiling, Griffith (1958) attributed all of the wall heat transport to liquid evaporation once nucleation begins; whereas Judd and Hwang (1976) suggested three different partitions: 1) single-phase free convection, 2) transient conduction to liquid that replaces departing bubbles from the surface, and 3) direct evaporation of a liquid layer entrapped beneath the growing bubbles.

Similar variations exist in heat flux partitioning in the case of PFB. Bowring (1962) investigated heat transfer in subcooled PFB in horizontal pipes and adopted a three-partition hypothesis considering that the overall heat transfer rate is due to the interplay of three mechanisms: single-phase heat transfer, evaporation heat transfer, and pumping heat transfer. Pumping heat transfer is due to the sensible heating of liquid replacing departing bubbles. The relationship between evaporation and pumping heat transfer partitions was determined from experimental results at various pressures for internal flow sub-cooled boiling. Del Valle and Kenning (1985) attributed the overall heat transfer rate in subcooled fully developed PFB (70-95% of CHF) in stainless steel tubes to the interplay of two main mechanisms: transient heat conduction and forced convection. Evaporation heat transfer was also considered as a primary heat transfer mechanism; however, it was found to have a small contribution to the overall heat transfer rate. Other PFB studies assumed two heat transfer partitions, (Akiyama (1973), Lahey (1978), and Basu et al. (2003), where evaporation heat transfer was not considered as a primary mechanism in direct heat transfer from the surface.

Basu (2003) developed a mechanistic model of the wall heat flux to subcooled water flowing upward in a vertical conduit under steady state heating of one side of the conduit assuming variable contribution levels of different heat transfer mechanisms depending on bubble generation intensity. If no bubbles were generated on the surface, all the heat transfer was attributed to single-phase forced convection. In the early stage of boiling, with low bubble generation intensity, an enhancement factor of 1.3 was introduced to the single-phase heat transfer coefficient to account for the effect of bubble protrusion. With the escalation of bubble generation intensity, two heat transfer mechanisms were considered at different locations of the heated surface: 1) single phase forced convection on areas of the surface where no bubbles exist, and 2) sensible heating of liquid by transient conduction heat transfer, where bubbles appear/disappear repetitively. The net effect due to heat transfer from the heated surface is direct sensible heating of liquid bulk and increase of vapor content due to bubbles growth subsequent to liquid superheating in the vicinity of the heated surface.

The duration of each heat transfer mechanism was determined from the bubble growth time, t_g, and the bubble wait time, t_w, time. The bubble growth time is defined as the duration of bubble growth until the bubble reaches its maximum diameter. The bubble wait time is the duration between bubble collapse or departure from its nucleation site and the onset of the next bubble at the same site.

Basu (2003) has validated the aforementioned model using experimental data obtained for upward water flow in a square vertical, heated channel. The information about the bubble growth was obtained using high speed imaging at 1225 frame/s whereas the flow conditions were varied as follows: the water mass flux was varied between 124 to 926 $kg/m^2.s$, the wall flux was varied between 2.5 and 113 W/cm^2 and the system pressure was varied between 1.03 to 3.2 bars.

Visual observations were used to investigate various growth termination scenarios, i.e., bubble collapse and sliding. Based on these observations, modeling of the area fractions of each heat transfer mechanism and constitutive model closure relations were carried out.

It is worth noting that no such comprehensive study of various heat transfer mechanisms in JIB has been carried out. However, the modeling approach proposed by Basu can be adopted for JIB configuration provided that an appropriate modeling of the heat transfer mechanisms and suitable constitutive relations for model closure are developed and/or selected for JIB configuration.

1.2.1.3 Modeling of bubble dynamics in FCB

To the author's best knowledge, no previous studies have been carried out specifically for investigating and modeling of JIB bubble dynamics. However, the effect of surface superheat and liquid subcooling on bubble dynamics in terms of maximum bubble diameter and number of active sites have been intensively studied and empirically correlated in the context of pool boiling, Sernas et. Al. (1969), Cooper (1970), Mikic et. al. (1970) and Judd et. al. (2004). In the context of forced convection boiling (FCB), similar studies have been carried out for internal PFB in horizontal and vertical conduits, Zeitoun (1994), and Basu (2003).

Two mechanistic approaches have been used in previous studies. These approaches are used to determine the maximum bubble diameter and bubble motion in the flow bulk upon reaching that diameter. Only studies of bubble dynamics in PFB are mentioned below.

The first approach adopted by Unal (1976) postulated that thermal equilibrium, i.e., the balance between various heat flows to and from a growing bubble on the heated surface, determines the bubble maximum attainable diameter, As shown in Figure 1.2, a growing bubble absorbs heat, $q_{b,in}$, from a superheated liquid layer of thickness δ_{sup} at temperature T_{sup} next to the heated surface. In case of subcooled flow boiling, the protrusion of the bubble into the subcooled liquid at temperature T_f would initiate vapor condensation heat loss, $q_{b,cond.}$ In this case bubble growth would be slowed and eventually reversed, denoting bubble collapse. According to the review of available literature on bubble growth in flow boiling conditions, consideration of bubble departure using this approach has not been addressed, which is one of the objectives in the current study.

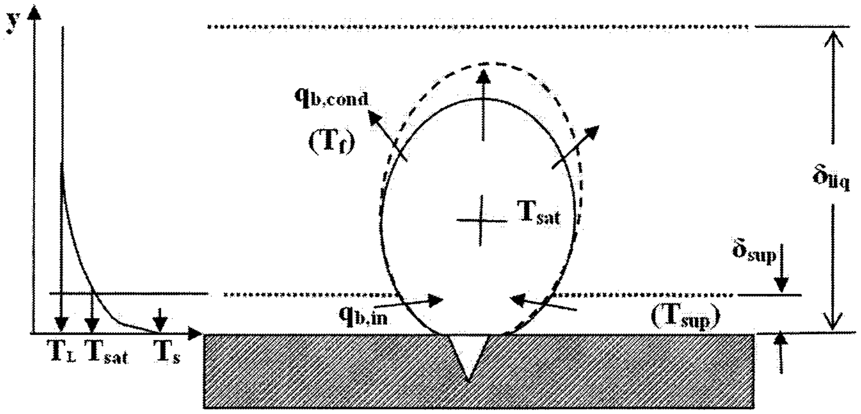

Figure 1. 2 Thermal field around a growing bubble.

The second approach postulated that dynamic equilibrium, i.e., the balance of forces acting on a growing bubble, is responsible for bubble growth termination. Identification of significant forces on a growing bubble has been provided by Koumoutsos et al. (1968), Vendervort et al. (1992), Klausner et al. (1993), and Steiner et al. (2005). Figure 1.3 summarizes significant forces acting on a bubble growing on a horizontal surface during PFB as identified by Klausner et al. (1993) and Steiner et al. (2005). A drag force (F_{qs}) that acts to remove the bubble from its nucleation site is opposed by the horizontal component of the liquid inertia force, $F_{du,x}$. The vertical component of the liquid inertia force due to bubble growth, $F_{du,y}$, acting to maintain the bubble on the surface is opposed by both the buoyancy force, F_b, and the lift force, F_{sl}. Assuming a spherical bubble, surface tension was neglected at departure due to the small contact area between the bubble and the heated surface.

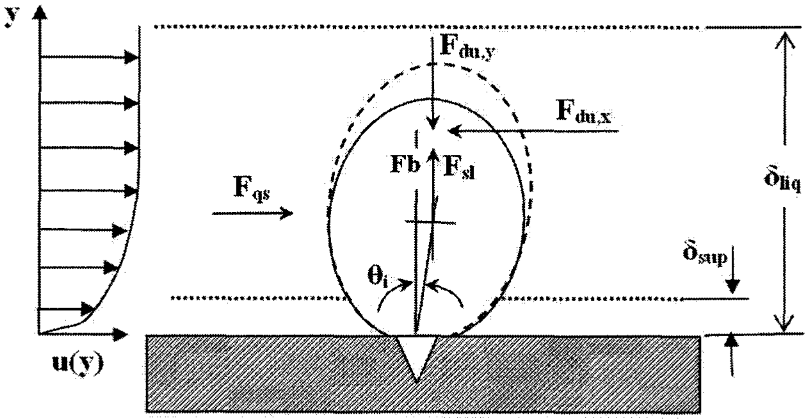

Figure 1. 3 Acting forces on a growing bubble.

Discrepancy exists between the aforementioned approaches regarding the extent of bubble growth into the fluid bulk and the assumption put forth about the growth termination event. While Unal (1976) imposed no restrictions on the bubble growth into the sub-cooled layers of the bulk flow and assumed that all bubbles collapse at the nucleation site, Steiner et al. (2005) imposed a limit on the maximum bubble diameter being equal to the thickness of the superheated liquid layer in the vicinity of the heated surface. They assumed that, upon reaching a certain diameter that is limited to the thickness of the superheated liquid layer, the bubble would depart and slide along the heater surface.

It is postulated here that a better modeling approach that does not impose any prior assumptions of the expected growth termination condition (scenario) is still lacking. Rather, all possible scenarios should be accounted for in the analysis and the most probable one would be determined by the model based on flow velocity, subcooling and surface superheat.

1.2.2 Experimental Techniques of Investigating JIB

The development of pertinent models for the JIB configuration necessitates conducting experimental investigations to collect necessary information of bubble dynamics under JIB configuration. Experiments that have carried out on JIB can be classified as transient and steady-state experiments.

Transient JIB experiments have been conducted extensively, e.g., Ishigai et al. (1976), Chen et al. (1992), Hammad et al. (2004), and Akmal et al. (2008). These experiments are carried out by initially heating the surface to a sufficiently high temperature based on the boiling regime(s) of interest (~ 300-1000 °C), and then quenching the surface with a liquid jet impinging at the desired velocity and degree of subcooling. A typical temporal change in surface temperature during a transient experiment is shown in Figure 1.4. Beside bubble dynamics, transient experiments have also been conducted to investigate propagation of the wetting front using high-speed imaging as shown in Figure 1.5. The wetting front is the edge of the region on the surface at which direct contact between the liquid and the surface is established and at which efficient nucleate boiling heat transfer exist, Akmal et al. (2008). By determining the rate of propagation of the wetting front, transient experiments can provide information on surface cooling uniformity and its impact on material microstructure and mechanical properties. Unless the surface has a high thermal capacity to slow down transient temperature variations, the various boiling regimes cannot be sustained for long enough time to capture the details of bubble dynamics on the heated surface, Monde (2002). This is why bubble dynamics investigations are usually carried out through steady-state experiments.

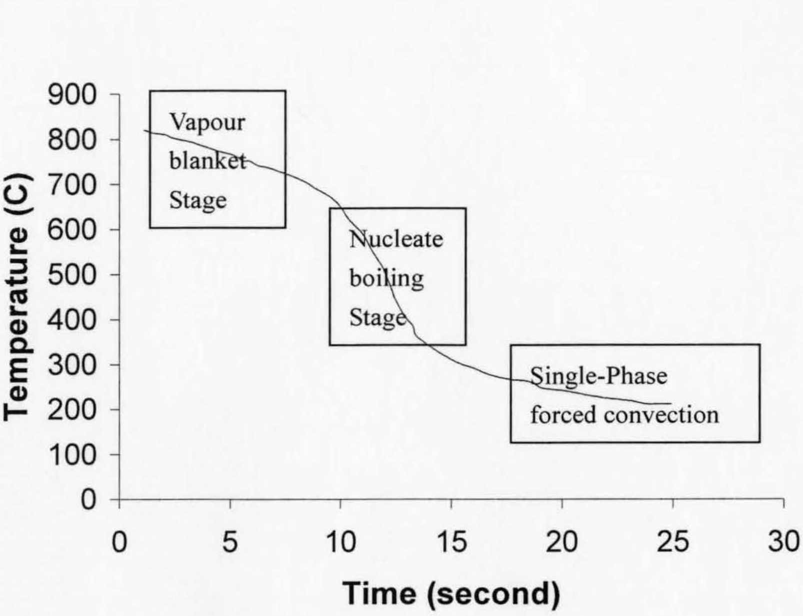

Figure 1. 4 Temperature transient and heat transfer stages in transient cooling.

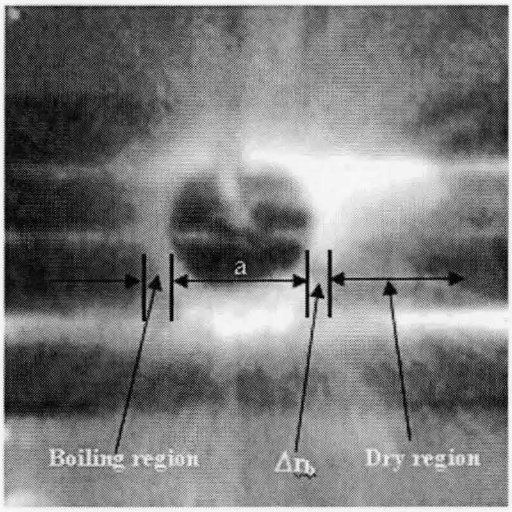

Figure 1. 5 Various heat transfer regimes during free surface jet impingement quenching of steel cylinders, Akmal et al. (2008)

In steady-state experiments specific boiling conditions can be sustained for sufficiently long time to capture all necessary details. In this type of experiments, heat input to the heated surface is controlled to establish a certain level of surface heat flux or surface temperature.

Once the required controlled surface superheat is established, the corresponding boiling intensity is sustained until the heat input is changed to a different level, Vader et al. (1992) and Robidou et al. (2002). This type of experiments can be used to replicate processes of continuous cooling of electronic chips and emergency core cooling in nuclear reactor accidents, Incropera et al. (1993) and Basu (2003).

A main concern in conducting steady-state experiments is that, due to the high cooling efficiency of jet impingement, the heat source must have sufficient capacity to compensate for the high heat removal rate. In previous experimental studies of JIB, jet velocity was kept relatively low to allow for boiling onset slightly above the liquid saturation temperature. The typical range of jet impingement velocity in steady-state experiments is in the order of 1 m/s, e.g., 1 m/s in Vader et al. (1992), 1 to 2.1 m/s in Wolf et al. (1995) and 0.4 to 0.97 m/s in Robidou et al. (2002).Another concern is the choice of whether the experiments are conducted under constant surface temperature or constant heat flux. Using a constant surface temperature is preferred over using a constant heat flux because the former facilitates the investigation of unstable transient boiling. In this regime the heat flux is in inverse proportion to the surface superheat, Robidou et al. (2002). However, the challenge in doing so is that surface temperature control increases the complexity of the power source controller and dictates the implementation of feedback into the control procedure to avoid burnout beyond the CHF.

In many of the previous experimental studies of JIB, e.g., (Vader et al. (1992) and Kamata (1999), the information on bubble generation intensity was obtained using high speed video imaging both in the partial and in the fully-developed nucleate. However, no quantification of bubble dynamics has been reported. Only qualitative descriptions of the variation of bubble size and population intensity have been reported. The degradation of image clarity due to intense vapor generation limits the use of video imaging to capture precise information of bubble dynamics under free JIB, Akmal et al. (2008). Image clarity is also impacted by the wrinkles and light reflection on the free surface in the vicinity of jet stagnation. So, reliable details of bubble generation is difficult to obtain under JIB conditions unless appropriate measures are taken to continuously remove generated vapor and to illuminate the flow field such that interference due to light reflections on the free surface is minimized. As no free surface exists in a PFB flow field, such issues represent no challenge to visual observations of bubble dynamics. Hence, high-speed imaging was sufficient to obtain necessary information to quantify bubble dynamics in the case of PFB, Klausner et al. (1993), Basu (2003), and Steiner et al. (2005).

An advanced measurement technique of bubble dynamics has been proposed by Bogdanic et al. (2007) by using a miniaturized intrusive optical probe to study bubble dynamics in steady-state subcooled JIB on a flat surface. The intrusive probe was used to measure the bubble generation frequency at the stagnation point of a 1 mm x 9 mm planar free water jet. The investigation was carried out for one set of jet conditions whereby the jet velocity and Subcooling were kept constant at 0.4 m/s and 20 °C, respectively. The variation of bubble release frequency over the entire boiling regime was investigated and reported. However, the relation between the cooling conditions and the bubble release frequency has not been implemented in the model. The intrusive probe was capable of measuring bubble release frequency but it would not provide information about maximum bubble diameter or bubble population intensity.

1.2.3 Conclusions

Based on the above literature review of modeling and experimental investigations of various FCB configurations, the following conclusions have been arrived at:

1- Both global and mechanistic subscale approaches have the potential to incorporate complicated JIB heat transfer governing physics and provide predicting tools that are not only flexible to changes of application requirements, but also simple in structure and computationally inexpensive.

2- Unlike PFB modeling, detailed experimental investigations of the interrelation between bubble dynamics, jet velocity, liquid subcooling, and surface superheat are lacking in the available literature.

3- Due to the repetitive, rapid, bubble growth and decay in JIB, the use of high speed measurements techniques is necessary.

4 -Due to the limitations of intrusive and non-intrusive measurement techniques, a combination of both would be important in studying bubble dynamics under JIB.

5- Many of the existing studies of PFB have overlooked the possibility of having different growth termination scenarios at various locations in the same flow field or under different flow conditions. In the case of JIB and due to flow filed variations downstream the jet stagnation and with the existence of a free surface between the liquid film and the surrounding air, it is necessary to develop an identification procedure of bubble growth termination scenario at various locations of the flow field and under various flow velocity and subcooling. Such scenario identification procedure (SIP) is essential for the proper partitioning of the heated surface area that is a basis of the mechanistic wall flux partitioning models. Specific flow field features of JIB such as the possibility of the formation of hydraulic jumps should be addressed in the SIP and in the mechanistic wall flux partitioning model.

1.2.4 Research Objectives and Plan

Based on the above review of the previous research work of JIB modeling, it has been found that although inclusion of underlying physics of JIB could improve heat transfer models predictions; little attention has been given to various modeling approaches that encompass these physics as compared to the enormous empirical modeling work found in the available literature. This is attributed to the stochastic nature of bubble generation on heated surfaces and the complexity associated with the interactions between the bubble growth and flow hydrodynamics. It is hence objected in the current study to develop models of JIB heat transfer rate that consider these variations and interactions based on better understanding of the physical aspects that governs the heat transfer process. This can also provide flexibility in accommodating postulated changes to the application configuration and/or process requirements.

Specific to free JIB configurations, there is scarcity of the available information on the variation of bubble dynamics parameters under free JIB configuration which could support development of mechanistic heat transfer models. In addition, with the advances in the computational capacity, sub models representing various bubble dynamics parameters can be included in computational fluid dynamics codes to simulate phase change heat transfer in JIB configurations. This will allow identification of potential opportunities for enhancements of cooling processes and system configurations based on more realistic predictions, Narumanchi et al. (2008). It is one of the objectives of the current study to develop suitable relations that describes the parameters of bubble dynamics which could be incorporated into the mechanistic models or simulation tools of JIB process.

Due to lack of such information in the context of JIB modeling, to achieve the above objectives, an enabling objective of the current study is to experimentally obtain the necessary information on the variations of bubble dynamics parameters such as the bubble diameter and release frequency with various JIB cooling parameters such as the jet velocity and liquid subcooling using a comprehensive set of measurements tools. Each tool should provide an original piece of information that will help making a full picture of the bubble dynamics variations under JIB conditions and so supporting the development and validation of the heat transfer models.

In order to achieve these objectives, the following research plan has been constructed:

1- In the initial stage of this research, it has been objected to experimentally investigate the specific characteristics of single-phase and nucleate boiling heat transfer regimes under free planar jet impingement that resemble various industrial applications. The experimental study has adopted steady-state, controlled-temperature heating of a flat surface. Temperature measurements have been conducted at various locations from the jet stagnation to obtain the spatial distribution of the surface temperature and heat flux. The ranges of experimental parameters have been selected comparable to those of previous studies of JIB and to ensure that boiling will occur with various intensities, i.e., low intensity that characterizes partial nucleate boiling and high sustained intensity of fully developed nucleate boiling. The velocity range in the current research has been from 0.4 to 1.7 m/s, the water subcooling range has been from 10 °C to 28 °C, while surface temperature has been varied from 75 °C to 125 °C.

2- To complement the experimental investigation in attempt to establish the modeling basis, it has been objected to develop an in-depth understanding of the governing physics of JIB heat transfer by experimentally studying the interrelations between bubble dynamics and jet flow parameters using both intrusive and non-intrusive measurement techniques. Use of an intrusive optical probe aimed to investigate the variations of bubble generation frequency and growth time, while use of non-intrusive high speed video imaging aimed to study the bubble maximum diameter, and bubble population, as well as bubble growth termination scenarios under various jet impingement conditions.

3- It has been objected to incorporate the obtained information from the experimental investigations to develop a hybrid empirical/analytical global model that accounts for the bubble dynamics in the determination of heat transfer rate in nucleate JIB. The global model has implemented the concept of additional diffusivity in determining the heat transfer rate. This model has the potential of being incorporated in numerical simulation of JIB heat transfer with minimal addition to the computational cost.

4- The experimental findings have been also used to develop a subscale mechanistic wall flux partitioning model of nucleate JIB. It has been aimed to address specific features of free JIB in the mechanistic model such as the rapid increase in the liquid film thickness known as the hydraulic jump. Model closure has been achieved using constitutive submodels of bubble dynamics as well as submodels of the flow hydrodynamics characteristics that have been specifically developed for JIB.

5- A mechanistic approach has been developed to determine the bubble growth termination scenario via the development of a Scenario Identification Procedure (SIP) based on the principle of precedence and supported by visual observations of bubble motion upon reaching the maximum diameter. This SIP has also taken into account the formation of hydraulic jump downstream jet stagnation in the determination of bubble growth termination scenario.

1.2.5 Thesis Structure

The thesis consists of seven chapters. Chapter 1 provides an introduction to FCB, its configurations and main applications, as well as a review of previous studies on modeling and experimentation of jet impingement boiling. Chapter 1 also lists the main and the enabling objectives of the current research. Chapter 2 provides a description of the experimental test facility, designed and constructed to conduct the experimental work necessary to achieve the objectives of the current research. Details are presented about the measurement techniques of various parameters and the methods of data acquisition and analysis. Chapter 3 provides the main findings of the experimental investigation of JIB heat transfer and bubble dynamics. It also describes the development process of the constitutive sub-models of heat transfer and bubble dynamics parameters used in the closure of the JIB model. Chapter 4 describes the development of the hybrid empirical/analytical global model of JIB using the concept of the additional bubble-induced diffusivity. Chapter 5 describes the development of the scenario identification procedure (SIP) of bubble growth termination under various flow conditions. Discussion has also been provided in this chapter on empirically derived criteria to determine the most probable scenario as drawn from visual observations. Chapter 6 describes the development of the mechanistic wall flux partitioning model of JIB including the bubble dynamics sub-models and the bubble growth termination criteria. Finally, chapter 7 summarizes main findings of the current research and contributions made to the existing knowledge in the context of JIB modeling as well as recommendations for future work.

Chapter 2

EXPERIMENTAL TEST FACILITY AND DATA ANALYSIS TECHNIQUES

2.1 Description of Experimental Test Facility

2.1.1 The Flow Loop

A flow loop has been constructed at the Thermal Processing Laboratory (TPL), McMaster University to conduct experimental investigations of liquid jet impingement boiling (JIB). This flow loop has been used in the current research to investigate steady-state nucleate boiling under a free planar water jet impinging on a flat surface. A schematic of the flow loop is shown in Figure 2.1.

As shown in Figure 2.1, the flow loop consists of two tanks: a water supply tank (1) and a collecting tank (13) where the boiling module (12) is placed. Water is heated to the desired temperature in the supply tank using a 5 kW immersion heater (2a). Water is delivered at the desired flow rate to a 1 x 9 mm slot nozzle (1) using a centrifugal pump (4). It returns back to the supply water tank (1) due to gravity. A low-flow turbine meter (6) (Omega FTB-9504, maximum flow rate of 0.26 GPM) has been used to measure the flow rate to the nozzle (11).

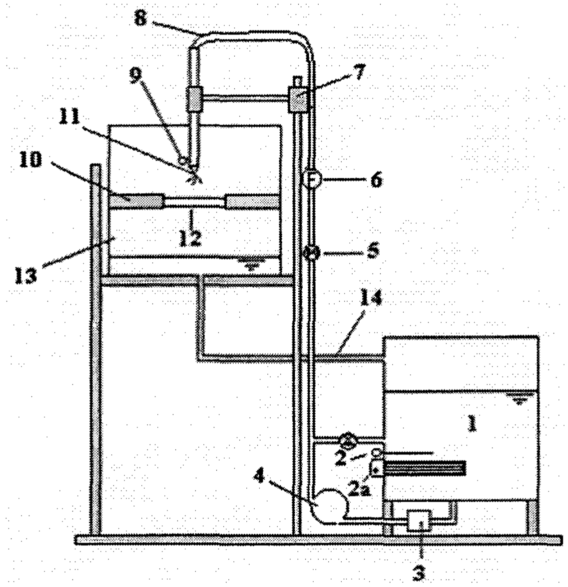

Figure 2. 1 Schematic of flow loop: 1-Water tank, 2-thermocouple, 2a- Water heater, 3-strainer, 4-pump, 5-valve, 6-flow meter, 7-nozzle holder, 8- hose, 9- thermocouple, 10-test section holder, 11- planar nozzle, 12- boiling module, 13-Collecting tank, 14-Drain

The set point temperature of the immersion water heater placed in the supply tank was adjusted at a slightly higher value than that required for the experiment in order to account for heat losses in the piping. Two thermocouples were used for this purpose: a T-type thermocouple (2) in the supply tank and a K-type thermocouple (9) at the nozzle inlet to monitor the actual jet temperature, which is used to calculate the actual degree of subcooling. Upon every refill of the water supply tank, water degassing was carried out by boiling and agitating the water for approximately thirty minutes.

2.1.2 The Boiling Module

Figure 2.2 illustrates the assembled boiling module showing the instrumentation used for bubble dynamics measurements (i.e., non-intrusive measurements using high speed camera (5), and intrusive measurements using optical probe (6)) while Figure 2.2b shows closely the main dimensions of the flow channel. The module consists of a machinable ceramic (Cotronics series 900) enclosure composed of two plates (1). The flow channel was constructed by gluing two quartz plates (2) on the upper ceramic plate (1) at the sides of the heated (boiling) surface (11). The quartz plates maintained the planar jet stability and helped in preventing jet inversion as water was issued from the nozzle (3). The flow channel dimensions are shown in Figure 2.3. While the optical probe tip was moved over the entire half of the boiling surface using an XYZ micrometer starting from the stagnation, the shaded area in Figure 2.3 represents the area of focus for the visual observations extends from approximately 2 mm downstream the stagnation using the high speed camera since the high light reflections in the vicinity of stagnation precluded visual observations of bubble growth in this region.

The boiling block was made of high purity copper (grade C110) with average thermal conductivity k_{cu}= 380 W/m.K over the temperature range of interest in the current research (that is between 75 ^{o}C and 130 ^{o}C). The thermal conductivity of the heated surface has been assumed constant as its value varied by only 3% over such temperature range.

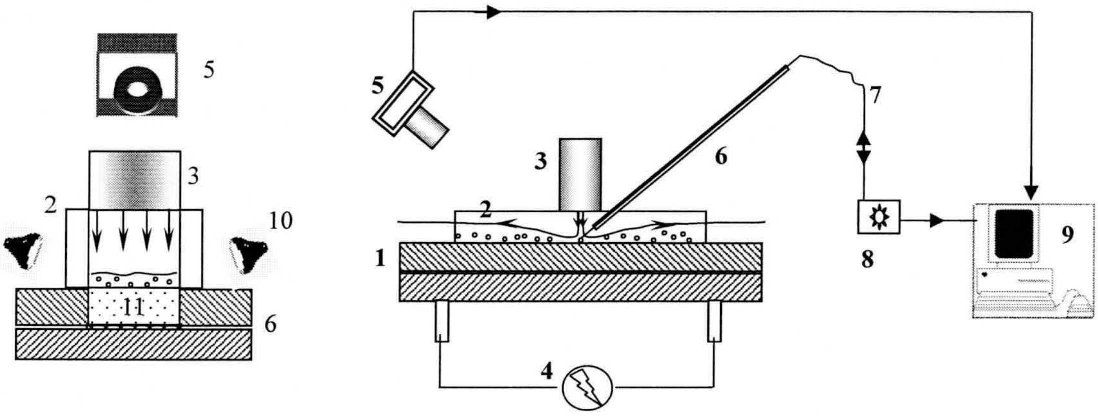

Figure 2. 2 Schematic of boiling module: 1-Ceramic plates, 2- Quartz plates, 3- Planar nozzle, 4- DC Power supply, 5- High speed camera, 6- Stainless steel tube, 7- Single mode optical fibre, 8- Laser transceiver equipment, 9- PC, 10- Light sources, 11- Heated surface

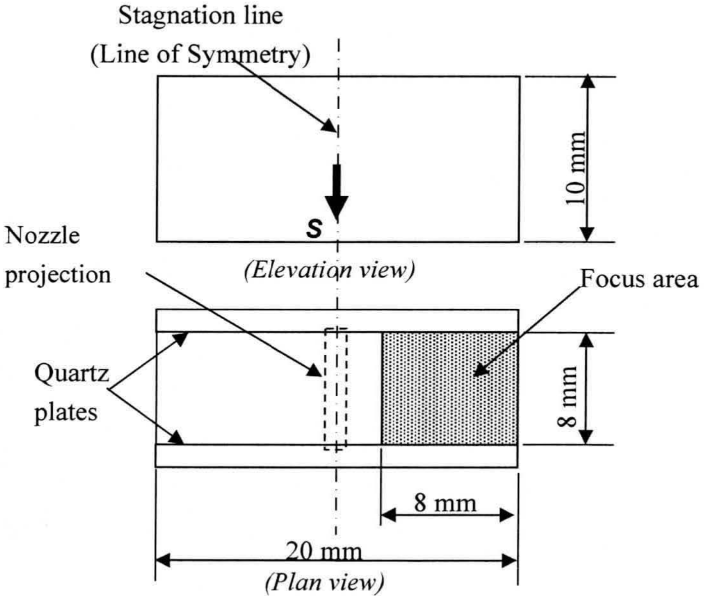

Figure 2. 3 Flow channel dimensions

Figure 2.4 shows the locations of twelve 0.52 mm diameter, holes that were drilled into the copper block at two different distances from the exposed surface, with six holes at each distance. Each of these holes was 4 mm in depth. Twelve, 0.5 mm outer diameter, sheathed, ungrounded; K-type thermocouples were inserted in these holes in order to measure the interior temperatures of the boiling block. These interior temperature readings were used to determine the surface temperature and heat flux at different locations from the jet stagnation point, point ***S*** in Figure 2.4, as discussed in the next section. In the Figure, the boiling block was cut into inverted T shape to enable minimizing the contact resistance with the heating element using the side protrusions as will be illustrated later. The average surface roughness of the exposed surface to the jet was measured before each run and was found to be less than 1 micron.

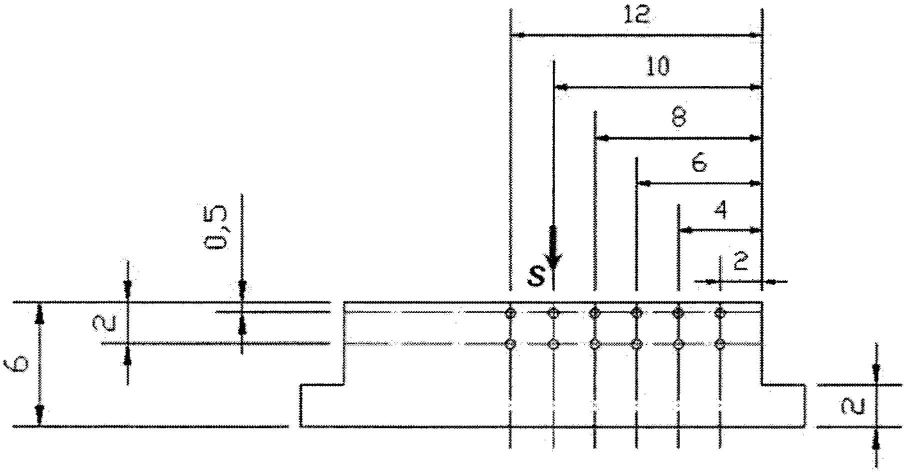

Figure 2. 4 Locations of the thermocouples installed in the copper block.
(All dimensions are in mm).

Heat was provided to the boiling block by passing direct current from a 2.6 kW

DC power supply (XANTREX XFR 20-130, 0-20V 0-130A) through a 50 microns thick NiCr 80/20 foil placed beneath the copper block. As shown in Figure 2.5, to minimize the thermal contact resistance in the assembly of the boiling module, the copper block (1) is pressed onto the foil (5) by means of pressing the upper ceramic plate(6) on the two end protrusions of the copper block. Electrical isolation from the foil was maintained by coating the copper block bottom with aluminum oxide (8). Photographs showing the assembly steps are provided in Figure 2.6 and the assembled test section with the bubble dynamics measurements instrumentations settings are shown in Figure 2.7.

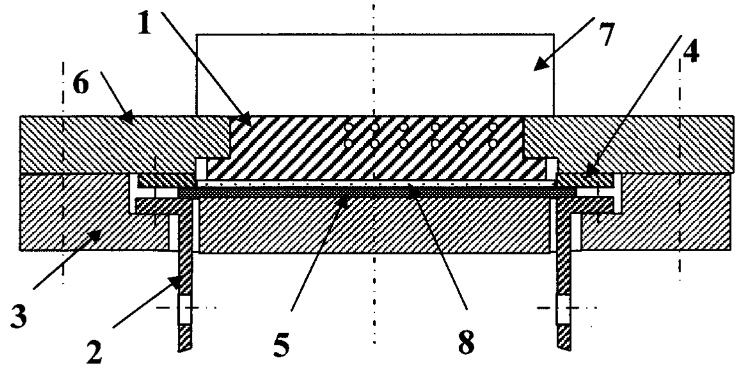

1- Boiling block, 2- Power lugs, 3- Lower ceramic plate, 4- clamps, 5- Ni/Cr foil, 6- Upper ceramic plate, 7- Quartz plate, 8- Al_2O_3 insulation layer

Figure 2. 5 Assembly of the boiling module

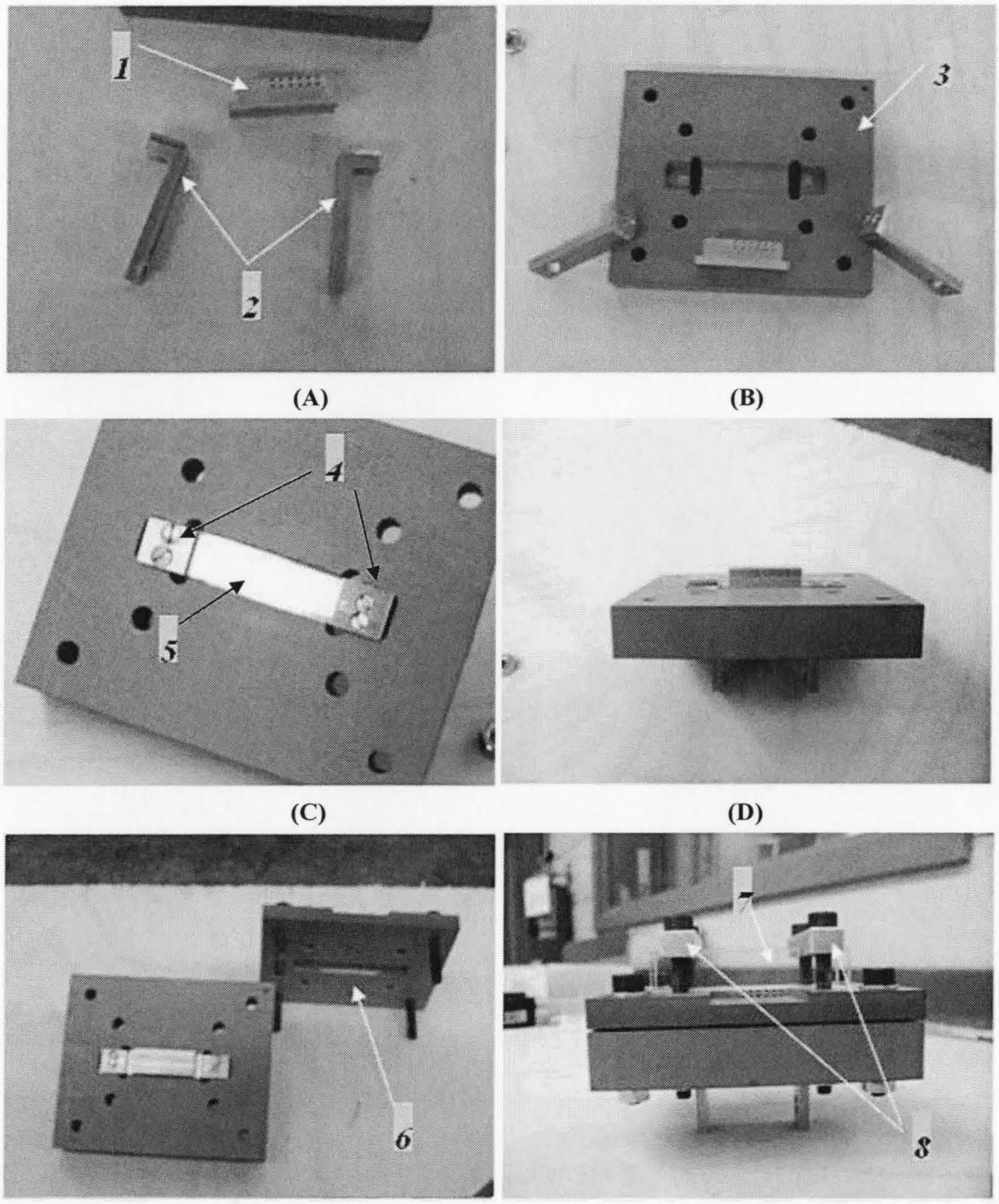

(A) (B)

(C) (D)

(E) (F)

Figure 2. 6 Photographs of boiling module assembly steps: 1- Boiling block, 2-Power lugs, 3- Lower Ceramic plate, 4- Heating foil clamps, 5- Ni/Cr heating foil (50 microns thick), 6- Upper ceramic plate, 7- Quartz side plates, 8- Quartz plates' clamps.

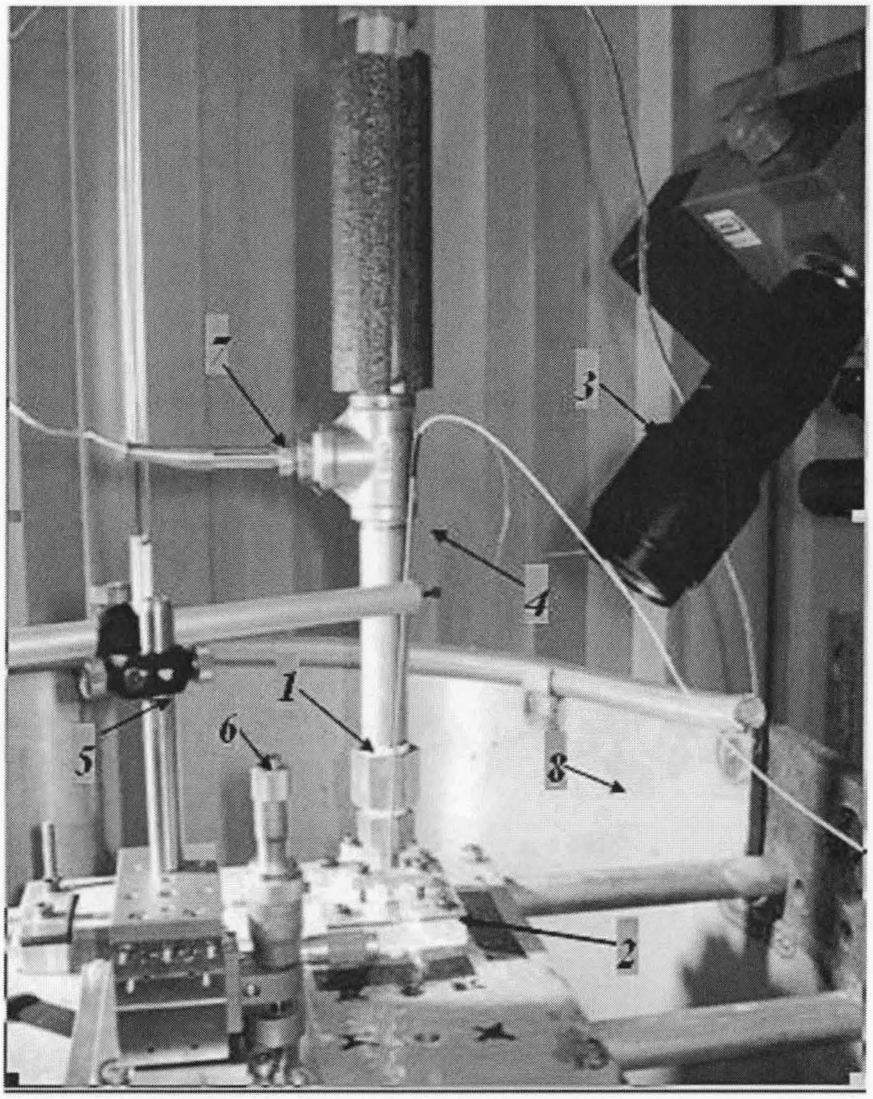

Figure 2. 7 Assembled test section with instrumentation of bubble dynamics measurements: 1- Nozzle, 2- Boiling module, 3- High speed camera, 4- Optical probe, 5- probe holder, 6- XYZ micrometer, 7- K-type thermocouple, 8- Quench tank

2.2 Analysis of Experimental Heat Transfer Data

2.2.1 Nodalization of boiling module

Steady-state readings of the copper block interior temperatures were used to determine spatial distribution of the temperature and the heat flux on the boiling surface. Interior temperature measurements were taken at distances, x, from the jet stagnation equal to 0, 2, 4, 6, and 8 mm. The temperature value at the insulated right side (i.e. at x = 10 mm) was determined using second degree polynomial fit of temperature data at x = 6 mm and x = 8 mm together with the assumption of zero gradient at x=10 mm. These readings have been used as input to a finite difference algorithm (FDA) used to determine the temperature distributions within the boiling block assuming two-dimensional steady-state heat conduction as shown in Figure 2.8.

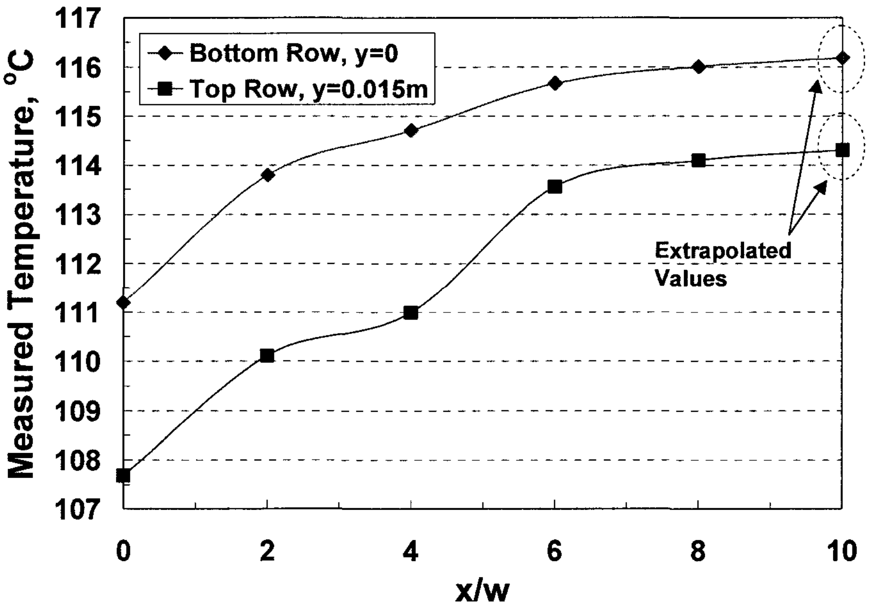

Figure 2. 8 Extrapolated temperatures at the adiabatic side of the boiling block using interior temperature measurements at the top and bottom thermocouple rows.

As illustrated in Figure 2.9, the computational domain represents one half of the boiling block (part (a) of the Figure) that is bounded by the two thermocouple rows at top and bottom. The remaining boundaries are two adiabatic sides: the left side at jet stagnation that is a line of symmetry and the right side that is insulated. The nodes of measurements, as well as the extrapolated nodes to the adiabatic side and the intermediate nodes used for numerical calculations are shown in part (b) of the Figure.

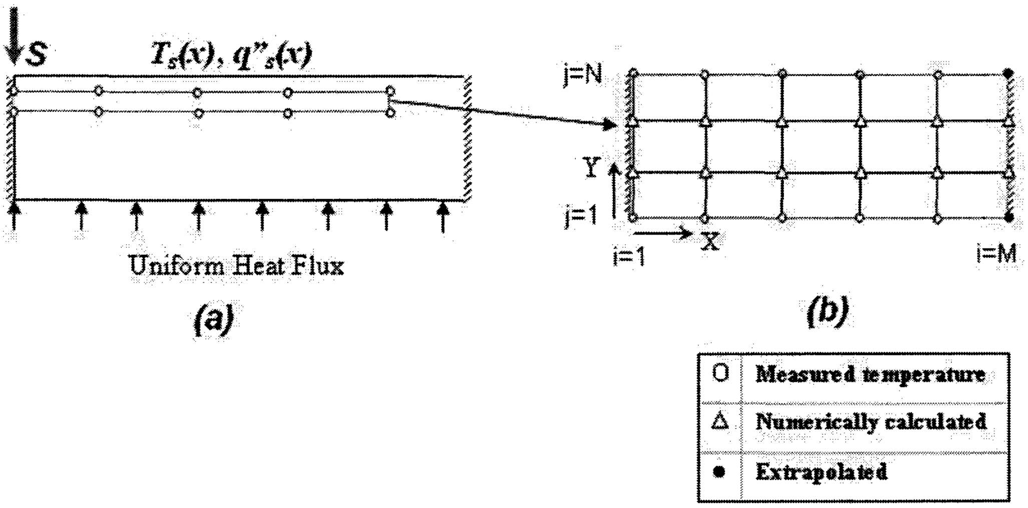

Figure 2. 9 Discretization of boiling block: (a) Physical domain representing half the block, (b) Computational domain showing nodes of: measurement, measurement extrapolations, and numerical calculation.

2.2.2 Determination of surface temperature and heat flux

The physical domain of interest within the boiling block can be represented by the following two-dimensional, steady-state, heat conduction Equation, assuming constant thermal conductivity:

$$\frac{\partial^2 T}{\partial x^2}+\frac{\partial^2 T}{\partial y^2}=0 \tag{2.1}$$

For the shown computational domain in Figure 2.10, the following boundary conditions were applied:

At x=0

$$\frac{\partial T(0,y)}{\partial x}=0 \tag{2.2}$$

At x=X=0.01 m

$$\frac{\partial T(X,y)}{\partial x}=0 \tag{2.3}$$

At y=0

$$T(x,0)=F_1(x) \tag{2.4}$$

At y=Y=0.0015m

$$T(x,Y)=F_2(x) \tag{2.5}$$

Where X = 0.01 m and Y = 0.0015 m are the dimensions of the FDA computational domain. F_1 and F_2 are temperature values determined at the top and bottom boundary of the domain using Cubic hermite data fit of temperature readings along the two thermocouple rows.

The partial differential heat conduction Equation (2.1) was converted into the following finite difference Equation:

$$\frac{T_{i+1,j}-2T_{i,j}+T_{i-1,j}}{(\Delta x)^2}+\frac{T_{i,j+1}-2T_{i,j}+T_{i,j-1}}{(\Delta y)^2}=0 \tag{2.6}$$

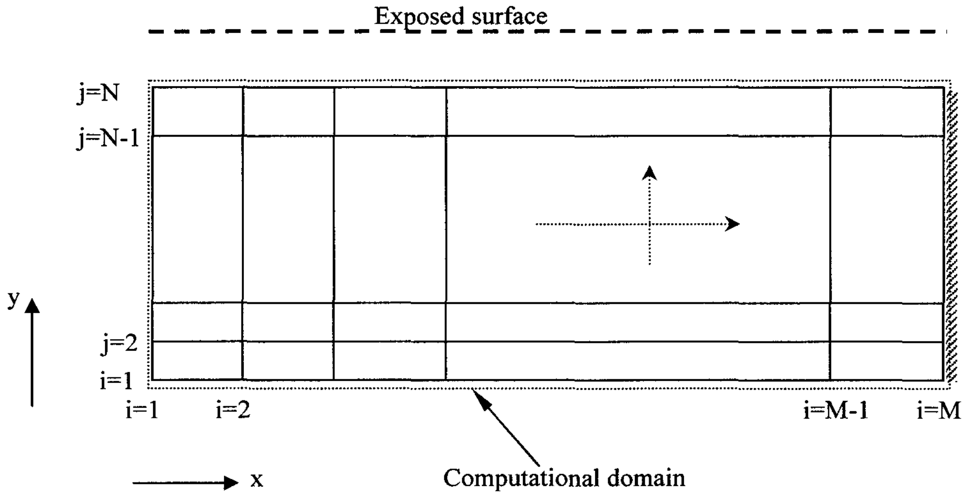

Figure 2. 10 Discretization scheme of the FDA domain

The boundary conditions in the discretized form become:

At x=0,

$$T_{-1,j}=T_{1,j} \tag{2.7}$$

At x=0.01 m,

$$T_{M+1,j}=T_{M-1,j} \tag{2.8}$$

At y=0 m,

$$T_{i,1}=T_{b,i} \tag{2.9}$$

At y=0.0015 m,

$$T_{i,N}=T_{t,i} \tag{2.10}$$

Where the subscripts 'b' and 't' refer to temperature values, measured and interpolated, at the bottom and top thermocouple rows, respectively. As shown in Figure 2.10, the exposed surface is not included in the computational domain. After the interior temperature distribution is determined, the spatial variation of the surface temperature, $T_S(x)$ in the x-direction was calculated by extrapolating the interior temperature distribution in the y-direction to the surface using the second degree polynomial shown in Equation (2.11):

$$T_s(x) = \left(a_o(x) + a_1(x)y + a_2(x)y^2\right)\Big|_{y=0.002m} \qquad (2.11)$$

Where y = 2 mm, as it is measured from the bottom thermocouple row. The coefficients $a_o(x)$, $a_1(x)$, and $a_2(x)$ were determined using the interior temperature distribution in the y-direction. The accuracy of the chosen fit was found acceptable since $R^2=1$. Figure 2.11 shows the curve fit used for the case of for the case of $V_n = 0.95$ m/s, $\Delta T_{sub} = 22$ °C, at different locations x/w from the jet, where w is the jet width.

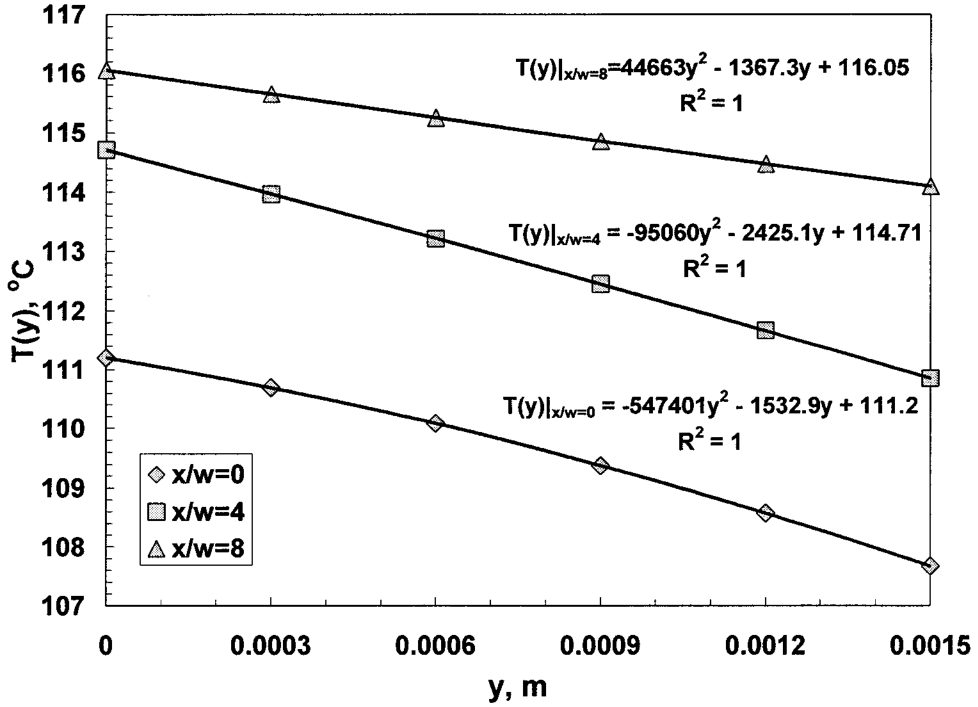

Figure 2. 11 Second degree polynomial fit of the interior temperature distribution between the two thermocouple rows.

The gradients of temperature functions represented by Equation (2.11) were used to determine the spatial distribution of the surface heat flux using Equation (2.12)

$$q_s''(x) = -k_{Cu} \left. \frac{\partial T(y)}{\partial y} \right|_{y=0.002m} = -k_{Cu}(a_1 + 2a_2(0.002)) \tag{2.12}$$

2.2.3 Validation of the results of the finite difference algorithm

Validation of the proposed FDA was conducted by comparing the predicted heat flux and surface temperature with those obtained from numerical simulations using ANSYS-CFX. In the numerical simulations of steady-state heat conduction within half of the copper block, the bottom boundary condition was exposed to a constant heat flux.

Two heat transfer coefficient profiles were assumed at the top boundary: linear and sinusoidal. Interior temperature values obtained from the simulations at the locations of thermocouples were used as input to the FDA code to calculate the heat flux distribution, which was then compared with the ANSYS-CFX simulation results. Figures 2.12 to 2.15 illustrate the agreement between the FDA code predictions of spatial distributions of surface temperature and heat flux using various data fit schemes and ANSYS-CFX numerical simulations for linear and sinusoidal heat transfer coefficient functions. The use of the cubic hermite data fit technique with the number of calculation nodes in flow direction, M=21 (Δx=0.5 mm) and that in the normal direction, N=6 (Δy=0.3 mm) points gave the best agreement with the numerical results. The deviation in the surface temperature was less than 1 % in all FDA cases where as the maximum deviation of the predicted wall heat flux from the simulation results was about 12% at the right adiabatic side, which temperature was obtained by interpolation of measured temperatures, while the average deviation of the heat flux was approximately 5% along the heated surface.

The proposed FDA results were also compared with those of an inverse heat conduction code developed by Woodfiled et al. (2006). As shown in Figures 2.13 and 2.15, the heat flux values obtained near the insulated wall using the proposed FDA are in a better agreement with the ANSYS-CFX numerical simulation results than those obtained using the inverse heat conduction code.

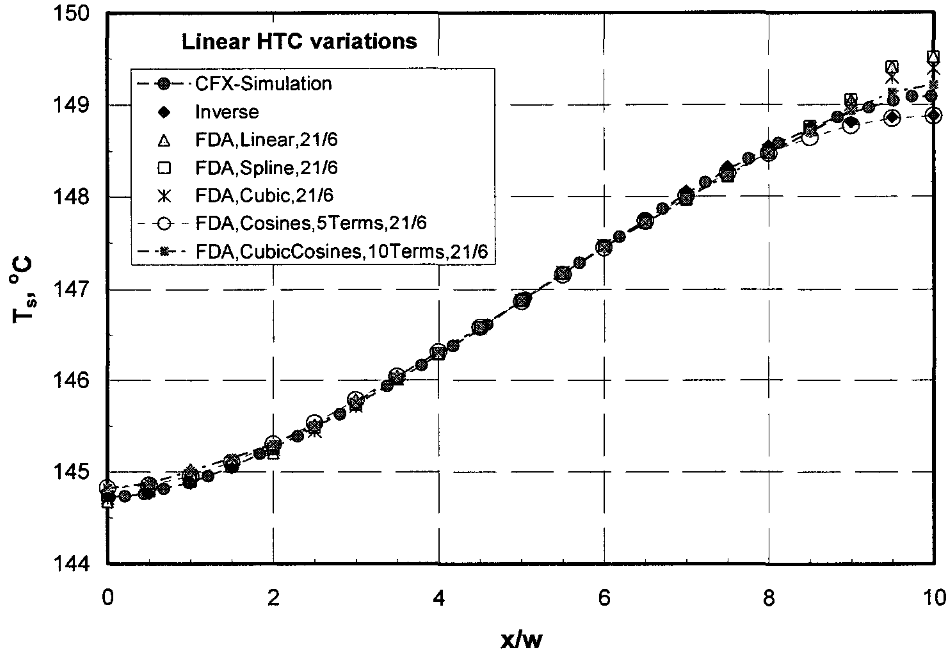

Figure 2. 12 Comparison of FDA prediction of surface temperature using various interpolation schemes (case 1- Linear surface heat transfer coefficient profile)

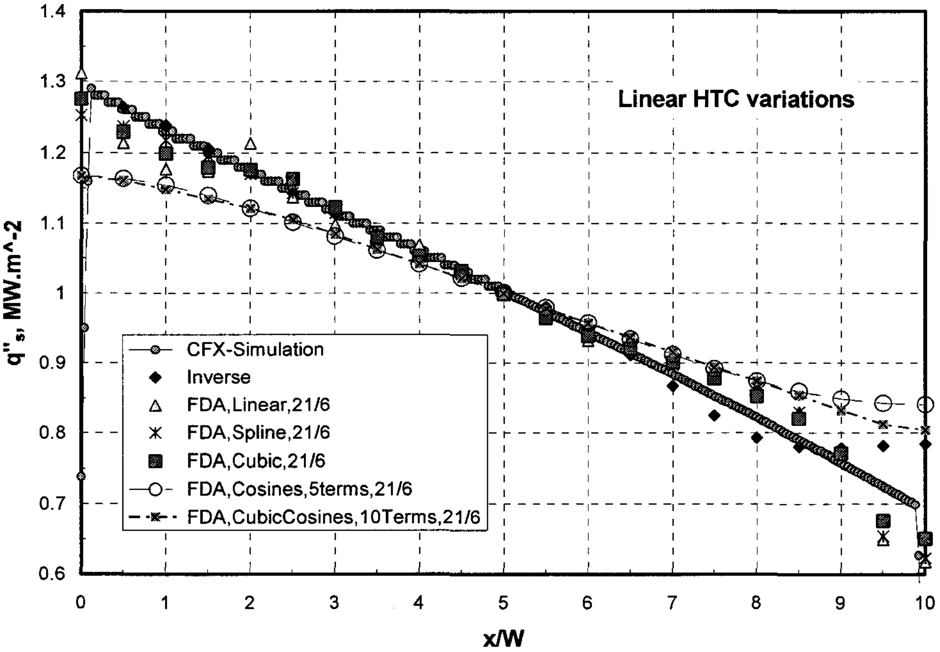

Figure 2. 13 Comparison of FDA prediction of surface heat flux using various interpolation schemes (case 1- Linear surface heat transfer coefficient profile)

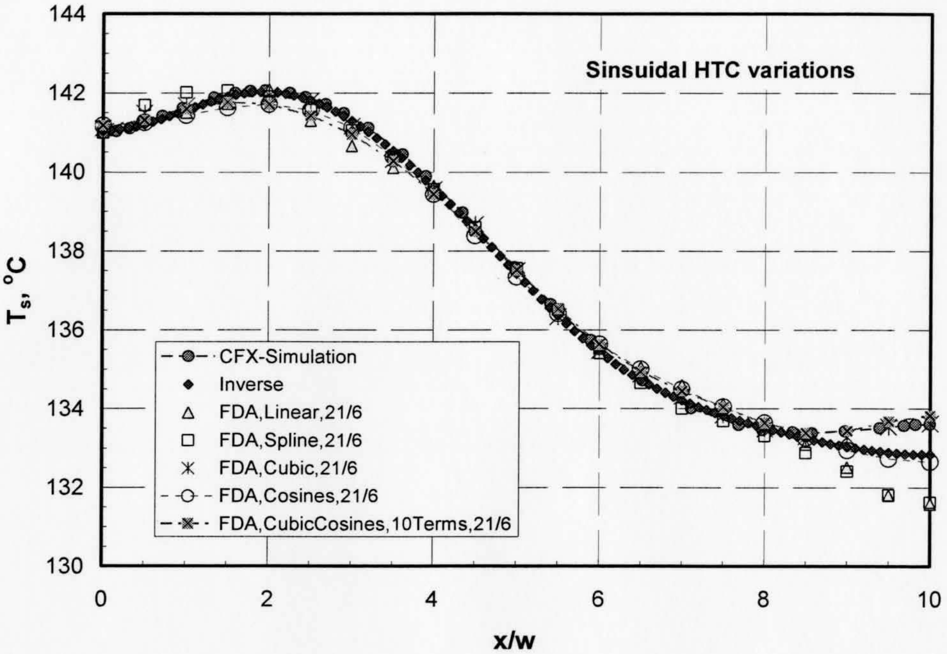

Figure 2. 14 Comparison of FDA prediction of surface temperature using various interpolation schemes (case 2- Sinusoidal heat transfer coefficient profile).

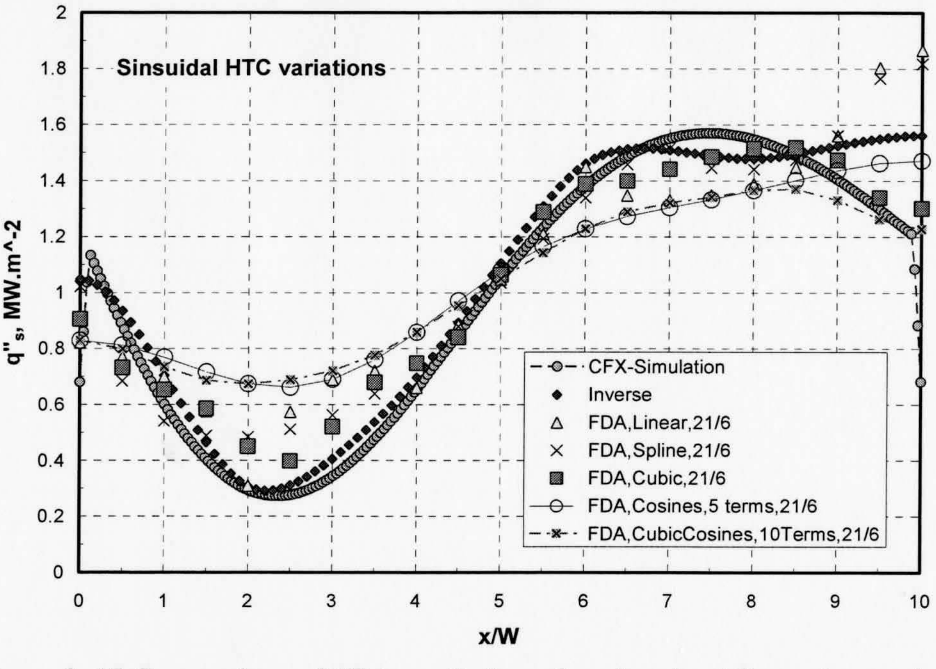

Figure 2. 15 Comparison of FDA prediction of surface heat flux using various interpolation schemes (case 2- Sinusoidal heat transfer coefficient profile).

2.3 Measurements of Bubble Dynamics

2.3.1 Intrusive measurements

An intrusive optical probe has been used to measure the frequency of bubble generation at various active nucleation sites on the heated surface. Figure 2.16 shows the structure of the intrusive optical probe. A single mode optical fiber of 900 microns clad diameter was used as the sensor. The clad of approximately 15 mm of the fiber was stripped to reduce the sensor tip to approximately 100 microns. The fiber was supported by inserting it through a 1 mm inner diameter, 200 mm long, stainless steel tube. The exposed length of the fiber to the flow was kept within 10 mm and the angle it makes with the heated surface was about 80° to achieve the following:

1- Minimizing any fiber deflection due to the flow velocity. Visual observation of the fiber deflection with the water velocity at the highest level in the current study proved the deflection to be negligible.

2- Minimizing the interference in bubble growth measurements from bubbles departing from upstream nucleation sites. With the above arrangement, only the local bubble is penetrated by the fiber tip. The oncoming bubbles from upstream locations would only bypass the probe tip and so would not affect the voltage spikes that represent local bubble growth.

The support tube was then mounted on an XYZ micrometer to adjust the location of the optical probe along the heated surface as has been shown in Figure 2.6 above.

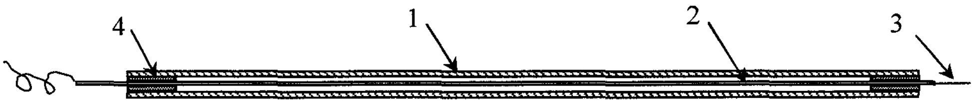

1- Steel tube (L=200mm, ID=1 mm, OD=2mm)
2- Single mode optical fiber (OD=0.9mm)
3- Fiber exposed tip (L=15mm, D=0.1 mm)
4- Packing Teflon tape

Figure 2. 16 Optical probe structure.

As shown in Figure 2.17, a laser transducer (ILX Lightwave 7900B) was used to transmit a single mode laser beam (wave length of 1558.8 nm) to a 2 x 2 light coupler (THORLABS). Due to the operational requirements of the coupler, only 50% of the light power was usable and transmitted through the probe fiber for measurements while the remaining 50% of the light intensity was dissipated into glycerin.

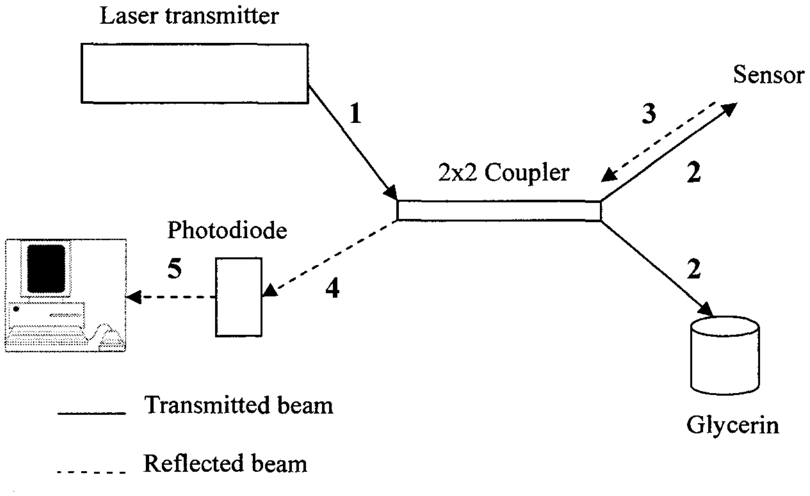

Figure 2. 17 Components of intrusive probe laser transceiver system

Only part of the useful 50% light power would reflect back through the fiber. As shown in Figure 2.18, the intensity of that reflection is determined according to the medium which the sensor tip is in contact with.

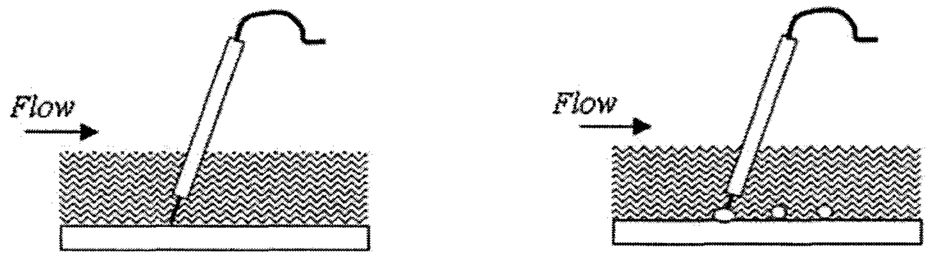

(i) Tip in liquid (ii) Tip in Vapor

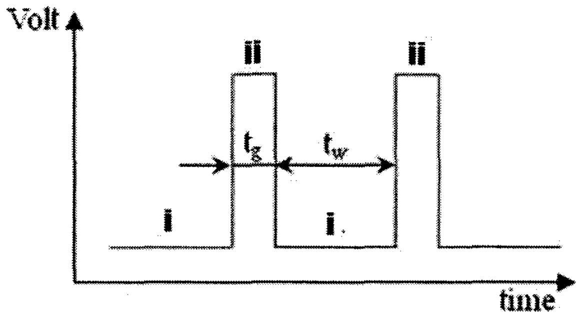

Figure 2. 18 Illustration of optical probe signal in JIB bubble dynamics measurements.

Higher intensity would be reflected back into the fiber when the tip is in contact with vapor, while liquid contact with the sensor tip would result in larger dissipation of the transmitted light, and hence less reflection back through the fiber. Light reflection was received by a photodiode (THORLABS) which was equipped with a signal amplifier and a converter of the light signal into voltage signal that was recorded to determine the bubble generation frequency and vapor contact time with the probe. The proper functioning of the optical probe was tested by repeatedly inserting and removing the fiber tip in a pool of water and observing the corresponding changes in the obtained voltage levels in both air and water. That enabled the determination of the base voltage value when the fiber tip is in contact with water. It also enabled the determination of the photodiode gain value and hence the voltage level above which the voltage values were considered to represent vapor contact with the fiber tip and not to be signal noise.

Before each experiment, the fiber tip was cleaved to remove vapor- blinded tip from a previous run as recommended by Bogdanic et.al. (2007). The optical probe signal was recorded at a rate of 250 kHz on a separate PC using an NI-PCI-6220 DAQ card. The voltage signal analysis procedure to determine the bubble release frequency and liquid and vapor contact periods (i.e., t_w and t_g, respectively) is discussed below.

The characteristics of the observed signal reflect the nature of vapor bubble generation on the heated surface in the nucleate boiling regime under jet impingement. These characteristics are the existence of only intermittent narrow spikes of high level signal within a larger base of low level signal. As shown in Figure 2.19, the short periods of time the spikes last (~ 1 ms) represent the time taken by successive bubbles to attain a maximum diameter and then depart or collapse at the nucleation site. The number of spikes per unit time represents the frequency at which bubbles appear at certain location whereas the duration of the contact represents the bubble retention time at the nucleation site from its growth onset until its collapse or departure.

To obtain the release frequency and bubble growth time, the following procedures were applied to files containing information of probe signal values recorded at a certain location on the heated surface at a certain surface superheat given the jet velocity and degree of subcooling. Sampling frequency in all measurements was 250 kHz and the physical observation time of each file has been 0.1 s which was found statistically sufficient for multiple bubble generation cycles and for convenient data handling. According to previous recommendation by Bogdanic et al. (2007) on the sufficient sampling time, for each experiment using the optical probe, recording time of bubble activity was extended for at least five seconds, i.e., at least fifty sampling files.

Procedure #1: Determination of Release Frequency (*f*):

1- As shown in Figure 2.19, the original signal was divided using a threshold voltage (V_{ts}):

$$V_{ts}=V_{min}+C_v(V_{max}-V_{min}) \tag{2.13}$$

The recommended range of C_v values is between 0.15 and 0.25. This range has been determined based on previous guidelines by Shawkat (2007) and also by manually inspecting the range of C_v over which the estimation of frequency values of an experiment would only vary within 5%.

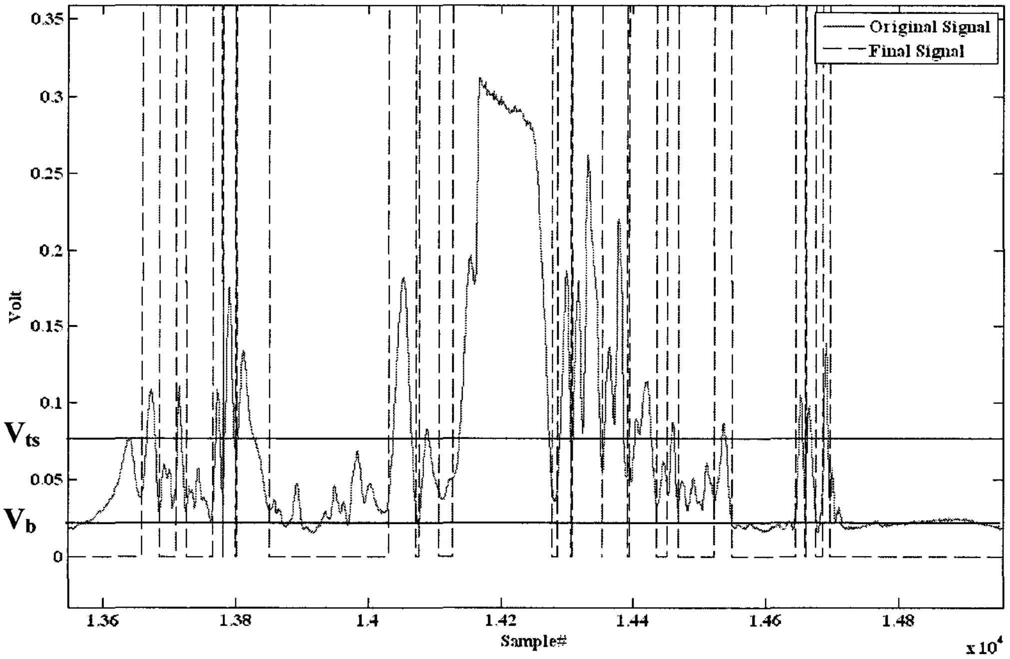

Figure 2. 19 Original vs. Final optical probe signals using spike root finding with average slopes technique (1 sample=4E-6 sec).

2- The number of spikes in a file was determined by scanning the voltage values in the file to find the points where the difference of their voltage with V_{ts} was positive while their preceding point voltage difference with V_{ts} was negative. Counting the occurrence of such condition represents how many times (N_{spikes}) crossing of the value of V_{ts} took place to initiate a spike. The bubble release frequency within the physical period of one file is thus:

$$f_i = \frac{N_{spikes}}{0.1s} \ Hz \tag{2.14}$$

3- The bubble release frequency of a given cooling condition was assumed to be equal to the average value of bubble release frequencies of the individual files:

$$f = f_{avg} = \frac{\sum f_i}{N_{files}} \tag{2.15}$$

It is worth mentioning here that with the current study being the first attempt to use intrusive measurements in free JIB at flow velocity values >1m/s, there has been high uncertainty in determining whether some of the observed spikes should be considered representative of bubble growth or only due to signal noise due to flow fluctuations around the probe tip. So, the applicable range of the threshold voltage coefficient C_v was in the majority of experiments chosen close to its higher limit, i.e., $C_V \sim 0.25$, to eliminate the inclusion of low amplitude spikes which are highly prone to be due to signal noise. That choice was well in alignment with the asymptotic variations in the frequency values within 5% as discussed above.

Procedure #2: Determination of Vapor contact time ($t_{vc}=t_g$)

The determination of vapor contact time has been a more complicated process. As shown in Figure 2.20, it is mandatory for the determination of this time period to include the rising and falling periods between a base voltage of the whole signal, V_b and V_{ts} and add them to the period between the points of intersection with V_{ts} (i.e., between A' and

B'). The following steps were applied to individual signal files to obtain the vapor contact periods:

1- The Voltage range between V_{min} and V_{max} of a file data was divided into 10 equal divisions.

2- A frequency analysis of the voltage values within each division is conducted. In all cases, the maximum frequency has been of voltage values within the lowest values division. The average voltage value within this division was taken as the signal base voltage (V_b) where the root of a spike was assumed to be located.

3- At the points of intersection of each spike with V_{ts} (A' on the rising side and B' on the falling side), Central differencing using signal values at a point before and at a point after each of A' and B' was applied to determine the average signal slopes of the signal at the intersection points (i.e., at A' and B').

4- Straight lines with the average slopes obtained in step 3 were used to replace the signal below V_{ts}, i.e., *between* each of A' and B' and the line of V_b.

5- The points of intersection between the lines obtained from step 4 and V_b line, i.e., A and B, are assumed to be the start and end points of a spike. The contact time representing a bubble growth time is thus the period between A and B. The average growth time was assumed to be the average of all contact periods in all sample files.

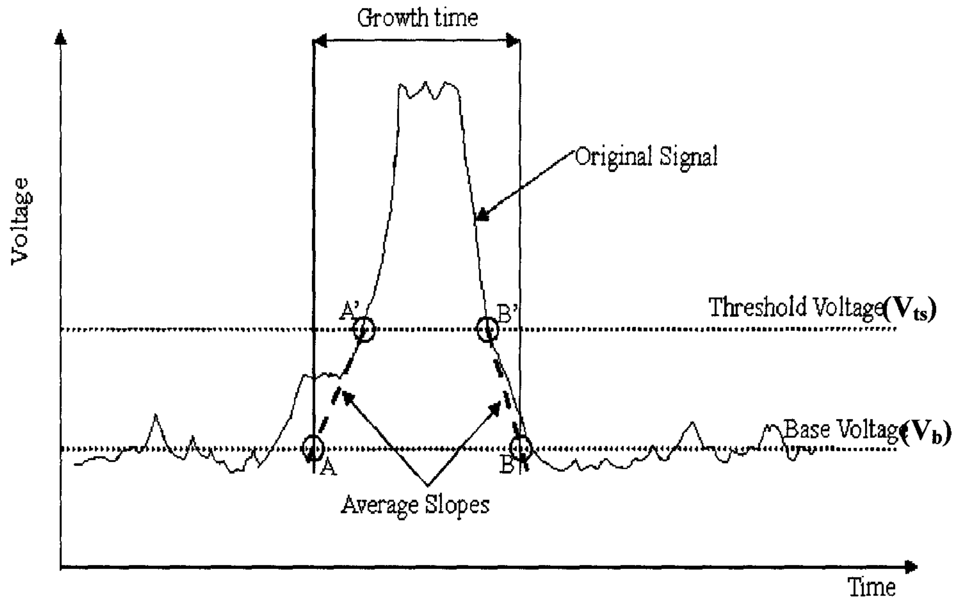

Figure 2. 20 Determination of vapour contact time using spike root finding with average slopes.

2.3.2 Non-intrusive measurements

Non-intrusive measurements of JIB bubble dynamics, i.e., bubble diameter, population intensity, and bubble motion, were conducted using high-speed video imaging. The main objective was to measure these three parameters under different flow conditions. This information is necessary to develop constitutive relations for closure of the global and subscale mechanistic JIB heat transfer models.

The high speed camera (FASTEC troubleshooter) was adjusted to 1000 frames/sec and 640 x 480 pixel/inch, for best image resolution. Two goose-neck light sources; 150 W each, were used to illuminate the flow field. By locating each lamp on one side of the flow channel, light reflections on the free surface were minimized. Figure 2.21 demonstrates the image processing steps carried out to obtain the bubble dynamics parameters.

The procedure is similar to the bubble identification procedures presented in previous studies of PFB, Maurus et al. (2002) and Ferret et al. (2004). The first step was to decompose a recorded movie into stack of images (approximately 250 frames per flow condition), Figure 2.21(a). Filtration of images was then applied to sharpen the bubble edges. A grey scale threshold was applied to convert the grey scale images into black and white images, as shown in Figure 2.21 (b), where white batches represent the bubbles. Finally, ellipses were drawn to encircle the irregular white batches and the larger diameter of an ellipse was assumed equal to the bubble diameter, Figure 2.21(c).

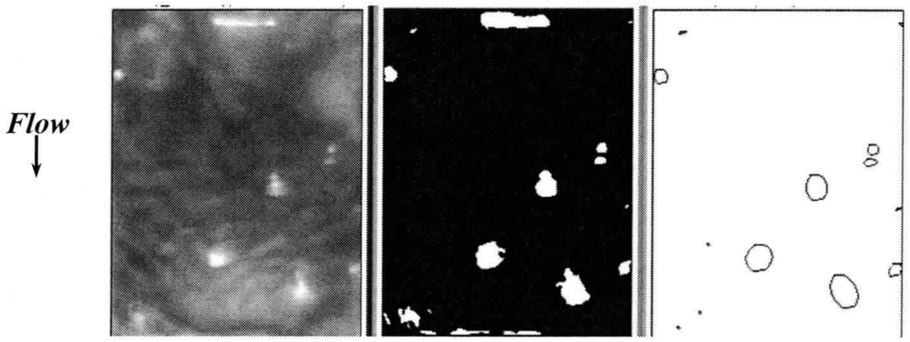

(a) (b) (c)

Figure 2. 21 Procedure of image processing: a-Original pictures from movie, b-Processed B&W pictures, and c- Final pictures with ellipses representing bubbles

The representative value of the bubble diameter under a given flow condition was determined as the most probable diameter value in all the images. Bubble population was determined by taking the average bubble count of all images. Bubble motion within the fluid bulk was determined by tracking the life cycles of individual bubbles in a sequence of images.

Unlike the case of PFB flow field, in free JIB the image sides needed to be cropped to remove light reflections at the intersection between the heater and the side glasses. Similar reflections were also observed in the vicinity of the stagnation. A condition of minimum white batch circularity of 0.75 was used to filter out these reflections from the bubble count where the circularity is defined as the ratio between the smaller and the larger diameter of an ellipse drawn around the white batch.

2.4 Experimental procedure

Prior to each experiment the boiling surface was cleaned by sanding using an Emry paper #1200 in one direction for about 1 minute and then washed with acetone. The purpose of this step was to maintain the initial condition of the surface for all experiments and to minimize the effect of oxidation on the nucleation process. This step did not affect the surface roughness which remained less than 1 micron over the entire course of experiments. The quartz plates were cleaned with wet cloth with acetone to allow for clear illumination of the flow field.

The following steps were conducted in each experiment:

1- Water temperature and impingement velocity were adjusted using the immersion heater in the water tank, and a needle valve at the nozzle inlet, respectively. Both parameters were monitored throughout the run for re- adjustment if necessary. Sample time variation of the flow meter readings during a full experimental run is shown in Figure 2.22 below for case nominal jet velocity of 0.75 m/s. With the exception of the first few seconds when the flow was initiated, the standard deviation in the velocity readings has been within ±0.0045 m/s or ±0.65% of the average velocity. The reading of the jet velocity was stopped and restarted intermittently during the experiments to refresh the computer buffer. Therefore, at the restart of the velocity reading program, some drift in the velocity readings appeared. Due to the relatively small number of such readings as compared to the whole sample that extends over an hour of readings at 50 Hz, they were not considered in the calculation of the mean jet velocity and the corresponding deviation. Similarly, the fluctuations in the water temperature have been within ±1 °C of the nominal values.

2- The heated surface temperature was adjusted using a proportional controller of the power supply output. The controller adjusts the power supply output based on the difference between the temperature reading of the farthest thermocouple inside the copper block from the jet stagnation and a pre-selected set temperature input into the controller.

3- After reaching a steady-state, readings of the block thermocouples were recorded at 50 Hz for thirty seconds.

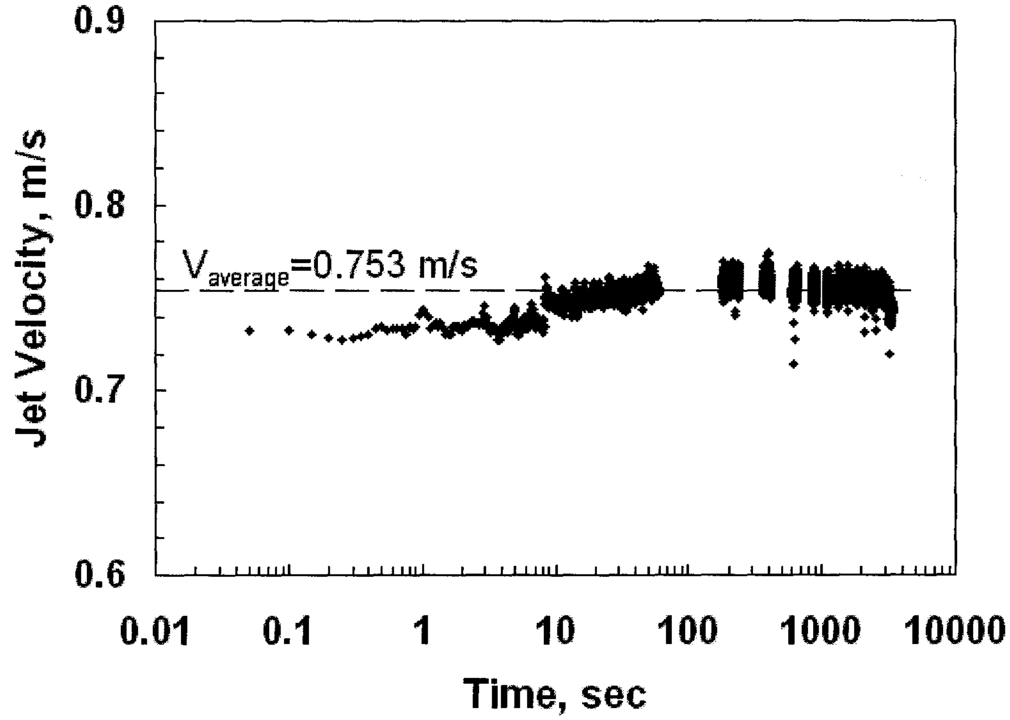

Figure 2. 22 Jet velocity variations during a full experimental run

4- Movies were recorded at one side of the heated surface. On the other side, bubble generation frequency was measured by moving the optical probe to individual active sites using the XYZ micrometer. The recording time was at least 5 seconds for every combination of flow velocity, water subcooling and surface superheat.

5- Boiling data over the entire nucleate boiling regime was obtained by increasing the set point temperature by increments of 2 to 3 °C and repeating steps 2, 3, and 4.

2.5 List of Measured Parameters

A summary of all measured parameters and techniques used in the current experimental investigation is provided in Table 2.1.

Table 2. 1 Summary of techniques to determine various JIB parameters.

No.	Parameter	Measurement/ Calculation techniques
1.	Local wall temperature, $T_s(x)$	Extrapolation of interior temperatures.
2.	Local wall heat flux, $q_s(x)$	From the gradient of interior temperature distribution normal to the heated surface, using finite difference analyses (FDA).
3.	Onset of nucleate boiling (ONB)	Visual observation of the flow domain, and Change of the slope of the boiling curve.
4.	Bubble diameter (D_b)	High speed imaging. Equals the average of maximum diameters identified in all images recorded for specific flow conditions.
5.	Active nucleation site density (N_a)	High speed imaging. Equals the average bubble count of all images recorded for specific flow conditions.
6.	Bubble release frequency (f)	Number of optical probe signal spikes per unit time.
7.	Bubble growth time (t_g) and wait time (t_w)	The width of an optical probe signal spike represents the growth time. The average wait time is calculated from the frequency and average growth time data.

Chapter 3

EXPERIMENTAL INVESTIGATIONS OF JIB CHARACTERISTICS

3.1 Introduction

In this chapter, experimental investigation findings of single-phase and boiling heat transfer under jet impingement in open channel are presented. The aim of the present experimental investigation has been to support the development of JIB heat transfer models, which are presented in the following chapters. This support has been provided by, first, providing a physical understanding of: (1) the characteristics of jet impingement flow field in open flow channels, (2) the spatial distribution of single-phase and boiling heat transfer rate, and (3) the effect of jet velocity, subcooling and surface superheat on bubble dynamics parameters (bubble frequency, maximum bubble diameter, bubble motion, and population intensity. Second, the experimental findings have been used to develop constitutive sub-models of heat transfer and phase change parameters for closure of the developed JIB heat transfer models in the subsequent chapters.

The spatial distribution of the heat transfer rate has been obtained using the interior temperature measurements and the FDA algorithm described in chapter 2. Bubble generation characteristics have been obtained using the single fibre optical probe and the high speed video imaging.

Table 3.1 lists the ranges of the jet velocity (V_n), degree of subcooling (ΔT_{sub}), degree of superheat (ΔT_{sup}), and dimensionless location from the stagnation point (x/w), where *w* is the jet width, considered in the present experimental investigation.

Table 3. 1 Range of Jet and Surface Parameters considered in this study

Parameter [*Unit*]	**Range**
V_n [m/s]	0.4, 0.55, 0.75, 0.95, 1.25, and 1.7
ΔT_{sub} [^oC]	10, 15, 22, and 28
ΔT_{sup} [^oC]	-25 to 30, (increment of 2 to 5 °C)
x/w [-]	0, 2, 4, 6, and 8, 10.

Bubble dynamics have been investigated under the various cooling conditions listed in Table 3.1 Selection of the set of experiments used in the development of the constitutive sub-models of the bubble dynamics parameters was based on the clarity of images, consistency and repeatability of the optical probe signal and the range of cooling conditions covered in these experiments.

3.2 Jet Impingement Single Phase Heat Transfer Coefficient

The values and distribution of the single phase heat transfer coefficient were determined by conducting experiments in the single phase heat transfer regime, where the maximum surface temperature was kept below the liquid saturation temperature ($T_{s,max}$ = 95 °C). As the local wall heat flux, q_x'' and the local surface temperature, $T_{s,x}$ at distance x from the stagnation were determined using the finite difference analysis (FDA) of the steady-state interior temperature distribution in the copper block, the local heat transfer coefficient was obtained using Newton's law of cooling:

$$h = \frac{q_x''}{(T_s - T_l)} \tag{3.1}$$

A unified sub-model of the single phase heat transfer coefficient that can be applied to the entire heater length has been developed. An empirical correlation has been developed for the stagnation heat transfer confident, h_o at $x=0$. A multiplier coefficient that accounts for the spatial variations of the heat transfer coefficient at x/w>0 has also been developed. The proposed correlation of the stagnation heat transfer coefficient is given in Equation (3.1)

$$Nu_{o,w} = \frac{h_o w}{k_f} = 0.68\,\mathrm{Re}_w^{0.53}\,\mathrm{Pr}^{0.375} \tag{3.2}$$

In Equation (3.2), the water properties were calculated at the film temperature; i.e., the average of the jet water temperature and the stagnation surface temperature. The characteristic length used to determine *Re* was the jet width, *w*. Figure 3.1 shows that Equation (3.2) correlates the experimental data of the heat transfer coefficient at the stagnation point within ±15%. This correlation has provided prediction than the next most suitable correlations such as that by Inada et al. (1981) where the predictions were within ±35%

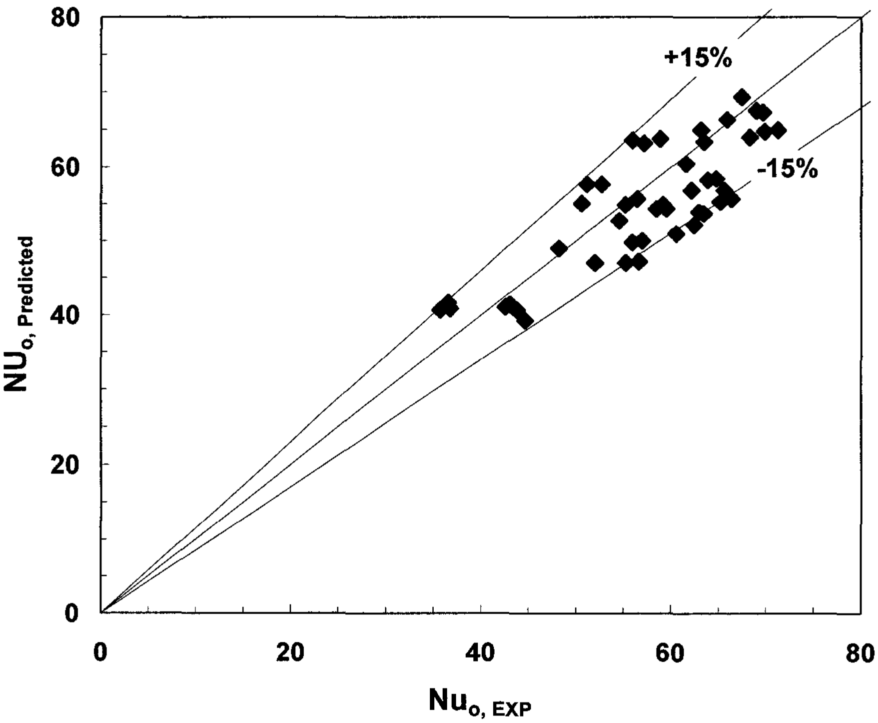

Figure 3. 1 Prediction of stagnation single phase heat transfer coefficient

The spatial distribution of the local heat transfer coefficient is shown in Figure 3.2. This data shows secondary peaks downstream of the stagnation point.. Schafer et al. (1991) and Duckle and Hollingworth (1996) observed and reported such *wavy* distribution. . However, Schaefer et al. (1991) did not provide any mathematical formulation of such distribution. Duckle and Hollingworth (1996) developed a correlation of the spatial distribution of the single phase heat transfer, only downstream of the secondary peak.

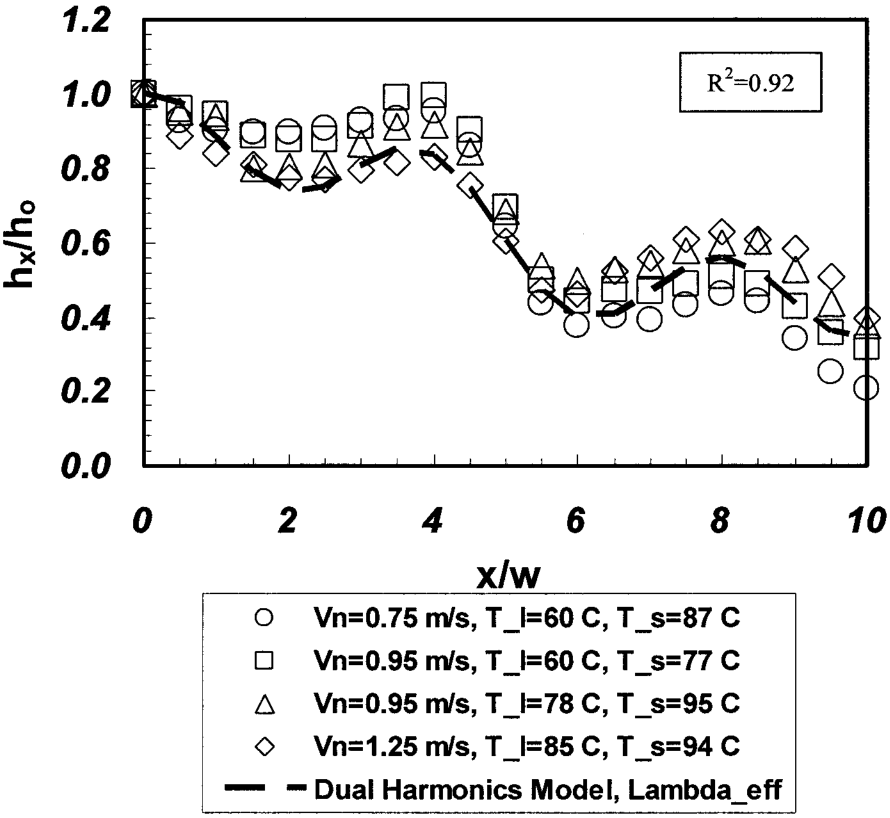

Figure 3. 2 Spatial distribution of the single phase heat transfer coefficient.

It has been postulated in the current study that the flow direction does not become parallel to the heated surface immediately after impingement. Rather, there are fluctuations in the velocity direction with the heated surface in cycles with decaying amplitude of the angles at which the flow direction deviates from parallelism with the heated surface. This creates points along the heated surface where the shear stress and the heat transfer coefficient experience peaks and valleys in their magnitudes along the surface. The distribution of the local heat transfer coefficient shown in Figure 3.2 indicates the existence of two peaks. These peaks have been consistently observed in all experiments at x/w~4 and at x/w ~ 8. Accordingly, a correlation using regression analysis has been developed to model the observed variations of the heat transfer coefficient.

It is suggested that for a correlation to capture the observed variations of the local heat transfer coefficient it should include a shape factor, λ_{eff} that is composed of two trigonometric functions, λ_1 and λ_2 such that:

$$\lambda_1 = [0.33 \cdot \cos(0.5\pi \frac{x}{w}) + 0.67] \cdot e^{(-0.015\frac{x}{w})} \tag{3.3}$$

$$\lambda_2 = [0.25 \cdot \sin(0.2\pi \frac{x}{w}) + 1] \cdot e^{(-0.148\frac{x}{w})} \tag{3.4}$$

The values of the frequencies in the two trigonometric functions in Equations (3.3) and (3.4) were deduced from the needed variation in the shape factor to resemble the heat transfer coefficient profile with the observed two peaks. On the other hand, extensive trials have been conducted manually to determine the values of the coefficients of the trigonometric functions and the exponents to obtain good agreement with the experimentally obtained ratios between the local heat transfer coefficient downstream the stagnation and the corresponding values right at the stagnation.

The local heat transfer coefficient can be determined using the stagnation heat transfer coefficient value and the value of λ at the location of interest from Equation (3.5):

$$\frac{h_x}{h_o} = \lambda_{eff} = 0.4\lambda_1 + 0.6\lambda_2 \tag{3.5}$$

Figure 3.3 shows the variation of each of the two trigonometric functions as well as the resultant double peak shape factor with the distance from the jet stagnation. The proposed heat transfer coefficient shape factor is applicable only for the range between x/w=0 and x/w=10.

In the following paragraphs, it is attempted to explain what could be the reasons for the observed double peaks in the heat transfer coefficient. Based on the proposal of the double peak shaper factor in Equation (3.5) to model those peaks, it is postulated that two factors contributed to this distribution:

1- The fluctuations in the flow direction with respect to the heated surface downstream the stagnation. It is postulated that the flow velocity does not become completely parallel after impingement. Rather, there would be a length over which the flow direction slightly fluctuates in detachment-reattachment like motion with respect to the heated surface. Consequently, this would produce fluctuations in the shear stress and the heat transfer coefficient values. This cycle of direction changes is thought to be the main contributor to the observed secondary peaks and is accounted for by λ_1.

2- The second trigonometric function, λ_2 accounts for the decay in the heat transfer coefficient due to the boundary layer growth and so it has monotonically decaying shape with x/w.

A lower agreement of ±15%, was observed in the range of $0 < x/w < 2$ and at the far end of the plate (i.e., at x/w~10). However, a better agreement, within ± 8%, was obtained between the two peaks (i.e., at $4 < x/w < 8$). The location of the two peaks has been accurately captured by the proposed shape factor and the stagnation heat transfer coefficient as calculated from Equation (3.2).

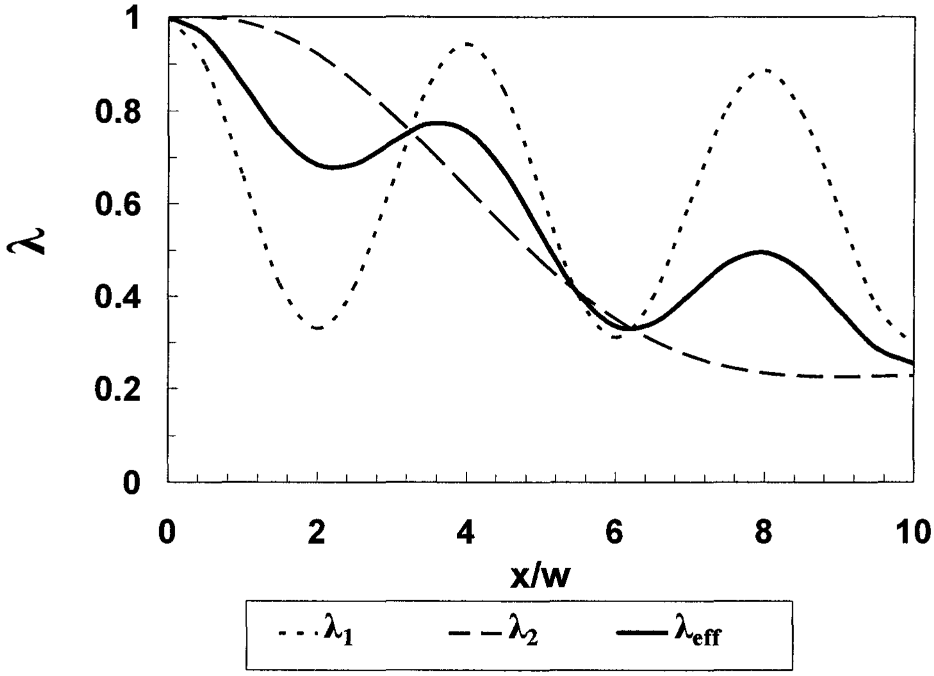

Figure 3. 3 Components of the normalized heat transfer coefficient shape factor consisting of two trigonometric functions.

3.3 Variation of Liquid Film Thickness in Jet Impingement Flow

The liquid film thickness is expected to vary with the jet velocity. An increase in the jet thickness would be accompanied with flow deceleration for the same mass flow rate through the flow channel. In the current study, the level of flow deceleration was found to increase with the reduction in the flow velocity. At lower jet velocity than approximately 1 m/s, a noticeable increase in the film thickness was observed which also indicated a buildup of the liquid hydrostatic pressure.

So, it could be postulated that such an increase in the liquid thickness is a flow adaptation to increase its hydrostatic pressure to overcome wall friction and to drive the flow further downstream the flow channel. Moreover, the location of the maximum film thickness was observed to become closer to the stagnation as the jet velocity was reduced. With the reduction in jet velocity, the initial flow kinetic energy is reduced and hence such flow adaptation is called upon earlier in channel to mitigate the early depletion of the jet kinetic energy against the friction. Under steady flow conditions, the formation of such *hydraulic jump* within the flow field is expected to decelerate the flow velocity and hence affects the characteristics of the single phase and nucleate boiling heat transfer. It would also affect bubble dynamics at various locations along the heated surface. Figure 3.4 shows the two characterizing parameters of the hydraulic jump. These parameters are the location of the hydraulic jump, X_{hj} and the liquid film thickness,

δ_2, downstream of the jump which determines the corresponding mean film velocity, U_2. In the visual observations of the flow field in the current study, the film thickness has been of uniform thickness at much larger values than the jet thickness at jet velocities of 0.4 m/s and at 0.56 m/s. These conditions are thus believed to have caused an early jump in the flow field that it can cover the entire heated surface length.

The location of the hydraulic jump has been measured together with the corresponding downstream liquid film thickness using a needle mounted on the XYZ micrometer that was used to adjust the optical probe location on the surface. The contour of the free surface was tracked by moving the needle in vertical direction away from the heated surface until a disturbance to the free surface is observed indicating that the needle is leaving the liquid bulk. The distance at which the disturbance is observed denotes the liquid film thickness δ.

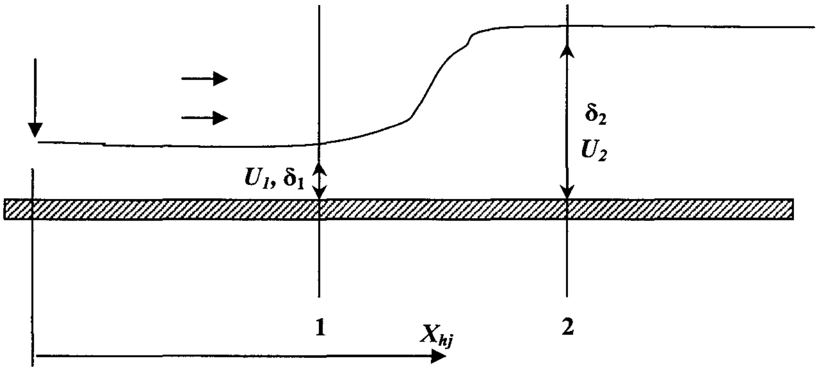

Figure 3. 4 Hydraulic jump in jet impingement flow field.

The needle tip was then moved in the flow direction to determine the variation in δ at various locations from the stagnation. The hydraulic jump location, X_{hj} was associated with noticeable change, i.e., increase, in the value of δ as shown in Figure 3.4. The distance, X_{hj}, was correlated in terms of the jet velocity as given in Equation (3.6).

$$\frac{X_{hj}}{w} = 6.51 \cdot V_n^{2.67} \tag{3.6}$$

Based on the variation of the liquid film thickness with impingement velocity shown in Figure 3.5, the following correlation has been developed to determine δ_2:

$$\frac{\delta_2}{\delta_1} = 1 + 30.4e^{-3.25V_n} \tag{3.7}$$

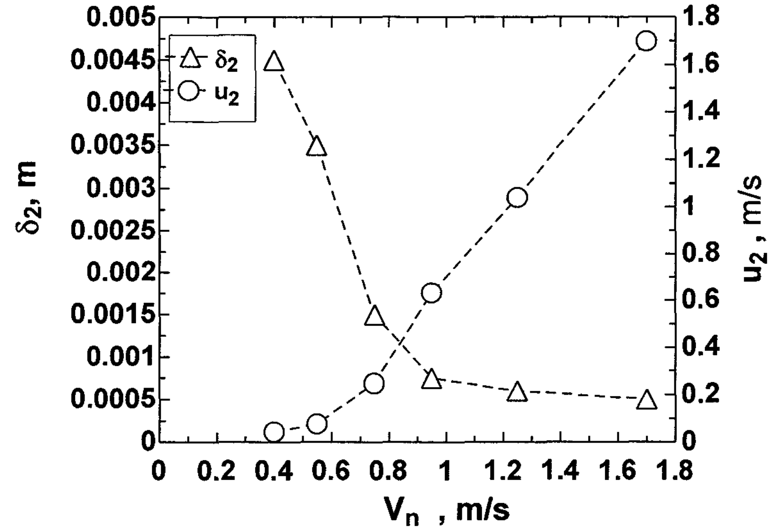

Figure 3. 5 Distribution of the mean film thickness and average velocity downstream of the hydraulic jump as a function of the jet velocity.

As the water jet is issued into stagnant air, and since the jet flows under gravity in downward direction, there is an increase in kinetic energy which results in reduction of the jet thickness. The average reduction in jet thickness is 16% for the range of jet velocities of the current study. However, as jet velocity reaches zero upon stagnation, as flow accelerates again in the parallel direction to the heated surface, the maximum velocity that it can hypothetically reach would be that at the nozzle, V_n.

If that would be the case, the flow could be approximated to have been divided into halves each of thickness equal to half the jet width, w/2. Similar assumption has been made by Liu and Lienhard (1992) in the analysis of single-phase planar jet flow filed. By assuming the liquid film thickness upstream a hydraulic jump to be equal to half the jet width, i.e., $\delta_1 = w/2$ and by, applying the conservation of mass between sections 1 and 2 in Figure 3.4, U_2 can be determined from:

$$\frac{U_2}{U_1} = \frac{\delta_1}{\delta_2} \tag{3.8}$$

3.4 Jet Impingement Boiling Curve

3.4.1 Effect of Jet Parameters on Boiling Curve

One of the main objectives of this work is to investigate the effect of jet velocity, water subcooling and surface superheat on the boiling curve. The aim of such investigation is to develop a sub-model that would be able to determine the degree of superheat corresponding to the onset of nucleate boiling, ΔT_{ONB} under JIB. The determination of ΔT_{ONB} is essential for the development of the bubble dynamics sub-models needed for the JIB heat transfer model. Figure 3.6 shows a typical JIB curve under including the single-phase and nucleate boiling regimes.

Three slopes designating three regimes can be easily identified in Figure 3.6. The least slope is associated with single phase heat transfer where no bubbles are generated on the heated surface.

An increase the wall degree of superheat would result in the appearance of few bubbles on the surface that interrupt the thermal boundary layer and agitate the liquid film in the vicinity of the heated surface. The formation of the bubbles results into an increase in the heat transfer coefficient.

In the partial boiling regime, bubble generation is intermittent with only few isolated, distant, bubbles growing on the surface to relatively small sizes. In most cases the bubbles remained attached to the surface before they eventually disappeared. Increasing the degree of superheat further causes boiling to become more vigorous with more bubbles generated resulting in a further increase in the slope of the boiling curve.

Figures 3.7 and 3.8 show the variation of the heat flux and heat transfer coefficient with the jet velocity and degree of subcooling The vertical lines on Figures 3.7a and 3.7b refer to the boiling onset surface superheats at two different velocities. It should be noticed that the heat transfer coefficient was determined using the overall temperature difference between the heated surface and the water at the stagnation.

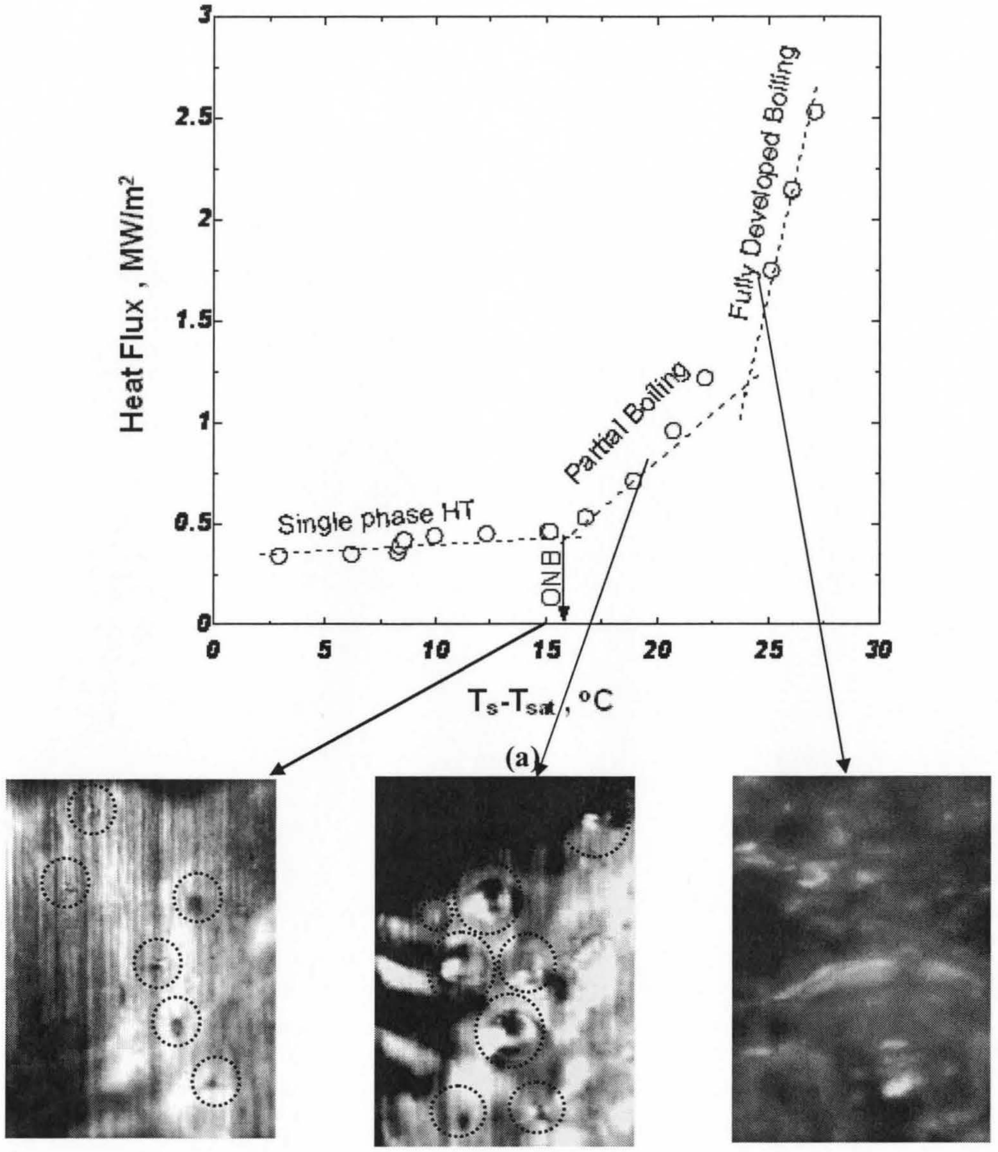

(a)

(b)

Figure 3. 6 (a) JIB curve at x/w = 6 in the case of V_n=1.25 m/s and ΔT_{sub}=22 °C. (b) bubble size and population intensity)

In Figure 3.7a, the boiling onset has been identified as the point of intersection between the two straight lines representing the trends of the single-phase and nucleate boiling regimes, respectively. Figure 3.7b allowed better determination of this parameter as it is the temperature at which the value of the heat transfer coefficient has first changed from its approximately constant value in the single phase regime denoting an improvement due to bubble generation.

It is concluded that an increase in jet velocity from level 0.75 m/s to 1.25 m/s has shifted the onset of nucleate boiling from a wall superheat of 9 °C to 16 °C, while the degree of subcooling was maintained at 15 °C. This trend is expected as increasing jet velocity reduces the thickness of the momentum and thermal boundary layers, White (1996), which under constant temperature difference would dictate steeper gradient at the wall denoting higher heat transfer rate. On the contrary, this has adverse impact on bubble nucleation as reducing the thickness of the superheated liquid with the velocity would result in suppressing the bubble growth. Hence, bubble nucleation would start at higher surface superheat, Rohsenow et al. (1998). In addition, bubble growth is also suppressed due to the increase of condensation heat loss to the liquid bulk at higher flow velocity, Unal (1976).

Increasing the degree of subcooling from ΔT_{sub} = 15 °C to ΔT_{sub} = 28 °C as indicated in Figure 3.8 resulted in an increase in the ΔT_{ONB} from 9 °C to 18 °C. This is again in accordance with the expectations of the physical interpretation of the JIB process. Increasing the degree of Subcooling results in an increase in the temperature gradient (hence in the heat transfer rate) at a given velocity (boundary layer thickness is maintained) and wall superheat. Again the increase in subcooling results in reduction in the thickness of the boundary layer where superheated liquid exists. Higher surface superheat would be needed to initiate and sustain bubble nucleation and growth.

By comparing Figures 3.7 and 3.8, it is concluded that in the current study, the increase in wall heat flux due to the increase in forced convection heat transfer at the higher jet velocity can be offset at the lower jet velocity in the nucleate boiling regime by early, and then more intense bubble generation. Same offset can be obtained by changing the liquid subcooling. For given wall superheat and velocity, the increase in temperature gradient at higher subcooling is offset by flow agitation due to early bubble generation at the lower subcooling. As shown in Figure 3.8b, the heat transfer coefficient at the lower subcooling could be as high as twice the value at the higher subcooling obtained at the same wall superheat and jet velocity.

In addition to the wall superheat, other surfaced conditions such as the surface roughness and material could also affect the overall heat transfer such as the nucleation density, Hahne et al. (2006). In the study by Shoukri et al. (1978) the effect of surface conditions on the increase of the pool boiling heat flux has been represented in terms of bubble flux density which depends on the number active nucleation sites density and frequency of bubble emission from the existing cavities on the surface, which in turn depends on the size and shape of those cavities. Another influence on the overall heat flux due to bubble nucleation is the enhanced liquid flow due to the induced liquid motion around a growing bubble by surface tension variations, termed as Marangoni effect, Petrovic et al. (2004). This effect is considered to be highly important in situations of pool boiling in reduced gravity environment, where the Marangoni effect is comparable with the buoyancy induced flow relative to the heated surface. In forced convection boiling, this effect is yet being overlooked due to the significantly small surface tension induced flow velocity with respect to the bulk flow velocity. In the current study, only the effect of nucleation density on the heat transfer coefficient has been considered as will be discussed in Chapter 6 for the range of jet flow velocity. Both material and surface roughness effect were out of the scope of the current study and only single material type, Copper, and surface roughness level were used throughout the experimental investigations, where the surface roughness was maintained below 1 micron.

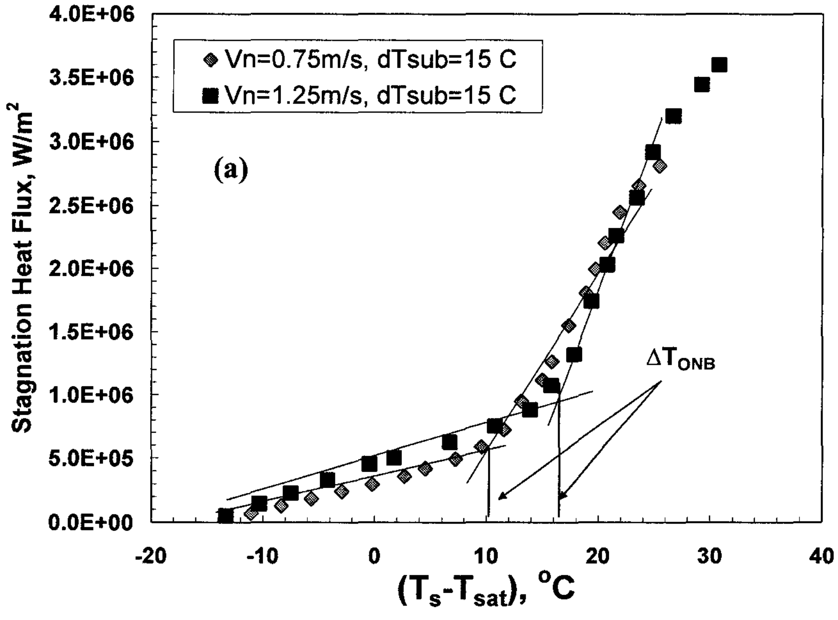

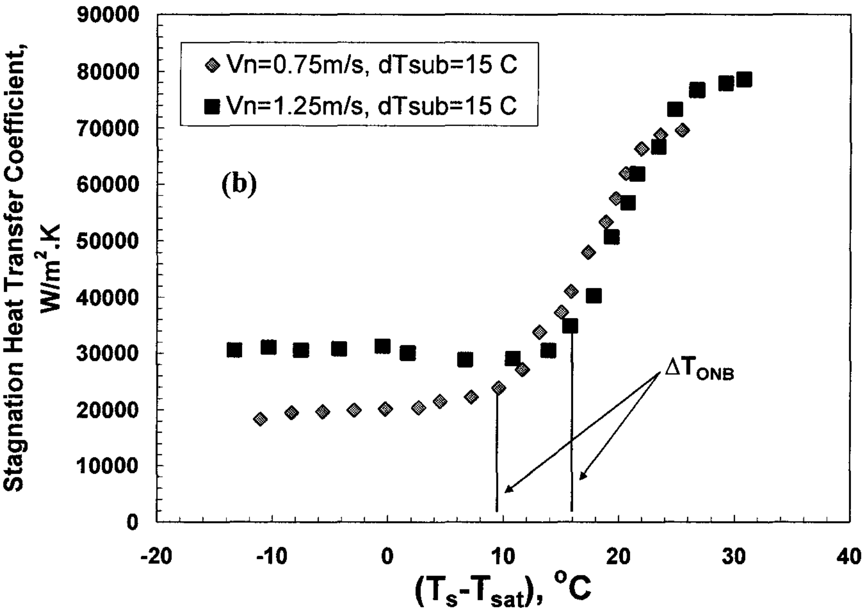

Figure 3. 7 Effect of jet velocity on: (a) Stagnation heat flux, and (b) Stagnation heat transfer coefficient.

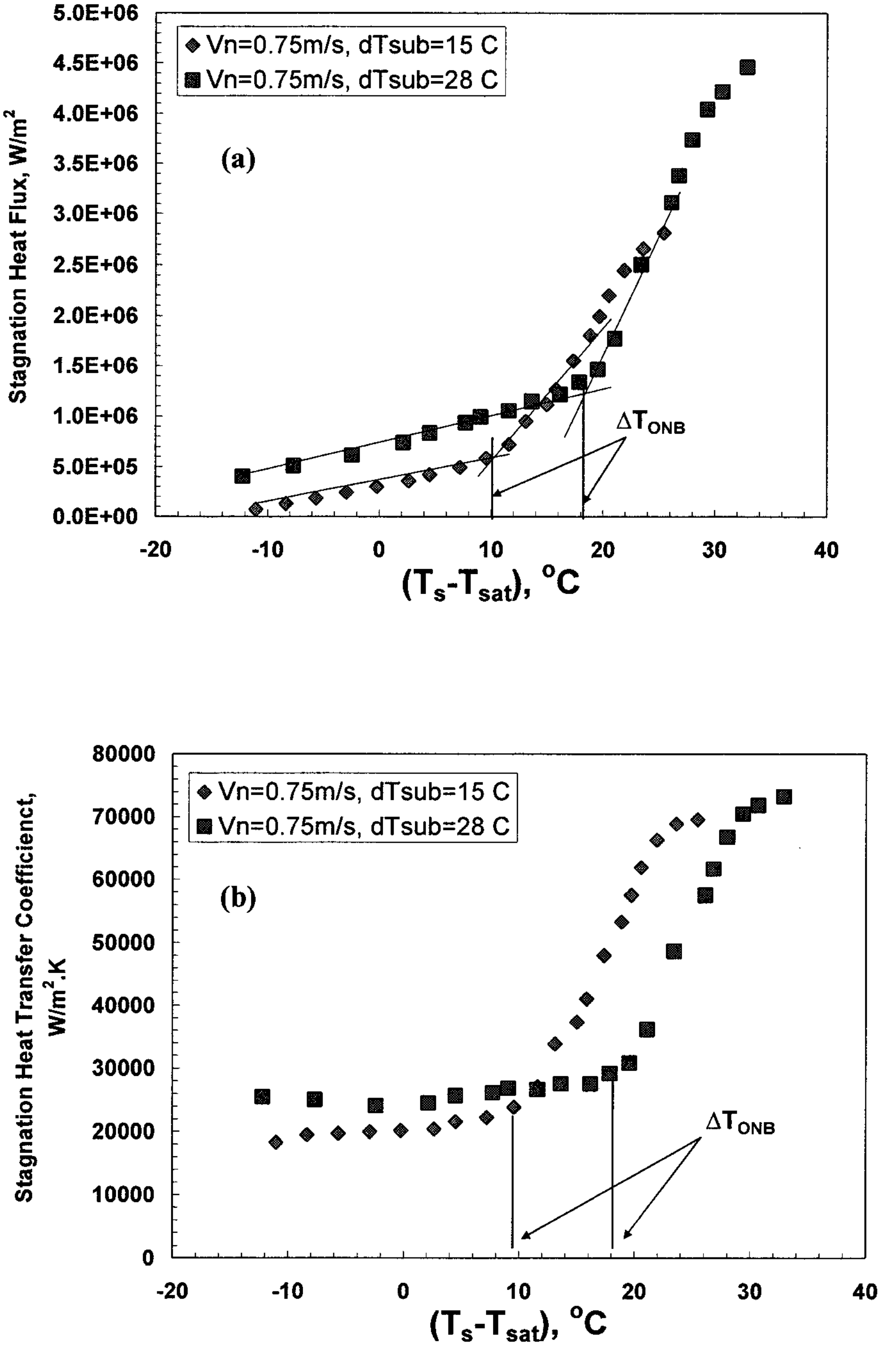

Figure 3. 8 Effect of liquid subcooling on: (a) Stagnation heat flux, and (b) Stagnation heat transfer coefficient.

3.4.2 Variations of Local Boiling Curves

Figure 3.9 shows boiling curves at various locations, *x/w,* along the heated surface. The degree of change of the local boiling curve slopes were found to depend on the location. The farther the location from jet stagnation, the less the slope change becomes and the wider the range of superheat it takes to reach fully developed slope. At stagnation, the change in boiling curve slope could be approximated to a single steep change from single phase to nucleate boiling as there is no distinction at stagnation between partial boiling and fully developed boiling. Boiling curves at downstream locations (in Figure 3.9, at x/w=4 and x/w=8) have more gradual slope changes from single phase to partial boiling and from partial boiling to fully developed nucleate boiling regimes. The farther the location from stagnation the more pronounced the three regions are and the wider the range over which partial nucleate boiling exists as shown in Figure 3.9 where partial boiling extends over superheat range of 7 °C at x/w=4 and over 11 °C at x/w=8). These observations of boiling curve shapes and slope changes is consistent with previous observations reported by Wolf et al. (1996) where it has been proposed that the stagnation boiling curve is characterized with only one steep change in the slope due to simultaneous activation of multiple nucleation sites as boiling onset is delayed to relatively elevated superheat.

Another aspect to be discussed here is the distribution of the wall superheat with the flow conditions and the applied heat flux. As shown in Figure 3.10, the wall superheat is always increasing with the distance from the stagnation. Since for a target average surface superheat the input heat flux varies with the jet velocity and subcooling, the difference between the wall superheat at x/w=10 and that at the stagnation varies between 5 and 8 °C. This variation could affect the timing at which the onset of boiling is observed at various locations on the heated surface and hence affect the determination of the boiling onset superheat. It is to be emphasized that boiling would usually start at downstream locations before stagnation. However, the associated values of boiling onset superheat at the downstream locations could be less or higher than of the stagnation depending on the range of the local wall temperature distribution.

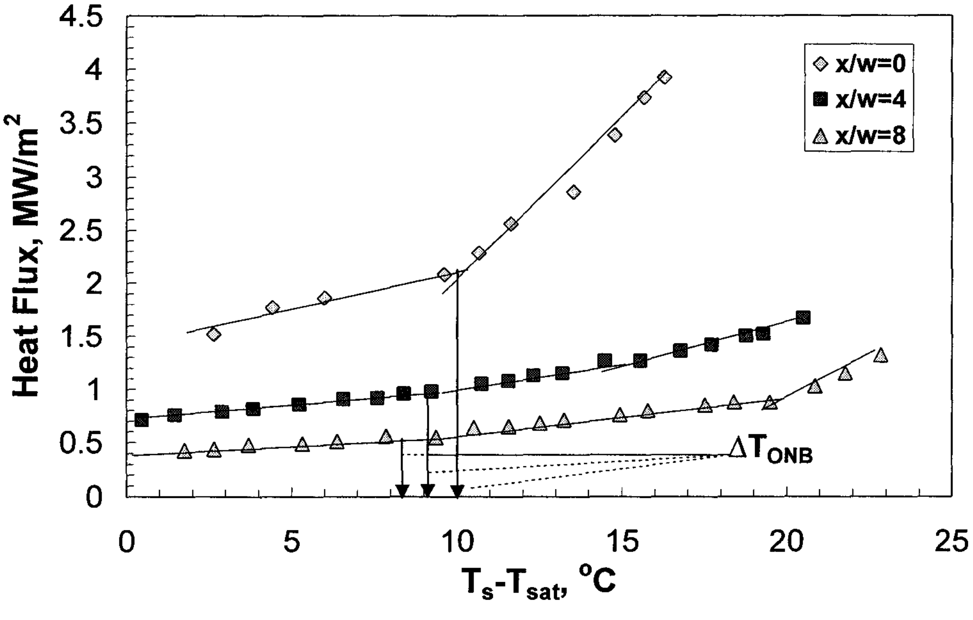

Figure 3. 9 Local boiling curves, $V_n = 0.95$ m/s and $\Delta T_{sub} = 22$ °C.

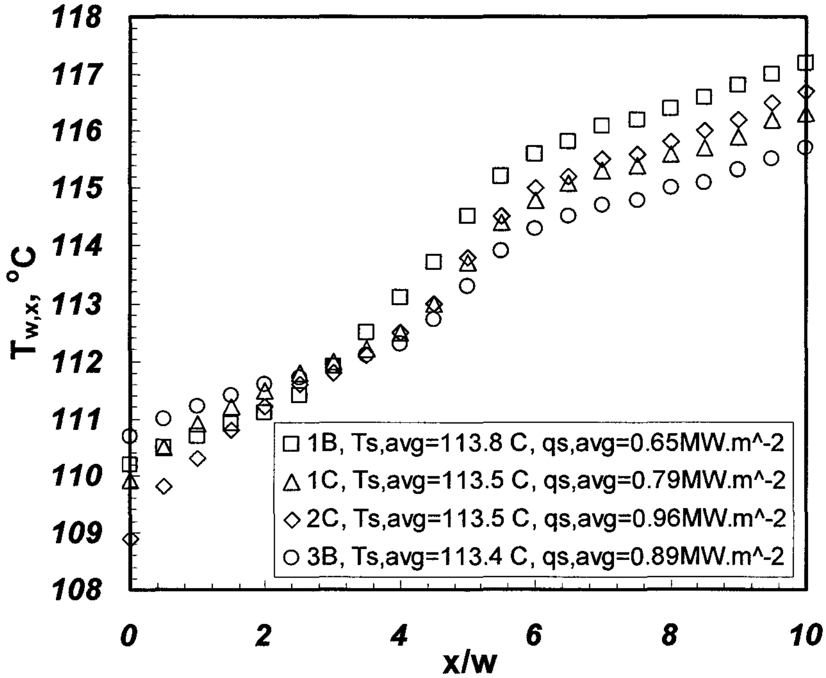

Figure 3. 10 Effect of surface heat flux on the spatial distribution of the heated surface temperature. (1: V_n=0.75m/s, 2:V_n=0.95m/s, 3:V_n=1.25m/s, B:ΔT_{sub}=15 °C, C: ΔT_{sub}=22 °C)

3.4.3 Onset of Nucleate Boiling

Table 3.2 presents the observed values of the wall superheat associated with the onset of nucleate boiling as determined from the changes of the boiling curve slopes as discussed above. This value of surface superheat is thought to be in direct proportion with the jet velocity and liquid subcooling as both parameters suppress the onset of nucleation due to the delay in the provision of suitable environment and limited liquid superheat in the vicinity of the nucleation sites. With the growth of thermal boundary layer, it is also expected that boiling onset will occur at relatively lower surface temperatures. Similar trend of the onset boiling superheat with the distance has been reported by Robidou et al. (2003). However, even with repeating 20% of the experiments, the observed trends of the boiling onset superheat with the jet velocity subcooling or the location were not in well agreement with the expected trends, as can be concluded from Table 3.2. Based on the aforementioned observations and assumptions, Equation (3.9) has been developed to predict ΔT_{ONB} and was in overall agreement with the experimental values within ±40%.

The scatter in the observed boiling onset superheat which has limited the success in predicting the postulated trends of ΔT_{ONB} with the various jet parameters is basically attributed to the effect of non-condensable gases in the water that could have remained even after degassing. The observed changes in the boiling curve slopes which have been used to identify the value of ΔT_{ONB} are sensitive to the intensity of bubble activity in terms of the number of active sites and the attainable bubble size. Those parameters determine the extent of interruption to the bulk flow and hence the additional improvement to the heat transfer rate. The bubble activity is highly sensitive to the flow velocity and local subcooling which affect the heat transfer coefficient and the bubble growth rates. The observed peaks in the single phase heat transfer coefficient at downstream locations could have thus an impact on the observed delays in bubble activity role and that accordingly limited the success to predict the delay in the boiling onset at those locations using Equation (3.9). So, Equation (3.9) should be considered as an initial attempt in the context of modeling of the details of boiling onset under free jet impingement configuration in the vicinity of the jet stagnation with constant mass flow rate. It should be noticed that that as the jet velocity increases the ratio between the mean film velocity U_l to the jet velocity V_n also increases. On the other hand, as the jet velocity is decreased the local liquid film velocity decreases accordingly such that in some cases U_l/V_n would be around 0.1 due to the formation of the hydraulic jump and the associated buildup of the film thickness. Thus, the use of the ratio U_l/V_n does not contradict the hypothesis that the ΔT_{ONB} is in direct proportion with the jet velocity. Rather it accounts for the effect of flow deceleration due to the formation of hydraulic jumps in free jet impingement configuration.

$$\Delta T_{ONB} = 10 \cdot \left(\frac{U_l}{V_n}\right)^{0.15} \cdot Ja_{sub}^{0.05} \cdot e^{(-0.014\frac{x}{w})} \tag{3.9}$$

Table 3. 2 Experimental boiling onset superheat.

$V_{n,\ m/s}$	ΔT_{sub}, °C	x/w	ΔT_{ONB}, °C
0.75	28	0	18
0.75	15	0	9
0.95	22	0	10
0.95	10	0	12
1.25	22	0	13.5
1.25	10	0	12
1.25	22	2	18
1.25	10	2	14

1.7	22	2	17
0.95	22	4	9
0.95	10	4	11
1.25	10	4	16
1.7	22	4	11
0.75	15	6	10
0.75	28	6	11
0.95	22	6	17
0.95	10	6	15
1.25	22	6	17
1.25	10	6	15
1.7	22	6	12.5
0.75	28	8	10
0.75	15	8	17
0.95	10	8	16
0.95	22	8	8
1.25	10	8	17
1.25	22	8	18
1.7	22	8	18.5
0.75	15	10	14
0.75	28	10	18
0.95	22	10	20
0.95	10	10	16.5
1.25	22	10	14
1.25	10	10	15.5
1.7	22	10	15

3.5 Non-Intrusive Measurements of JIB Bubble Dynamics

Non-intrusive observations using high speed camera have been carried out to study the variation of bubble diameter, bubble population intensity and bubble growth termination scenario under various jet impingement cooling conditions.

As a first step, the image processing procedure described in chapter 2 was applied to stacks of approximately 250 successive frames for each cooling condition. Then, statistical analysis of the bubble diameters and number of bubbles detected in the stack frames was carried out. Histograms have been generated for each case to determine the most probable value of the bubble dynamic parameters corresponding to given jet velocity, degree of subcooling and surface superheat. In the following subsections, a description is presented of the development of the empirical sub-models of the bubble dynamics parameters based on these non-intrusive measurements.

3.5.1 Bubble Diameter

The value of the most probable bubble diameter was obtained from the distribution of individual bubble diameter values obtained from the visual observations. Figure 3.11 shows the probability of occurrence of bubble diameter values in between arbitrarily specified bin values over the expected range of bubble diameter. Zero probability of a bin value means there was no bubble diameters observed less than or equal to this value. The same applies to the analysis of the bubble population probability shown in the following section. The bubble diameter was found to increase proportionally with the wall superheat and inversely with liquid subcooling and jet velocity.

As the wall superheat increases, the available energy in the superheated liquid layer increases which promotes bubble growth to larger diameters. Bubbles start to lose heat to the liquid bulk as they protrude into the subcooled liquid. An increase in the jet velocity increases condensation losses from the bubble to the subcooled liquid. In addition, bubble sizes are limited as jet velocity increases due to the reduction in the momentum boundary layer thickness.

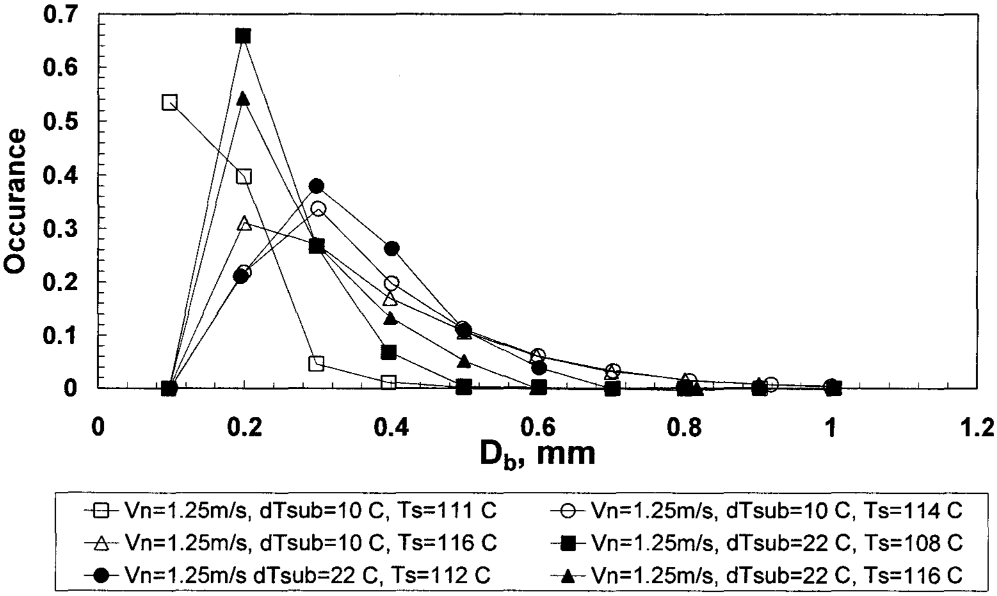

Figure 3. 11 Probability distribution of bubble diameter. at ΔT_{sub}=10 °C and 22 °C, and V_n=1.25 m/s.

Equation (3.10) has been developed using the experimental data of the representing bubble diameter, D_b, which is the diameter value with the maximum probability of occurrence in the visual observations samples, This empirical sub-model has been developed using non-linear regression analysis including all three inputs that characterize the JIB process, i.e., jet velocity in terms of Reynolds number, (Re_w=

$\rho_f V_n w/\mu_f$), wall superheat in terms of superheat Jacob number , ($Ja_{sup}=\rho_f.c_p\Delta T_{sup}/\rho_v h_{fg}$) temperature, Ja_{sup}, and the subcooling Jacob number, ($Ja_{sub}=\rho_f.c_p\Delta T_{sub}/\rho_v h_{fg}$).

$$\begin{aligned} D_b &= 2.3136 - 0.00261 \cdot \mathrm{Re}_w + 3.6896 \times 10^{-7} \cdot \mathrm{Re}_w^2 - 0.01055 \cdot Ja_{sub} \\ &+ 9.95 \times 10^{-5} \cdot Ja_{sub}^2 + 0.127 \cdot Ja_{\mathrm{sup}} - 0.00146 \cdot Ja_{\mathrm{sup}}^2 \end{aligned} \tag{3.10}$$

A comparison between the values of D_b obtained experimentally and those obtained using Equation (3.10) and using previous correlations such as those proposed by Unal et al. (1976) and by Basu (2003) is illustrated in Figure 3.12. Equation (3.10) proved to be more appropriate in predicting the bubble diameter under JIB conditions than the previous correlations. It is to be emphasized that as Equation (3.10) has been developed using experimental data over specific ranges of wall superheat, liquid subcooling and jet velocity, it cannot be used with the same confidence at lower or higher ranges of those parameters neither does it give accurate predictions at very low wall superheat or subcooling (e.g., at zero wall superheat the predicted bubble diameter would not be zero which is obviously not physically expected). It is worth noting here that the other correlations proposed in previous researches have been developed for different boiling conditions and/ or configuration.

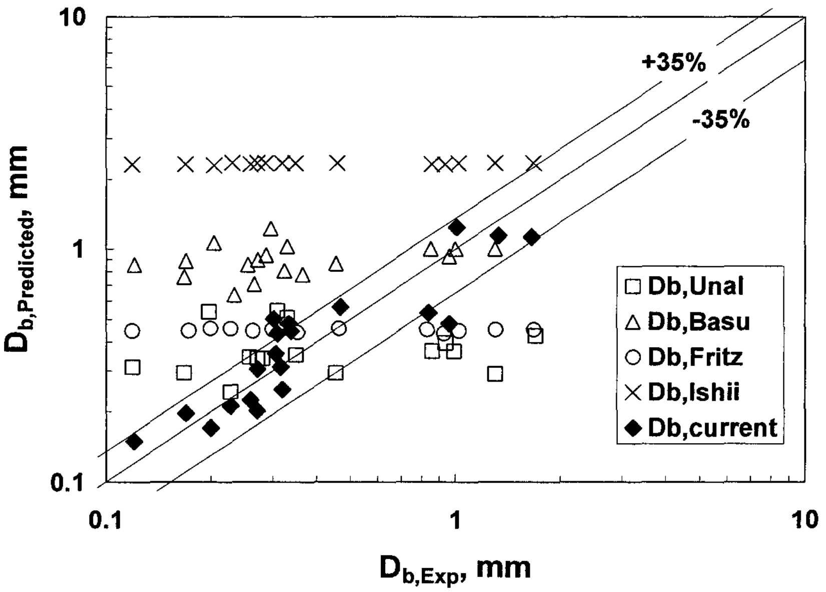

Figure 3. 12 Prediction of the most probable bubble diameter.

For example, the bubble diameter correlation in Unal (1976) has been developed for low velocity, high pressure water flow in horizontal pipe. Basu (2003) has developed her correlation for vertical water flow in square duct, whereas Fritz correlation was developed for pool boiling configuration according to Narumanchi et al. (2008). Equation (3.10) represents a first attempt to predict the bubble diameter using experimental data that was originally obtained under horizontal JIB configuration.

3.5.2 Bubble Population Intensity

The bubble population intensity, N”, is defined as the number of bubbles per unit area of the heated surface. N” has been determined from visual observations within the area of focus of the high speed camera as described in chapter 2. Figure 3.13 shows probability of occurrence of bubble population intensity captured for six experiments (conditions of which are represented in the Figure legend. where the surface temperature T_s is the average heated surface temperature). Only few distant active nucleation sites, and hence few bubbles, were observed within the area of focus in the partial boiling regime. As the wall superheat was increased, the number of active sites increased and site spacing decreased. Increasing the wall superheat further resulted in increasing bubbles diameters.

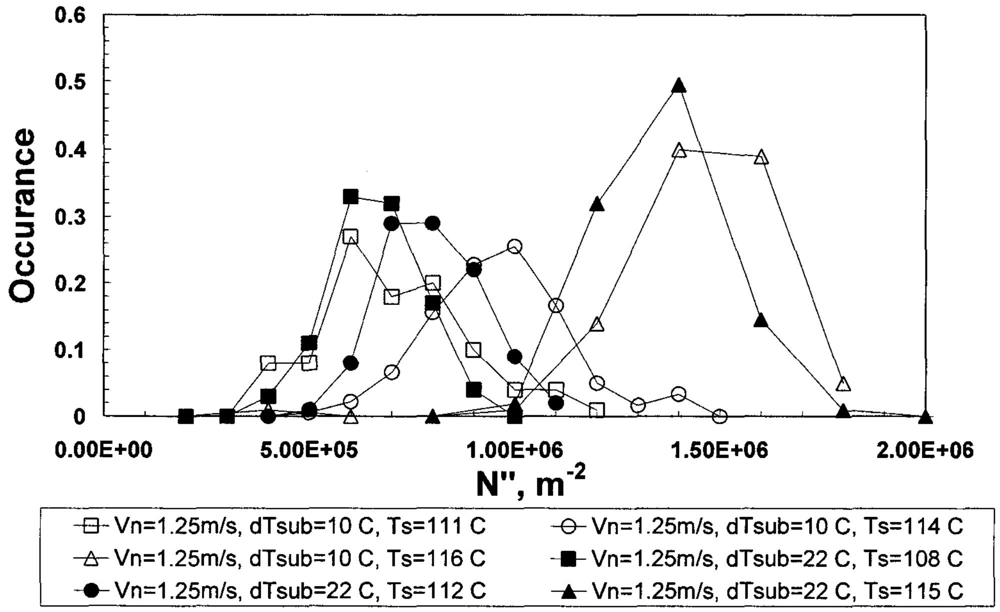

Figure 3. 13 Sample probability distributions of the bubble population.

Accordingly, bubbles started to merge vigorously, which made the detection of individual bubbles before merging extremely difficult. The proposed models of both bubble diameter and population (i.e., Equations (3.10) and (3.11)) have been developed using experimental data that was obtained over range of surface superheat ΔT_{sup}=8 and 20 °C where appropriate level clarity of the flow field was available to measure the size and count the number of bubbles on the heated surface.

N” has been correlated as function of the jet velocity in terms of Reynolds number and both degree of subcooling and degree of superheat in terms of Ja_{sub} and Ja_{sup}; respectively. Equation (3.11) provides the correlation of N” under the current JIB conditions.

$$\begin{aligned} N'' = -1.04786\times10^{7} + 2339\cdot \mathrm{Re}_w - 0.4306\cdot \mathrm{Re}_w^2 + 260409\cdot Ja_{sub} \\ - 2520\cdot Ja_{sub}^2 + 52291\cdot Ja_{\mathrm{sup}} + 276.2\cdot Ja_{\mathrm{sup}}^2 \end{aligned} \tag{3.11}$$

The prediction of Equation (3.11) is demonstrated in Figure 3.14 along with predictions using correlations from existing literature for PFB conditions developed by Chwala (1999) and Basu (2003), which was reported by Narumanchi et al. (2008).

Although the wide scatter in the obtained experimental data, even with the repetition of experimental runs resulted in some predictions being over twofold of the experimental values, there is still a noticeable improvement in the prediction of bubble population using Equation (3.11) as compared to predictions of previous correlations and the majority of the predictions were yet within ±50% of the experimental data. This scatter in the experimental data is again attributed to the interference from non-condensable gases which could have possibly contributed to the number of amount of bubbles appearing within the focus area during the conduct of visual observations. It is concluded here that for better agreement in future studies, online degassing should be applied even though distilled or highly purified water is used to eliminate entrapment of air along the flow path during the conduct of free jet impingement cooling experiments. Another improvement to the conduct of this type of experiment could be to provide a means of isolation around the jet impingement assembly from the room environment to control of air content around the boiling surface.

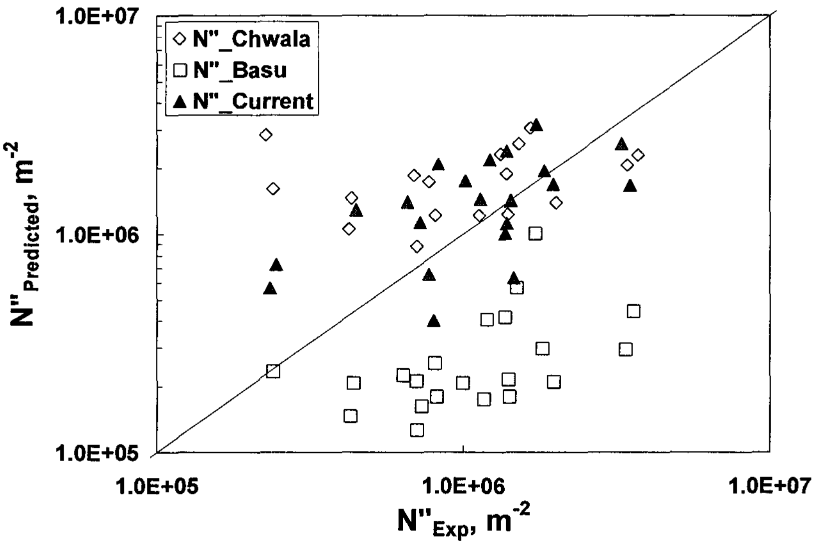

Figure 3. 14 Prediction of the proposed sub-model of the bubble population.

Table 3.3 lists the JIB conditions at which the experimental results have been used to develop the bubble diameter and population density sub models. Further information on the ranges of parameters over which the experimental data was obtained is provided in Table 3.3. The bounds of applicability of the proposed Equations (3.10 and 3.11) would hence be: 1500 to 4500 for Re_w, 25 to 70 for Ja_{sub}, and 35 to 60 for Ja_{sup}.

Table 3. 3 Experimental vs. predicted bubble diameter and population intensity.

Re_w	Ja_{sub}	Ja_{sup}	$D_{b,Exp}$, mm	$D_{b,predicted}$, mm	N''_{Exp}, m^{-2}	$N''_{predicted}$, m^{-2}
1886	56.97	51	1.65	1.11	1.35E+06	2.44E+06
1913	56.93	59.9	0.29	0.76	1.70E+06	3.20E+06
2438	66.06	39	0.17	0.61	1.44E+06	1.33E+06
2463	66.03	45	0.28	0.62	1.00E+06	1.79E+06
2510	66.05	40.5	0.46	0.58	6.50E+05	1.46E+06
2554	66	51	0.94	0.47	1.20E+06	2.28E+06
2563	44.94	47.9	0.29	0.51	3.36E+06	2.44E+06
2584	50.98	42.9	0.84	0.52	8.00E+05	2.16E+06
2613	29.94	44.9	0.33	0.55	1.69E+06	1.13E+06
3073	66.07	36	0.17	0.2	1.40E+06	1.09E+06
3136	66.02	48	0.26	0.23	1.80E+06	1.97E+06
3183	44.98	36	0.12	0.15	1.12E+06	1.46E+06
3199	44.97	39	0.27	0.2	1.98E+06	1.67E+06
3293	29.94	41.9	0.32	0.25	2.40E+05	7.68E+05
3341	29.93	50.9	0.2	0.17	1.40E+06	1.44E+06
4043	66.07	36	0.23	0.21	7.98E+05	3.84E+05
4105	66.03	45	0.27	0.32	1.40E+06	9.85E+05
4292	44.94	50.9	0.32	0.32	3.60E+06	1.62E+06
4416	29.92	53.9	0.3	0.36	1.50E+06	6.03E+05

3.5.3 Bubble Growth Termination (BGT) Scenario

High speed imaging has also been used to investigate the effect of surface and jet conditions on the process of bubble growth and bubble growth termination (BGT) scenario. A sample of the sequence of images used to carry out such task is shown in Figure 3.15. The identification of the most probable BGT scenario is important in modeling of JIB heat transfer. Depending on the BGT scenario, different heat transfer mechanisms would take place at various locations of the heated surface area. Two BGT scenarios have been identified and detected in the current study: Local Collapse (LC), and Bubble Departure (BD).

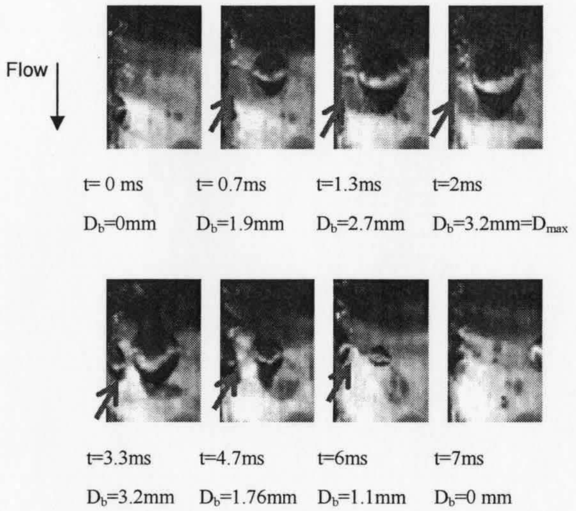

Figure 3. 15 Visual observation of bubble growth and BGT scenario. A case of LC identified for V_n=0.55 m/s, ΔT_{sub} = 15 °C and ΔT_{sup} = 20 °C.

Visual observations of the flow field indicated that no BD occurred downstream of any hydraulic jump. . This could be attributed to the low average flow velocity downstream of the jump. In which case, flow drag would not be strong enough to cause the bubble to move (slide) along the surface or depart from the surface. Therefore, only LC is possible. On the other hand, upstream of the jump where flow velocity is high, bubbles might or might not remain attached to the surface depending on the degree of superheat which controls the rate of bubble growth. In this case, both LC and BD scenarios are possible. In the current study, at jet velocities higher than 1 m/s, bubble sliding was commonly observed as the BGT scenario, whereas at jet velocities lower than 1 m/s, even small bubbles remained attached at their nucleation sites until they locally collapsed. The latter is typical of the situation downstream the hydraulic jump. The bubble sliding distance, L_{slid}, has been measured and found to be in the order of few bubble diameters. Equation (3.11) provides the average value of L_{slid}.

$$L_{slid} = 3D_b \tag{3.12}$$

Equation (3.12) can be only used to determine the sliding distance at upstream locations of a hydraulic jump and for jet velocities higher than 1 m/s. The stagnation region is an exceptional case of the aforementioned sliding criteria as it is postulated here that bubbles generated at the stagnation will locally collapse, regardless of the velocity value.

3.6 Intrusive Measurements of Bubble Dynamics Parameters

3.6.1. Bubble Release Frequency

As discussed in chapter 2, an intrusive optical probe has been used in the current study to measure the bubble release frequency, f at various nucleation sites. In addition, the bubble growth period, t_g was calculated from the contact time between a growing bubble and the probe The values of the bubble release frequency and growth time presented below are the time average values of the measurements at various nucleation sites along the heated surface where the corresponding steady state surface superheat was taken to be the average of the entire heated surface. . The probe locations vary as the nucleation sites were first identified visually and then the probe tip was moved to the active sites to take the measurements. At least 3 different locations were used per each test run to obtain the average frequency and contact period. From the calculation of f and t_g, the waiting time, t_w between a bubble growth termination and the successive bubble growth onset has been determined using Equation (3.13)

$$t_w = \frac{1}{f} - t_g \tag{3.13}$$

An example of how the bubble release frequency was determined is discussed below for the case of $V_n = 0.4$ m/s, $\Delta T_{sub} = 20$ °C, and $\Delta T_{sup,avg} = 20$ °C The first step is to record the frequency values at the various locations (in this example at x/w=0, 3, and 7) under steady state conditions for sufficient period of time, i.e., long enough to capture several cycles of bubble generation. This period was approximately between 5 to 8 seconds. For ease of data handling, the probe signal recording was divided into samples with each sample file containing information about the voltage signal over 100 millisecond as shown in Figure 3.16. A histogram was then generated using 10 bins to investigate the distribution of the frequency values. As shown in Figure 3.17, the frequency values distribution resembles normal distribution and hence the representing value of the bubble release frequency was simply the mean of the frequency values.

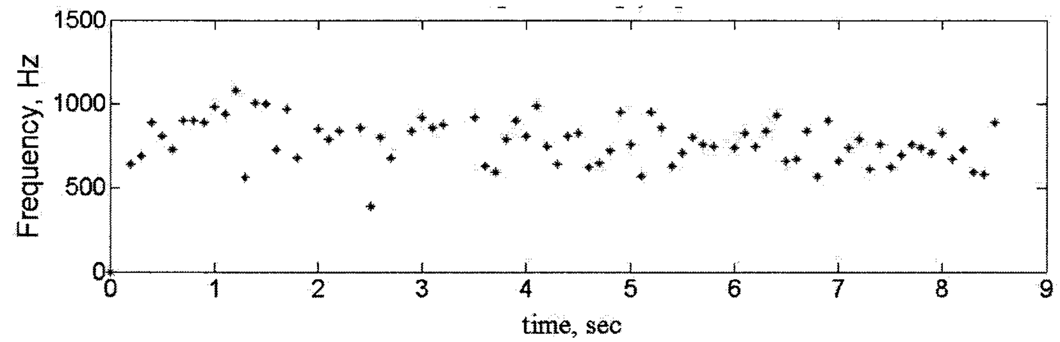

Figure 3. 16 Time history of bubble release frequency at V_n=0.4 m/s, ΔT_{sub}=20 °C, and $\Delta T_{sup,avg}$=20 °C.

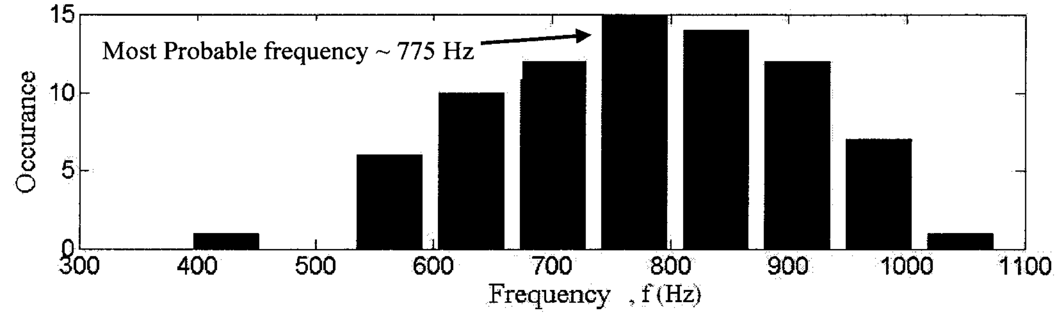

Figure 3. 17 Histogram of bubble release frequency (For the case of Figure 3.16).

Trend analysis of the bubble release frequency with the jet velocity, liquid subcooling and wall superheat has been conducted. An example of the obtained trends is shown in Figure 3.18 where the variation of the bubble release frequency was plotted against the dimensionless wall superheat Ja_{sup} for various Re_w and Ja_{sub} levels.

As shown in Figure 3.18, the bubble release frequency was found to increase with the wall superheat. This is expected since high superheat is a favorable condition for promoting bubble nucleation, and hence it would increase the number of bubbles released. It is worth mentioning here that despite the obtained monotonic increase of the release frequency with the wall superheat as reflected from the shown experimental result, this trend may change at higher wall superheat levels than those at which the results shown have been obtained. This would be attributed to the increase of the maximum attainable bubble diameter and bubble merging on the surface which could result in lower release frequency as sensed by the optical probe due to the elongated bubble retention on the heated surface. However, in the current study such change in the frequency trend with wall superheat could not be confirmed.

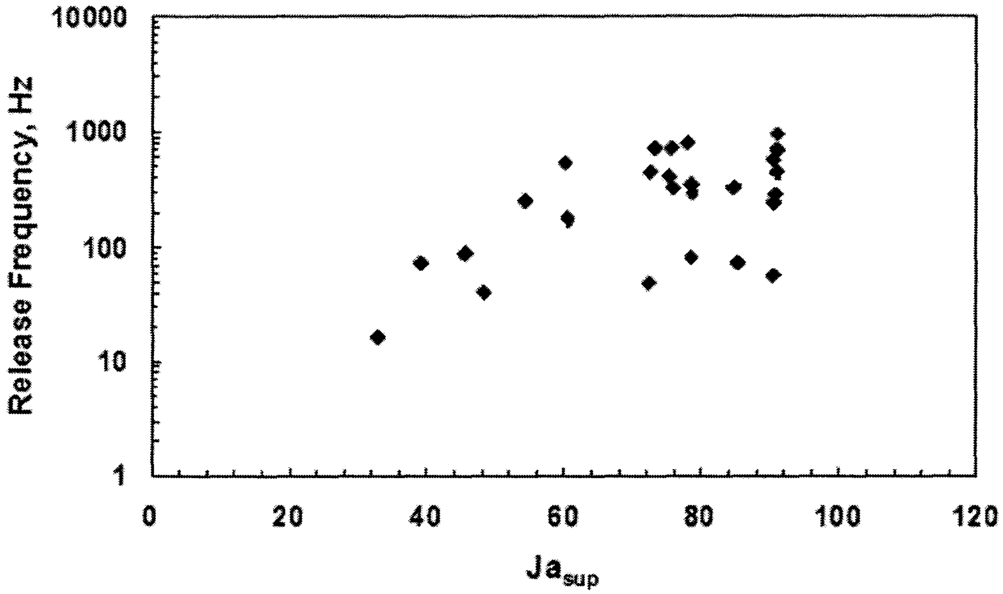

Figure 3. 18 Variation of bubble release frequency with wall superheat

An increase in the degree of subcooling, on the other hand, results in a decrease in the release frequency. It is postulated here that this is primarily due to the increase in the waiting time at higher subcooling due to the increase in the required time for the liquid to attain the appropriate level of superheat for bubble growth onset. In addition, it is postulated here that the bubble growth rate decreases with liquid subcooling due to higher condensation losses to the subcooled fluid bulk, Unal (1976).

Increasing the jet velocity was found to found to adversely affect the bubble release frequency. This can be attributed to the increase in waiting time for succeeding bubble to start growing after a preceding bubble has collapsed or departed from the nucleation site due to an increased possibility of liquid flooding of these site and the increased condensation losses. In addition the thickness of both momentum and thermal boundary layers decreases with the increase in flow velocity. Hence, the available amount of superheat in the vicinity of the heated surface will subsequently be less which demotes the bubble growth onset.

From the above discussion and using the experimental data of the most probable bubble release frequency at various combinations of jet velocity, subcooling, and surface superheat, a correlation given in Equation 3.14 has been developed to model the aforementioned variation of the bubble release frequency as function of the three JIB parameters. The agreement between the proposed submodel and the experimental data is presented in Figure 3.19.

$$f_{predicted} = (5.015 \cdot 10^7) * \frac{Ja_{\text{sup}}^{1.82}}{\text{Re}_w^{1.89}\, Ja_{sub}^{1.69}} \quad \text{Hz} \qquad (3.14)$$

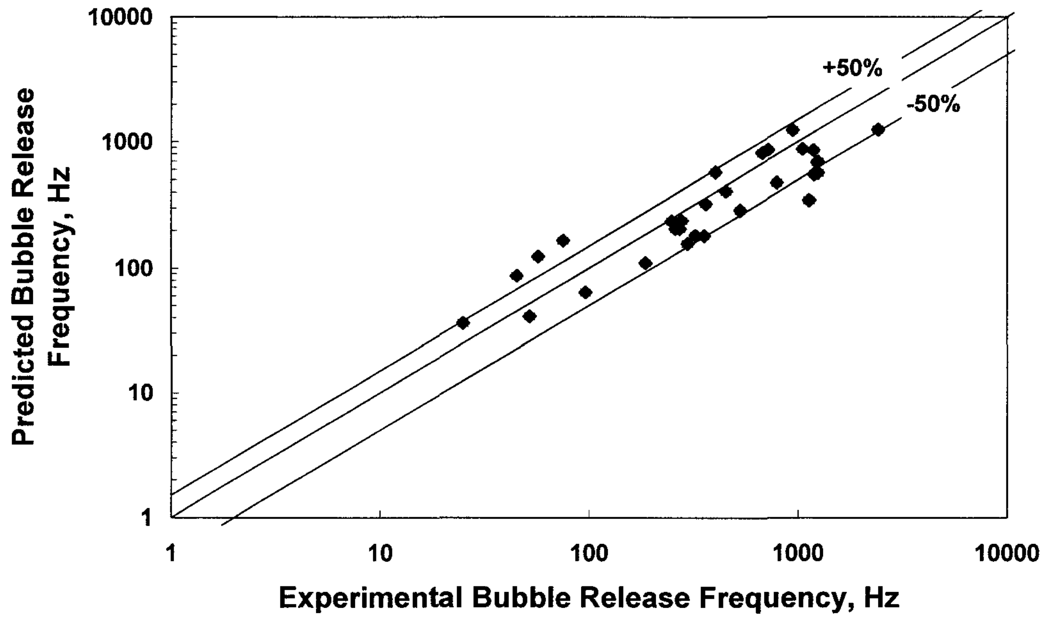

Figure 3. 19 Prediction of bubble release frequency using Equation 3.14

Table 3.4 lists all experimental conditions used to develop the correlation in Equation (3.14) and a comparison between the experimental and predicted frequency values using Equation (3.14). Equation (3.14) has been developed for Re_w range between 540 and 1720, Ja_{sup} range between 33 and 105, and Ja_{sub} range between 30 and 85.

Table 3. 4 Experimental and predicted bubble release frequency

Re_w	Ja_{sub}	Ja_{sup}	f_{exp}, Hz	$f_{predicted}$, Hz
536.83	60.29	90.43	942	1238
542.54	60.31	75.39	719	871
542.54	60.31	75.39	1050	871
545.73	60.33	66.36	1232	682
999.7	45.2	84.38	1193	549
1004.3	45.21	78.37	792	476
1008.8	45.22	72.35	452	408
1013.1	45.23	66.33	1134	345
1017.3	45.24	60.31	529	288
1021.3	45.24	54.29	248	236
1027	84.48	84.48	323	182
1030.7	84.5	78.46	296	157
1244.5	30.12	90.36	674	818
1293.6	30.16	39.21	75	166
1298.5	84.47	87.49	57	124
1309.9	84.51	72.44	45	87
1325.3	84.58	48.33	52	41
1637.5	45.18	105.41	361	324
1658.3	45.2	90.39	277	239
1673.9	45.21	78.37	355	181
1695.5	45.24	60.31	186	110
1711.7	45.26	45.26	96	64
1723.5	45.27	33.2	25	36

3.6.2. Bubble Growth and Waiting Times

The bubble growth has been found to strongly depend on the degree of superheat. This is reflected by the inverse proportion between the average growth time at each level of surface superheat shown in Figure 3.20. At higher superheat, there is an increase in the available heat supply from the superheated liquid layer that promotes bubble growth which results in faster growth to the maximum bubble diameter.

Both the flow velocity and liquid subcooling has adversely affected the bubble growth time. This is attributed to the reduction expected in the maximum attainable bubble diameter with the increase of both parameters. This reduction in the maximum diameter is due to the increase in drag force on the bubble and condensation losses from the bubble to the liquid. The increase in condensation losses in fact can support the role of drag in early eviction of bubbles from the nucleation sites. With the increase in condensation losses, the net heat to the bubble decreases and hence its growth rate is expected to decrease. This reduces the liquid resistance to displacement due to bubble expansion into the liquid bulk. With this liquid resistance tending to retain the bubbles at the nucleation sites, and so acting as resistance to flow drag, reduction in this resistance would result in early bubble eviction. In addition, with the increase in flow velocity, there would be reduction in the thermal boundary layer thickness and consequently in the superheated layer thickness from where the growing bubble receives the heat required for growth continuation.

The increase in liquid subcooling also contributes to the limitation in the available liquid superheat in the vicinity of the heated surface which occupies a portion of the thermal boundary layer that decreases with the increase in liquid subcooling. An overall reduction in average growth time dropped from 0.5 ms at $Re_w \sim 1000$ to below 0.1

ms at Re_w~1700 over a range of wall superheat between Ja_{sup} =33 and 90. It should be emphasized here that this conclusion is limited to the ranges of wall superheat and jet parameters shown in Table 3.5.

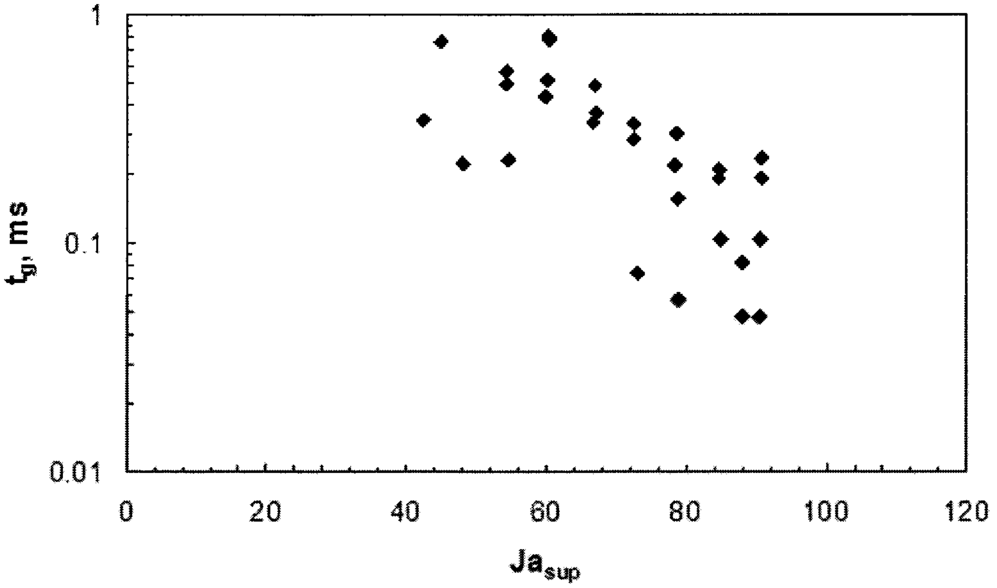

Figure 3. 20 Variation of experimental bubble growth time with surface superheat.

Using the mean growth time determined from the histograms generated for each experiment during which the optical probe was used, a sample is shown in Figure 3.21, the following constitutive submodel of the bubble growth time has been developed:

$$t_{g,predicted} = \frac{0.13 \cdot e^{(-0.002 \cdot \mathrm{Re}_w)}}{Ja_{\mathrm{sup}}^{1.07}} \text{, sec} \tag{3.15}$$

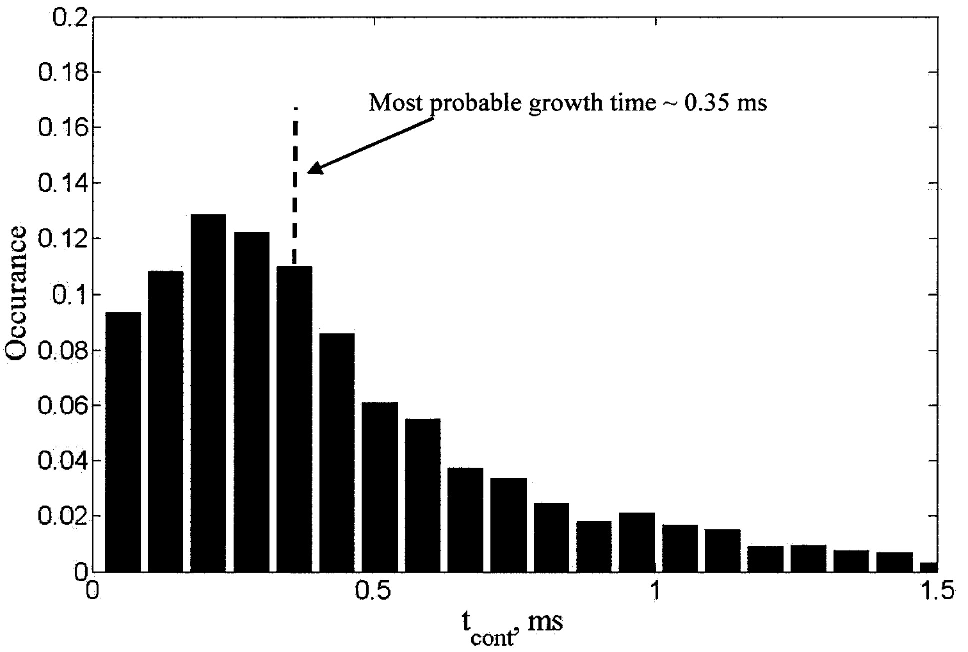

Figure 3. 21 Probability distribution of bubble growth time in the case of V_n=0.4 m/s, ΔT_{sub}=20 °C, and $\Delta T_{sup,avg}$=20 °C.

Equation (3.15) has been developed using data obtained over the same ranges of Re_w, Ja_{sub} and Ja_{sup} of Equation (3.14). The level of model uncertainty of Equation (3.15) is ±40% as shown in Figure 3.22. The waiting time between a bubble growth termination and the onset of the next bubble at the same site can be calculated from Equation (3.12) where the values of f and t_g are those calculated from Equations (3.14) and (3.15), respectively.

The predicted values of both the growth time and wait time under various conditions of jet velocity, degree of subcooling, and surface superheat are presented in Table 3.5.

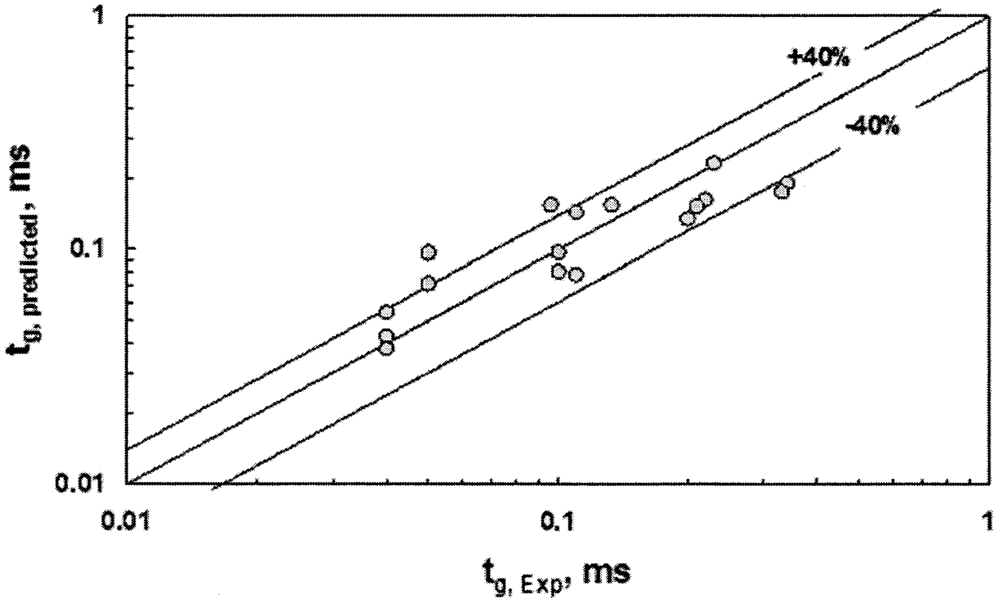

Figure 3. 22 Prediction of the growth time using Equation 3.15

The wait time in various cases is one or two orders of magnitude higher than the growth time. Since the typical JIB heat transfer cycle consists of bubble nucleation, growth and collapse or departure. Such difference in the growth and waiting times reflects the dominance of the effect of liquid contact with the heated surface, which hence indicates that the main mechanisms of heat transport in JIB are those attributed to sensible heating of liquid, rather than to evaporation. This conclusion has been used as a foundation for the development of the JIB heat transfer model discussed in the following chapters.

Table 3. 5 Predictions of bubble growth and waiting periods

Re_w	Ja_{sub}	Ja_{sup}	$t_{g,exp}$, ms	$t_{g,predicted}$, ms	$t_{w,model}$, *ms*
999.7	45.2	84.38	0.21	0.15	1.57
1004.31	45.21	78.37	0.22	0.16	1.83
1008.77	45.22	72.35	0.33	0.18	2.15
1013.09	45.23	66.33	0.34	0.19	2.56
1017.27	45.24	60.31	0.8	0.21	3.08
1021.29	45.24	54.29	0.23	0.23	3.79
1023.24	84.46	90.5	0.2	0.14	4.44
1027.03	84.48	84.48	0.11	0.14	5.08
1030.66	84.5	78.46	0.13	0.16	5.86
1296.11	84.46	90.5	0.11	0.08	7.07
1298.53	84.47	87.49	0.1	0.08	7.55
1309.88	84.51	72.44	0.05	0.1	10.85
1325.28	84.58	48.33	0.06	0.14	23.26
1658.26	45.2	90.39	0.04	0.04	3.93
1673.85	45.21	78.37	0.04	0.04	5.19
1695.45	45.24	60.31	0.04	0.05	8.6
1711.71	45.26	45.26	0.05	0.07	14.8
1723.53	45.27	33.2	0.1	0.1	26.39

Chapter 4

GLOBAL MODELING OF JIB

4.1 Introduction

Development of a global, hybrid analytical/empirical model of JIB heat transfer is presented in this chapter based on the concept of bubble-induced diffusivity (BID). The BID model has been developed to predict nucleate JIB heat transfer rate at jet stagnation where the main difference between PFB and JIB flow domains exists.

Numerical modeling of JIB involves two major tasks: (1) simulating phase change due to boiling and account for its effect on flow hydrodynamics, and (2) resolving the interface between the liquid and the surrounding gas (air). Carrying pout task (1) involves dealing with the time and length scales of bubble dynamics, which are in the order of 10^{-5}-10^{-4} s and 10^{-4}-10^{-3} m, respectively. The global BID model described herein is an attempt to provide a simplified means to carry out such task. The model accounts for the effect of bubble generation on the mean flow hydrodynamics and on the wall heat flux without the need to model or resolve the details of phase change The BID concept introduces an additional diffusivity to the molecular one in the diffusion terms of the momentum and energy conservation Equations. By using this approach, only the task of resolving the free surface would be required in the simulations, which would significantly reduce the complexity and cost of computations.

The basis of the derivation and development of the BID model is similar to that developed in a previous study for single-phase impingement heat transfer by Zumbrunnen (1991) and in a study of film boiling impingement heat transfer by Timm et al. (2003), in which case they attained film boiling by maintaining a very high surface to saturation temperature ratio ($5 < T_s/T_{sat} < 8$). In the current study, the implementation of this approach has been carried out to investigate the applicability of the BID concept for nucleate boiling using a much lower ratio, $1< T_s/T_{sat} < 2$, The solution of the analytical BID model is based on converting the partial differential conservation Equations of momentum and energy into ordinary differential Equations (ODE) using a set of dimensionless stream and temperature functions In addition, the closure of the analytical model has been achieved by developing an empirical correlation of the additional diffusivity using the experimental data discussed in chapter 3. It is worth noting that previous studies who have adopted the BID concept did not provide any constitutive models of the additional diffusivity. Add reference to the paper. The proposed BID model has been published recently in Omar et al. (2009).

4.2 The Physical Basis of the BID Concept

Figure 4.1is a schematic of the velocity field of a planar free jet impinging on a flat surface. As the jet impinges on the heated surface, it diverts symmetrically about the stagnation point (line) and flows parallel to the surface. When the surface temperature is well above the saturation temperature of the liquid, bubbles start to nucleate and grow on the surface. The adjacent region to the surface where bubbles nucleate is referred to as the "bubbly layer" (BL). The thickness of the BL is assumed equal to the bubble diameter, as shown in Figure 4.2. Due to the cyclic bubble growth and decay, additional disturbances are induced into the main flow. Such disturbances improve the heat transfer from the surface to the fluid bulk. For nucleation to take place within the BL, there should be enough liquid superheat around each bubbles in order to sustain its growth, Hsu (1962) and Carey (1992).

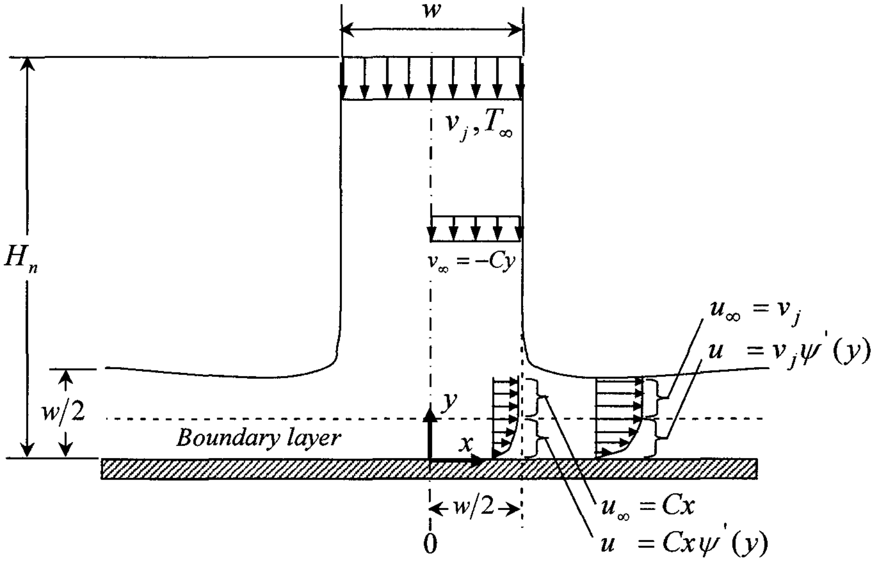

Figure 4. 1 Velocity field of a free jet impinging on a flat surface.

Thus, it has been assumed in this study that the liquid in the BL is superheated and that the top of the BL is at the saturation temperature. The top of the BL is taken as the bottom boundary of the computational domain shown in Figure 4.2. The intensity of flow disturbances due to bubble generation on the heated surface is assumed to have a maximum value at this bottom boundary.

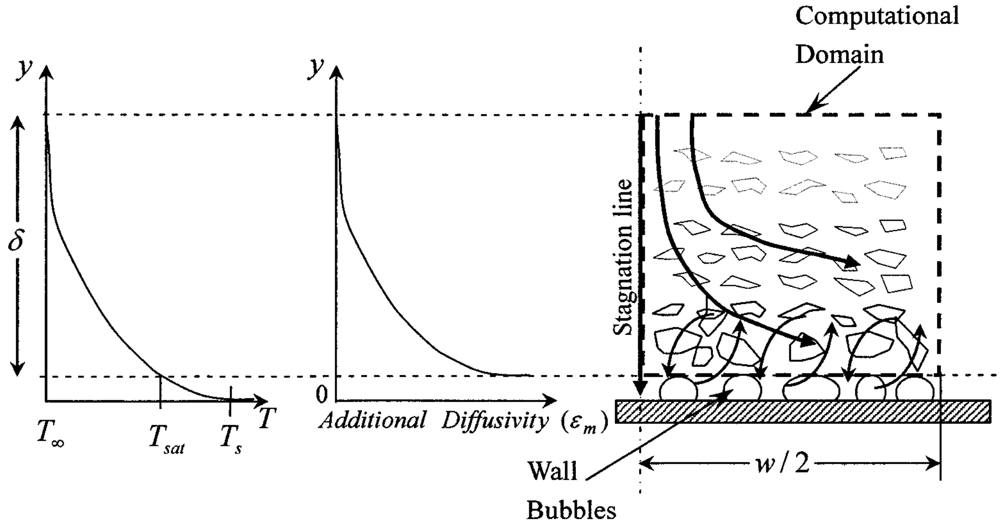

Figure 4. 2 JIB flow and temperature fields in the jet stagnation region.

The influence of the bubble-induced disturbances decays in the vertical direction from the top of the BL. The transport enhancement that results from such disturbances is represented by additional diffusion of momentum and energy that originates at the domain bottom boundary. In addition to the molecular diffusivities in the diffusion terms of the conservation Equations, additional diffusivities have been added such that they account for bubble-induced diffusion in the momentum and energy transport. Such diffusivities are not constant and should rather decay as well in the vertical direction, as shown in Figure 4.2.

With that spatial variation in the normal direction and being dependent on the flow velocity and temperature, the additional diffusivities are thus flow properties, not fluid properties. The modified momentum and energy Equations are to be solved within the computational domain of interest in order to obtain the velocity and temperature fields with consideration of the effect of the BID.

4.3 Modeling Assumptions

In the development of the BID global model of stagnation JIB heat transfer, the following assumptions have been employed:

1. Liquid properties are constant.
2. Flow is incompressible and steady.
3. Surface temperature in the stagnation region is constant. This assumption is valid, given the size of the stagnation region considered in this study.
4. The additional diffusivities in the momentum and energy Equations are equal, i.e., the bubble-induced diffusion Prandtl number, $Pr_t = \varepsilon_m/\varepsilon_t$ is assumed = 1.
5. The additional diffusivities are decaying functions in the vertical direction.

6. The temperature at the bottom of the computational domain is equal to T_{sat}.
7. The amount of direct heat transfer from the heated surface due to evaporation is negligible.
8. The boundary layer thickness in the stagnation region is constant because of the balance between the flow acceleration and the viscous effect, White (1991).

4.4 Mathematical Formulation

4.4.1 Analytical BID model of nucleate JIB heat transfer at stagnation

The boundary layer flow problem depicted in Figure 4.2 can be mathematically represented by the following set of boundary layer Equations:

1- The Continuity Equation:

$$\frac{\partial u}{\partial x}+\frac{\partial v}{\partial y}=0 \tag{4.1}$$

2- The Momentum Equation:

$$u\frac{\partial u}{\partial x}+v\frac{\partial u}{\partial y}=-\frac{1}{\rho_l}\frac{dP}{dx}+\frac{\partial}{\partial y}\left[(\varepsilon_m+\nu)\frac{\partial u}{\partial y}\right] \tag{4.2}$$

3- The Energy Equation:

$$u\frac{\partial T}{\partial x}+v\frac{\partial T}{\partial y}=\frac{\partial}{\partial y}\left[(\varepsilon_t+\alpha)\frac{\partial T}{\partial y}\right] \tag{4.3}$$

The total diffusivity, ε, in Equations (4.2) and (4.3) equals to the sum of the additional diffusivities ε_m or ε_t due to bubble-induced diffusion, and the molecular diffusivity. This sum has a maximum value at the bottom boundary of the computational domain, ε_{max}. The ratio between the maximum total diffusivity and the molecular diffusivity is defined as the dimensionless total, or *effective*, diffusivity, ε^+.

The velocity components, u and v in the x- and y-directions, respectively can be defined in terms of a stream function *ψ(y)* in the stagnation region such that:

$$u = C\,x\,\psi'(y) \tag{4.4}$$

$$v = -C\,\psi(y) \tag{4.5}$$

The velocity gradient C can be expressed in terms of jet velocity, v_j, and jet width, *w*, such that $C = \bar{C} v_j / w$, where the value of $\bar{C} \sim 1.0$, Zumbrunnen et al., (1991) and Timm et al. (2003). The pressure distribution in the outer region of the flow is given by Bernoulli's Equation as:

$$P_o - P = \frac{1}{2}\rho_l C^2 [x^2 + F(y)] \tag{4.6}$$

Where, P_o is the stagnation pressure. It should be noticed that only the pressure gradient in parallel direction to the surface; i.e., $\partial P/\partial x$ is needed for solving the conservation Equations. Therefore, the evaluation of the function *F(y)* is not necessary in this context. Combining Equations (4.4), (4.5), and (4.6) together with the definition of ε, the momentum and the energy Equations can be written as:

$$\frac{\varepsilon}{C}\psi''' + \left(\frac{\varepsilon'}{C} + \psi\right)\psi'' - (\psi')^2 + 1 = 0 \tag{4.7}$$

$$\frac{\varepsilon}{C}\frac{\partial^2 T}{\partial y^2}+\left(\Pr_t \psi+\frac{\varepsilon^{'}}{C}\right)\frac{\partial T}{\partial y}=0 \tag{4.8}$$

According to assumption number (4), the bubble-induced diffusion Prandtl number, $\Pr_t = \varepsilon_m/\varepsilon_t$ is assumed = 1. Introducing a set of dimensionless variables for the coordinates x and y, stream function $\psi(y)$, velocity components u and v, and fluid temperature T yields:

$$\bar{x}=\frac{x}{w},\eta=y\sqrt{\frac{C}{\varepsilon_{\max}}},\ \bar{u}=\frac{u}{v_j},\ \bar{v}=\frac{v}{v_j},\Psi=\psi\sqrt{\frac{C}{\varepsilon_{\max}}},\theta=\frac{T-T_\infty}{T_{sat}-T_\infty} \tag{4.9}$$

Equations (4.7) and (4.8) can be written in dimensionless form as:

$$N\Psi'''+N'\Psi''+\Psi\Psi''-(\Psi')^2+1=0 \tag{4.10}$$

$$N\theta''+(\Pr_t\Psi+N')\theta'=0 \tag{4.11}$$

Where N is defined as $N(\eta) = \varepsilon/\varepsilon_{\max}$. This function should satisfy the hypothesis of decaying total diffusivity with the vertical distance. The exponential decay of $N(\eta)$ has been assumed similar to Zumbrunnen (1991) and Timm et al. (2003) such that:

$$N=\frac{\varepsilon}{\varepsilon_{\max}}=\exp(-c_\varepsilon\eta)+\frac{1}{\varepsilon^+} \tag{4.12}$$

Where c_ε has been assumed ≈ 2 by Zumbrunnen (1991). The boundary conditions for Equations (4.10) and (4.11) are:

$$\eta=0:\ \Psi=\Psi'=0,\ \theta=1, N=1 \tag{4.13}$$

$$\eta \to \infty : \Psi' \to 1, \ \ \theta, N \to 0 \tag{4.14}$$

The boundary condition of N in Equation (4.14) is of higher accuracy as the additional diffusivity is much larger than the molecular one. This is typical situation of sustained bubble nucleation in fully developed nucleate boiling. Solution of Equations (4.10) and (4.11); where all derivatives are with respect to η, provides information on the variation of Ψ and θ across the boundary layer.

The ordinary differential Equations (4.10) and (4.11) are characterized by their high sensitivity to the boundary values $\Psi''(0)$ and $\theta'(0)$, White (1991). In the current study, as the bubble activity changes, it induces corresponding changes in the additional diffusion, and hence in ε^+. This requires precise determination of $\Psi''(0)$ and $\theta'(0)$ at the lower boundary of the computational domain to meet the upper boundary conditions, i.e. Equation (4.14). For this purpose, an iterative solution procedure has been developed using the Runge–Kutta method and Matlab® to obtain the corresponding values of Ψ'' and θ' to the fifth or sixth decimal place at $\eta = 0$ to satisfy the upper boundary conditions for various values of ε^+ as listed in Table 4.1.

Figure 4.3 demonstrates the variations of Ψ, θ, and their derivatives with respect to η for $\varepsilon^+ = 10$.

Table 4. 1 Initial values of Ψ”(0), θ’(0) for different ε+ values

ε+	Ψ”(0)	θ’(0)
1	0.732978	0.33005
3	0.826835	0.32555
5	0.846944	0.32542
10	0.861121	0.31905
25	0.868753	0.31162
50	0.871068	0.30948
100	0.872174	0.30802
250	0.872818	0.3075
500	0□87303	0.307□
1000	0.873135	0.3071

When the value of the first derivative of the dimensionless temperature, θ’(0) is determined at the lower boundary of the computational domain, the heat flux transferred to the bulk flow as a result of the enhanced bubble-induced diffusion model can be obtained from Equation (4.15)

$$q''_{nb,\mathrm{mod}} = \rho_l c_p \varepsilon_{\max}\left(\frac{\partial T}{\partial y}\right)_{y=0} = \rho_l c_p (T_{sat} - T_\infty)\sqrt{\varepsilon_{\max} C}\left(\frac{d\theta}{d\eta}\right)_{\eta=0} \qquad (4.15)$$

In Equation (4.15), the effects of jet velocity and surface superheat on the boiling heat transfer rate are accounted for in the value of $\varepsilon_{\max}$, which also determines the temperature gradient $(d\theta/d\eta)_{\eta=0}$ at the bubbly layer top.

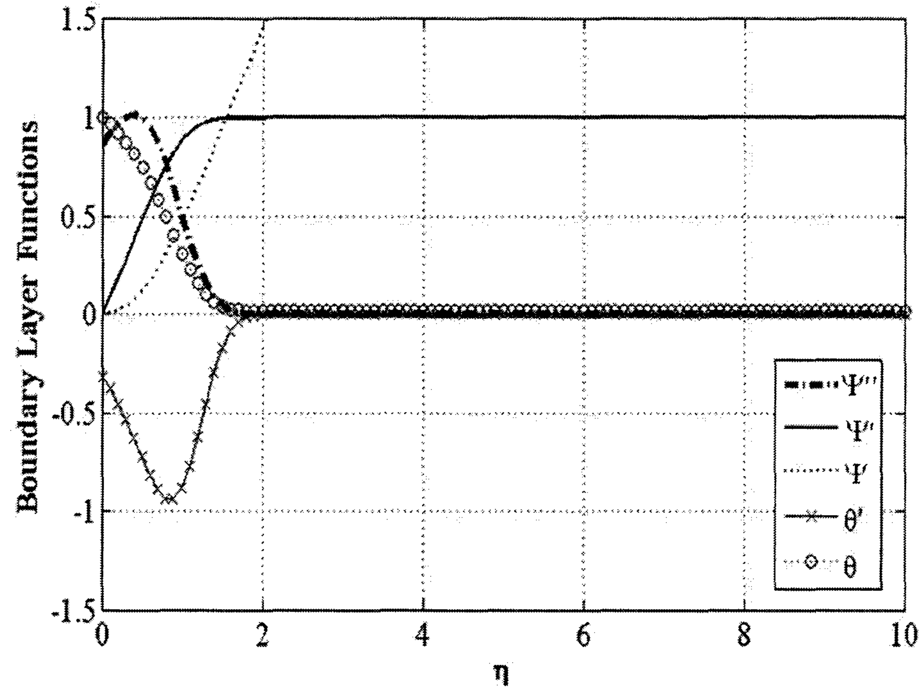

Figure 4. 3 Analytical solution of dimensionless boundary layer dimensionless functions (Case of $\varepsilon^+=10$, $\Psi''(0)=0.861121$, $\theta'(0)=-0.31895$)

4.4.2 Solution Procedure

The iterative solution procedure to obtain the theoretical values of the wall heat flux considering the bubble-induced diffusion is shown in Figure 4.4. Equation 4.15 is rearranged to obtain the following expression for the nucleate boiling heat flux as function of dimensionless total diffusivity ε^+:

$$q''_{nb,\mathrm{mod}} = \left(\varepsilon^+\right)^{0.5} \rho_l c_p (T_{sat} - T_\infty)\sqrt{\frac{\bar{C} V_n \nu}{w}}\left(\frac{d\theta}{d\eta}\right)_{\eta=0} \tag{4.16}$$

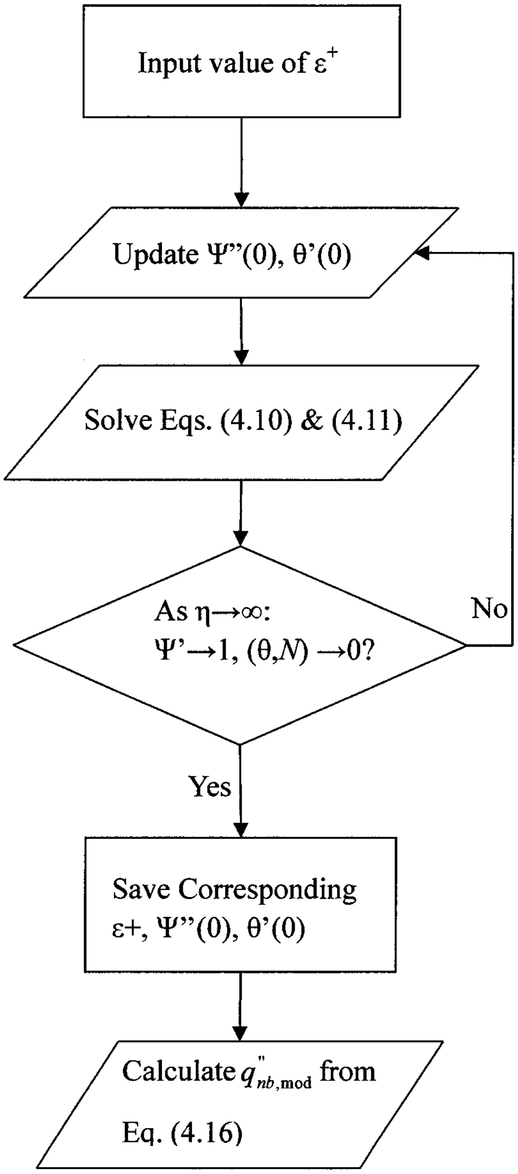

Figure 4. 4 Solution procedure of BID analytical model for known bubble-induced diffusivity.

To estimate the total heat flux from the wall to the jet flow, the nucleate boiling heat flux calculated from Equation (4.16) is added to the single-phase forced convection heat flux, q''_{sp} such that:

$$q''_w = q''_{sp} + q''_{nb,\mathrm{mod}} \tag{4.17}$$

Where

$$q''_{sp} = h_{sp}(T_s - T_\infty) \tag{4.18}$$

The single-phase heat transfer coefficient h_{sp} is calculated using the correlation developed in chapter 3, given by Equation (3.2).

Figure 4.5 shows the variation of nucleate boiling heat flux with the dimensionless total diffusivity ε^+ at various values of jet velocity and degree of sub-cooling. These variations indicate that a certain value of the boiling heat flux can be achieved using various combinations of these parameters. For example, the effect of increasing the jet velocity could be offset by decreasing the degree of liquid sub-cooling, so that boiling intensity would be maintained at the same level.

Substitution of an ε^+ value in Equation (4.16) and in the iterative solution of Equations (4.10) and (4.11) to obtain θ'(0) presents the frame work to obtain the model prediction of the nucleate boiling heat flux, $q''_{nb,\mathrm{mod}}$, provided that the used value of ε^+ is indeed the corresponding value to the combination of jet velocity, water subcooling, and surface superheat.

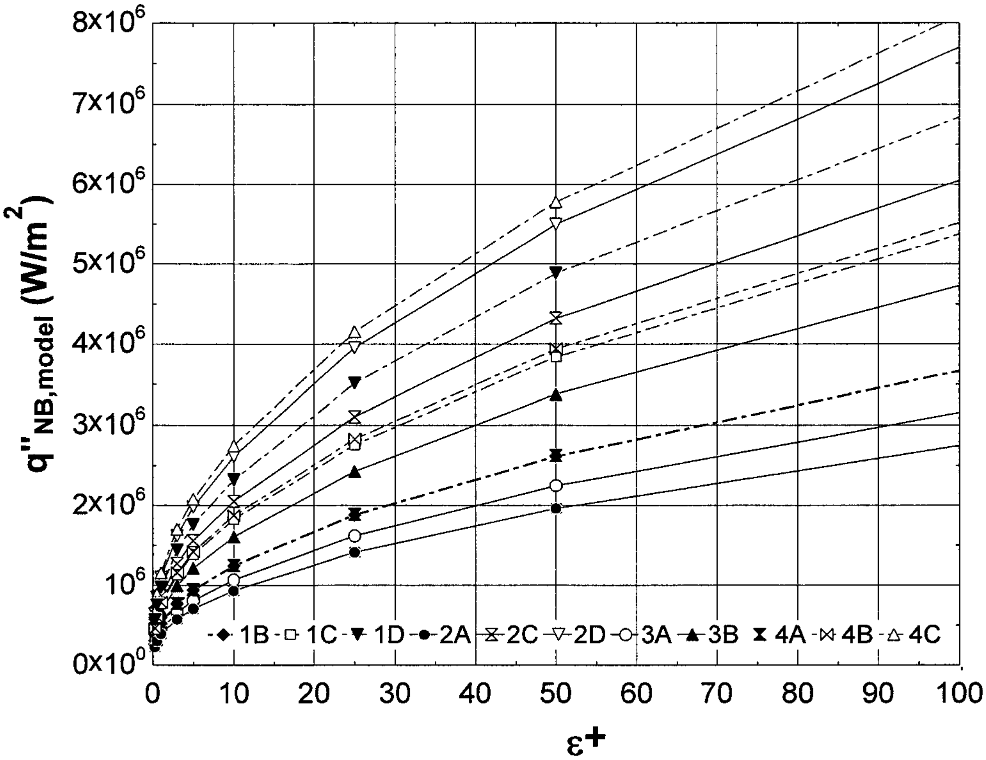

Figure 4. 5 Variation of $q''_{nb,\mathrm{mod}}$ with ε^+ at different flow conditions.

4.4.3 Model Closure

Since the bubble-induced diffusivity is not known a priori, it cannot be used as an independent input to predict the heat flux. Therefore, the analytical BID model would still need a relation that uses the practical inputs (i.e., surface temperature, jet velocity, and liquid temperature) to determine the corresponding ε^+. The experimental findings presented in chapter 3 were used to develop this relation. The following dimensionless groups were identified to represent all the parameters that control the bubble dynamics, and hence the values of ε^+:

$$\mathrm{Re}_b = \frac{V_j D_b}{\nu},\ We_b = \frac{\rho V_j^2 D_b}{\sigma},\ Ja_{\mathrm{sup}} = \frac{\rho_l c_p (T_s - T_{sat})}{\rho_v h_{fg}},\ Ja_{sub} = \frac{\rho_l c_p (T_{sat} - T_\infty)}{\rho_v h_{fg}} \quad (4.19)$$

The characteristic length in Reynolds number, Re_b, and Weber number, We_b, is the bubble diameter has been calculated by using Equation (3.9). This characteristic length is a better representation, as compared to fixed nozzle or heater dimensions, of the length scale over which flow-bubble interactions take place. It also accounts for the variation of bubble intensity and subsequent variation of the extent into the mean flow domain where the bubble-induced diffusion is effective. The development of the correlation between the practical inputs and the effective diffusivity has been carried out by applying the following procedure to various experimental combinations of jet velocity, degree of sub-cooling, and degree of superheat

1. Calculate the bubble diameter (D_b) using Equation (3.9) and the dimensionless groups, Re_b, We_b, $\mathrm{Ja}_{\mathrm{sup}}$, $\mathrm{Ja}_{\mathrm{sub}}$,using Equations (4.19).
2. Determine the portion of the heat flux due to single-phase heat transfer, using Equation (4.18).
3. The total heat flux to the surface is calculated from the finite difference analysis described in chapter 2.
4. The amount of heat transfer due to nucleate boiling in the experiment, $q''_{nb,\exp}$,is the difference between the total wall heat flux (step 3) and the single-phase heat flux (step 2).

5. Calculate ε^+ corresponding to the input flow velocity, water subcooling, and surface superheat from Equation (4.16) that is corresponding to $q''_{nb,\exp}$ and with the aid of the iterative solution depicted in Figure 4.4.

The following correlation has been developed using regression analysis of 55 experimental data points:

$$\varepsilon^+ = \frac{\mathrm{Re}_b^{x1}\, Ja_{\sup}^{x4}\, Ja_{sub}^{x5}}{\left(We_b^{x2} + x3\right)} \tag{4.20}$$

Where: $x_1 = -0.7736$, $x_2 = 4.283$, $x_3 = 5.634$, $x_4 = 4.167$, $x_5 = -1.586$.

The values of the constants x_1 to x_5 in Equation (4.20) reflect the expected effect of different forces and flow parameters on the intensity of bubble generation, and hence on the prediction of ε^+. By increasing the inertial forces, i.e., increasing Re_b, or by increasing the degree of sub-cooling, represented by Ja_{sub}, a lower ε^+ value is obtained. This is physically interpreted by the suppression an increase of flow velocity and/or liquid subcooling will induce to bubble nucleation on the heated surface due to flooding of nucleation sites and/or insufficient liquid superheat in the vicinity of the heated surface.

An increase in the degree of wall superheat, represented by Ja_{sup}, provides more appropriate environment in the vicinity of the heated surface to enhance bubble nucleation at higher frequency and for bubbles to grow to larger diameters which results in higher ε^+ values.

4.5 Model Validation

Figure 4.6 presents the difference between the BID model predictions of the total wall heat flux and the corresponding experimental values. The BID model predictions are in reasonable agreement with the experimental data with an overall deviation of +30% and -15%. This range of model accuracy was further validated using experimental data from a set of 11 experiments that were not included in the regression analysis. Table 4.2 lists the particulars of the validation experiments and the corresponding deviation from the experimental values. These predictions are within the same overall range of accuracy reported above.

Table 4. 2 Validation of BID hybrid analytical/empirical model

V_n / m s^{-1}	ΔT_{sub} /, ^oC	ΔT_{sat}/, ^oC	ε^+ (---)	q''_{exp} $MW.\ m^{-2}$	q''_{mod} $MW.\ m^{-2}$	*Relative Error%*
0.4	21	12.5	10.89	1.53	1.95	+27
0.75	10	10.5	8.5	1.17	1.22	+4.27
0.75	15	20	38.2	3.22	3.13	-2.73
0.75	28	19.7	27.5	4.9	4.83	-1.47
0.95	10	17	21	1.8	1.95	+8.39
0.95	10	25	53.3	3.3	2.89	-12.33
0.95	15	11	12.7	1.74	1.675	-3.74
0.95	22	15.5	10.5	2.87	2.98	+3.73
0.95	28	14.5	7.62	2.6	3.3	+27
1.25	15	7.7	1.36	1.22	1.34	+9.75
1.25	15	22	19.9	2.93	3.17	+8.26

The BID model predictions have also been compared with experimental data reported in previous investigations by Bartoli et al. (1997) and Robidou et al. (2002). Bartoli et al. (1997) carried out a set of steady-state experiments of boiling heat transfer in the stagnation zone of a planner jet impinging on the side of a stainless steel cylinder. Robidou et al. (2002) conducted a set of steady-state experiments of boiling heat transfer of a planer jet impinging in an open channel onto a horizontal flat copper surface. Figure 4.6 indicates that the proposed model is capable of predicting the stagnation heat flux of those experiments within the same overall range of accuracy.

The best agreement of the proposed BID model over the considered ranges of jet velocity and liquid subcooling in the current study was obtained at surface degree of superheat higher than 5 °C. Below this limit, the empirical closure correlation tends to overestimate bubble mixing. In real situations only few bubbles at such low superheat would be intermittently generated and be of little contribution to the total wall heat flux. So, the proposed BID model is capable of predicting JIB heat flux at boiling intensities specific to the fully developed nucleate boiling regime, where the bubble generation process and the bubble-induced mixing are sustained.

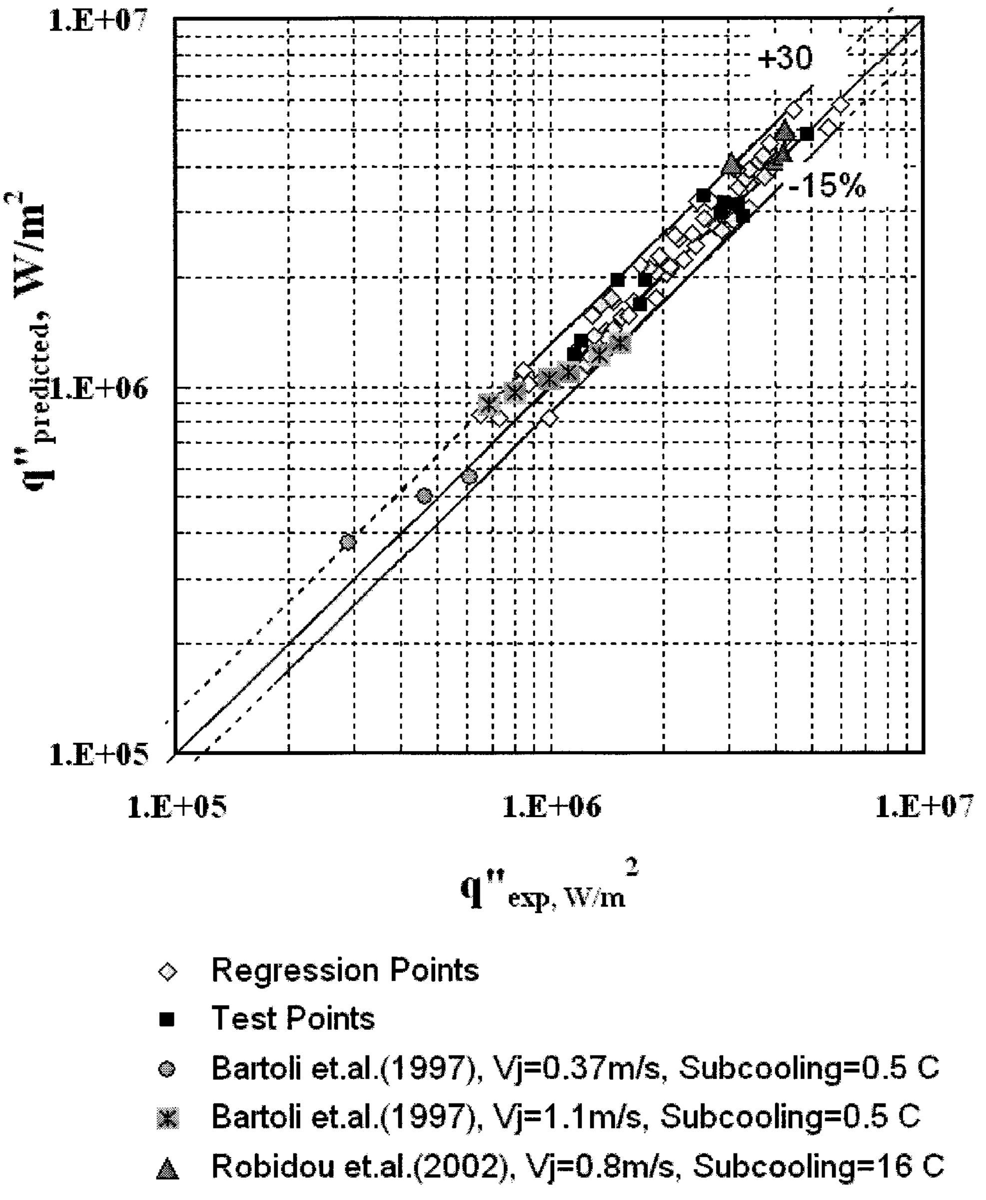

Figure 4. 6 BID model predictions of the total wall heat flux.

Chapter 5

The Development of a Scenario Identification Procedure (SIP) of Bubble Growth Termination in JIB

5.1 Introduction

When the bubble reaches its maximum diameter, it undergoes a certain growth termination scenario, which depends on the JIB, surface and jet, conditions. A mechanistic scenario identification procedure (SIP) has been developed to determine the corresponding bubble growth termination (BGT) scenario under various JIB conditions. It is postulated that the possible scenarios of BGT in nucleate JIB are: (1) bubble collapse (BC) at the nucleation site, or (2) bubble departure (BD) from the nucleation site. It has been assumed in study that the BD scenario would be associated with bubble sliding, rather than bubble taking off inside the liquid. This is in accordance with the observations made in PFB investigations by Basu (2003) given the relatively shorter heated surface length and the thin liquid film in the current study under JIB that did not allow for bubble migration into the liquid bulk Figure 5.1, illustrates the fraction of heated surface area that would be influenced by bubble in the two possible BGT scenarios. The determination of such area fraction is a key element for any mechanistic model of JIB heat transfer developed using the wall heat flux partitioning approach. The details of such model will be discussed in Chapter 6.

Previous studies assumed that only one BGT scenario prevailed (e.g., Unal (1976), Klausner et al. (1993), Steiner et al. (2005), and Narumanchi et al. (2008)). These investigations were focused on PFB. In the case of JIB, the complexity of the flow field caused by jet hydrodynamics makes it difficult to assume that one BGT scenario would be favored under all surface and jet conditions. Therefore, a SIP is needed in order to determine the most prevailing BGT scenario under different surface and jet conditions. The proposed SIP would also take into account the effect of possible variations in the liquid film thickness due to hydraulic jumps.

The following equilibrium conditions have been used in all previous studies to determine the bubble diameter and the corresponding BGT scenario

1) Thermal equilibrium between the bubble and the surrounding fluid. If thermal equilibrium is the effective BGT condition, a bubble would collapse without departure. In this case, the area of influence due to bubble collapse can be assumed to be equal to the projected bubble area, i.e., $A_{b,collapse} \sim (\pi D_b^2)/4$, where D_b is the bubble diameter at collapse.

2) Dynamic equilibrium of the acting forces on the growing bubble. If this condition is the effective BGT condition, a bubble would depart and slide downstream

for a certain distance L_{slid}, as shown in Figure 5.1. Depending on the value of L_{slid}, the sliding area could be approximated to the collapse area, i.e., ~ projected bubble area) if L_{slid} is within a bubble diameter. Otherwise the influenced area due to bubble sliding is equivalent to ($A_{b,sliding} \sim L_{slid} \cdot D_b$).

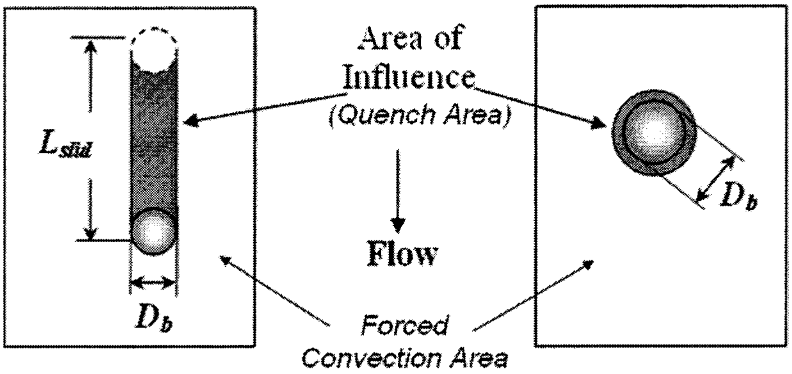

Figure 5. 1 Partitions of the heated surface area in the case of BD (left) and BC (right).

5.2 Physical Concept of BGT-SIP

The proposed SIP is based on determining the value of the bubble diameter required for each equilibrium condition to be established. The condition that would require a smaller bubble diameter would be the one that would be established first. And hence, it would be the condition that determines the possible BGT scenario. Therefore, bubble collapse without departure from the nucleation site would take place if thermal equilibrium is reached before dynamic equilibrium. Otherwise, bubble departure will take. To implement this SIP concept, the bubble diameter for each equilibrium condition has been calculated independently. The predicted bubble diameter at growth termination ($D_{b,pred}$) is the minimum of the two equilibrium diameters such that:

$$D_{b,pred}=Min\ [D_{th,eqm}, D_{dyn,eqm}] \tag{5.1}$$

Temporal variation of the bubble diameter during growth has been calculated using three different models. The accuracy of each model has been determined by comparing the diameter and the BGT scenario predicted by the SIP and the same obtained from the experiments.

5.3 Modeling Assumptions

The following assumptions have been used in the development of the growth termination SIP:

1. Flow is incompressible and steady.
2. The temperature profile in the thermal boundary layer is linear. The velocity profile is similar to that of a single-phase turbulent flow over a flat plate.
3. The growing bubbles are spherical in shape. This assumption has been verified during the preliminary tests to determine the appropriate viewing angle of the high speed camera as shown in the examples on Figure 5.2. While an oblique view of the flow filed was not the final choice in the current study, it helped in confirming the assumption of spherical bubble shape.

4. Bubbles receive heat by evaporation of superheated liquid at $T_{\sup} = (T_{sat} + T_s)/2$, within a uniform thickness layer adjacent to the heated surface. The thickness of the superheated layer is determined from knowing the thermal boundary layer thickness, as represented by Equation (5.14) and the degree of subcooling, together with assumption 2.
5. Bubbles can grow outside the superheated liquid layer. When this takes place, the growing bubble will be losing heat by condensation to the subcooled liquid layer at $T_f = (T_L + T_{sat})/2$ through the contact area with the subcooled liquid.

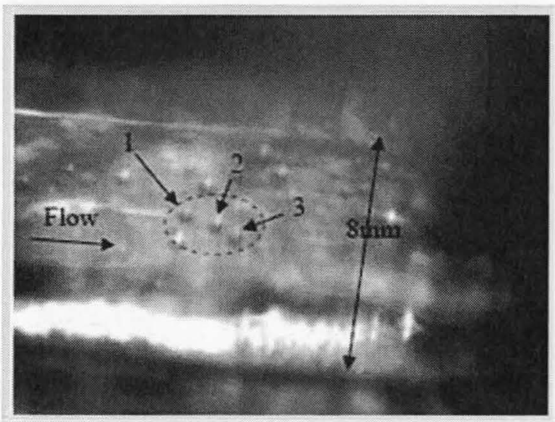

Figure 5.2 Visual observation of spherical bubble shape.

5.4 Mathematical Formulation of the SIP

5.4.1 Thermal Equilibrium Model

For a bubble to grow within a subcooled liquid, it receives heat from a superheated liquid layer in the vicinity of the nucleation site. This postulation is supported by previous studies such as that by Basu et al. (2005). Heat balance of a growing bubble shows that two heat flows control the bubble growth, as shown in Figure 5.3 and represented by Equation (5.2):

$$q_{b,in} = q_{b,cond} + \rho_v h_{fg} \frac{dV_b}{dt} = q_{b,cond} + \frac{\pi}{2} \rho_v h_{fg} D_b^2 \frac{dD_b}{dt} \tag{5.2}$$

A bubble would continue to grow as long as the heat input, $q_{b,in}$ from the superheated liquid heated surface is higher than the heat loss , $q_{b,cond}$ to the subcooled liquid due to condensation, provided that the diameter does not allow the dynamic equilibrium (force balance) to occur first, in which case the bubble would depart before it reaches thermal equilibrium.

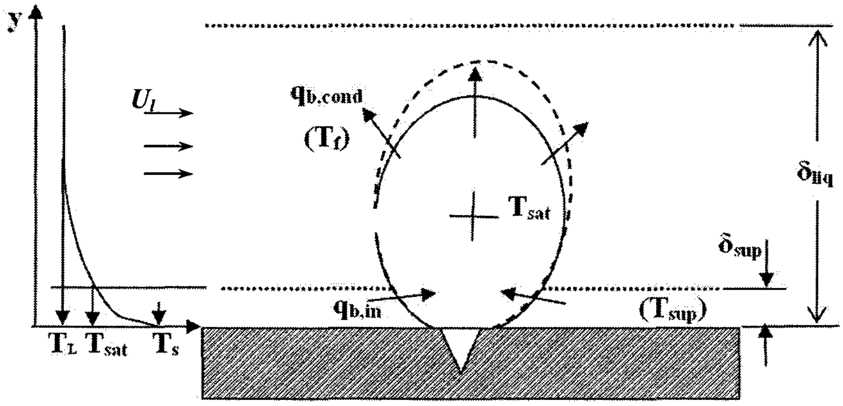

Figure 5. 3 Liquid temperature distribution heat flows to a growing bubble.

At thermal equilibrium, the second term on the right hand side of Equation (5.2) is equal to zero. At this point, the heat input due to liquid evaporation from the superheated layer at the lower portion of the bubble is balanced by the heat loss due to condensation to the subcooled liquid layer at the upper portion.

By partitioning the bubble surface area as shown in Figure 5.4, the area exposed to the superheated layer is equivalent to a spherical section of height δ_{sup}. This area is calculated using Equation (5.3):

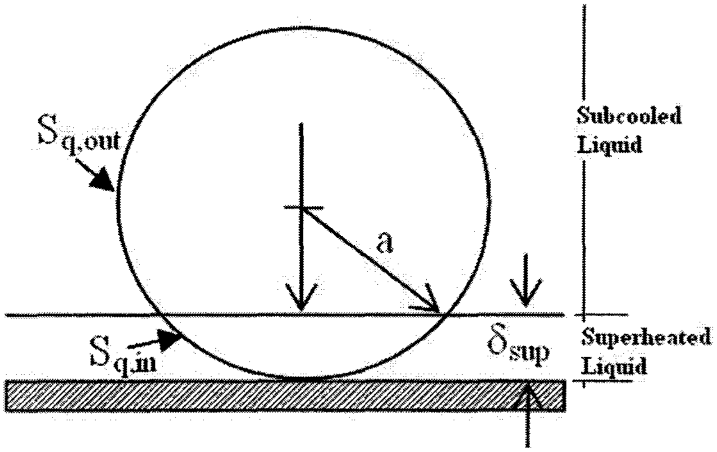

Figure 5. 4 Partitioning of the bubble surface area.

$$S_{q,in} = 2\pi a \delta_{\sup} \tag{5.3}$$

The heat flow through this area can be estimated for a given wall superheat using Equation (5.4) according to Unal (1976).

$$q_{b,in} = \sqrt{\frac{k_s \rho_s C_s}{\pi t}} S_{q,in} \Delta T_{\sup} \tag{5.4}$$

Where k_s, ρ_s, and C_s are the thermal conductivity, density, and specific heat of the surface material, in the current study it is pure Copper. The remaining area of the bubble that is exposed to the subcooled liquid is calculated using Equation (5.5):

$$S_{q,out} = S_{Bubble} - S_{q,in} = 4\pi a(a - \frac{\delta_{\text{sup}}}{2}) \tag{5.5}$$

And the heat loss due to condensation is calculated from Equation (5.6):

$$q_{b,out} = h_{sub} S_{q,out} (T_{sat} - T_L) \tag{5.6}$$

In order to determine the diameter at which thermal equilibrium is established, the second term on the right hand side of Equation (5.2) requires that the bubble growth rate dD_b/dt must be determined. Three growth models have been tested in the current study to determine $D_b(t)$. These three models are: Zuber model, modified Zuber model, and the Power growth model proposed by Zeng (1993) and discussed in further detail in the current study. Zuber model has been used in previous studies by Zeng et al. (1993), Klausner et al. (1993), and Steiner et al. (2005), where bubble growth has been assumed dependent on wall superheat as indicated by Equation (5.7):

$$D_b(t) = 4 \cdot b \cdot Ja_{\text{sup}} \cdot \sqrt{\frac{\alpha t}{\pi}} \tag{5.7}$$

In order to improve model prediction of the bubble diameter in PFB configuration, Zuber model has been modified in these studies by adjusting the value of the coefficient b in Equation (5.7). While b = 1 was used in the original Zuber model, Carey (1992), Steiner et al. (2005) used a value of b = 0.21 and Zeng et al. (1993) used a value of b = 1.73.

In the current study, a parametric study has been conducted to evaluate the value of *b* that should be used in a modified Zuber model to improve the accuracy of the developed SIP in predicting both the bubble diameter and the prevailing BGT scenario under JIB conditions. The determination of the optimum value of b has been based on trial of various values over the range found in previous literature where modifications to Zuber model have been reported. The optimum value would result in best achievable agreement of the bubble diameter and BGT scenario with experimental observations. An attempt to develop a third growth model , i.e., the Power growth model, has emerged from the postulation made by Zeng et al. (1993) which suggested that bubble growth can be expressed in the power form given in Equation (5.8)

$$D_b(t) = Kt^{n_1} \tag{5.8}$$

However, there was not any attempt in Zeng et al. (1993) to describe K or n_1. In the current study, the two coefficients were obtained from the experimental observations of individual bubble growth at jet velocity of 0.56 m/s which provided the clearest possible flow field. The following correlations have been developed from these observations for K and n_1:

$$K = 9.5E - 8(\Delta T_{\sup})^{3.96} \tag{5.9}$$

$$n_1 = 0.14(\Delta T_{\sup})^{0.36} \tag{5.10}$$

The condensation heat transfer coefficient has been calculated using the relation proposed by Unal (1976):

$$h_{sub} = \frac{aZ\phi h_{fg}}{(1/\rho_v - 1/\rho_l)} \tag{5.11}$$

Where Z = 65 at atmospheric pressure and

$$\phi = \left(\frac{U_l}{U_o}\right)^{0.47} \quad \text{for } U_l > 0.61\text{m/s} \tag{5.12}$$

$$\phi = 1 \quad \text{for } U_l \le 0.61\text{m/s} \tag{5.13}$$

$$U_o = 0.61 m/s \tag{5.14}$$

In Equations (5.12) and (5.13), U_l is the local mean film velocity. The superheated layer thickness at distance x from stagnation has been calculated using the thermal boundary layer thickness distribution proposed by Incropera and DeWitt (1996):

$$\delta_{th,x} = 0.37x / \sqrt[5]{\mathrm{Re}_x} \tag{5.14}$$

Based on assumption (2) above, the superheated liquid layer thickness is:

$$\delta_{\sup} = \delta_{th,x} \cdot r \tag{5.15}$$

Where

$$r = \frac{\Delta T_{\sup}}{\Delta T_{\sup} + \Delta T_{sub}} \tag{5.16}$$

For the range of velocity and distance from stagnation in the current study, the values of $\delta_{th,x}$ are in the order of 10^{-4} m. From the previous discussion in chapter 3 on the liquid film thickness variations with the jet velocity, it was observed that the liquid film thickness increases with the reduction in the jet velocity from a value approximately equal to half the jet width, i.e., δ_{liq}~0.5 mm at velocities greater than 1 m/s, to around 5mm at the lower limit of the velocity range. So, the thermal boundary layer would occupy larger fraction of the thinner liquid film at the higher levels of velocity. On the other hand, thermal boundary layer thickness would represent only smaller fraction of the total liquid film thickness and hence the majority of the liquid film is sufficiently subcooled. For the latter situation and together with the degraded drag force on the growing bubbles as jet velocity decreases, it would be expected that local bubble collapse would be more probable at low jet velocity. It is hence concluded that at the higher velocity levels, the heated wall boundary condition would penetrate further into the liquid film than it does at lower jet velocity cases for which larger fraction of the original liquid subcooling would be preserved within the bulk liquid. Energy balance would support this conclusion since less heat flux is being removed at lower jet velocity which means the increase in bulk fluid enthalpy is also limited and hence the jet subcooling is preserved to farther locations from the stagnation with the reduction in jet velocity.

Unlike Steiner et al. (2005), δ_{sup} was not used to limit the extent to which a bubble can grow. This condition was not applied here because of the values of bubble diameters obtained experimentally in the current study. Rather, δ_{sup} has been used to calculate the area fractions, $S_{q,in}$ and $S_{q,out}$.

Figure 5.5 shows the variation of the two heat flows to and from the bubble and the maximum bubble diameter $D_{b,th,eqm}$ at which the thermal equilibrium condition was established in the case of V_n=0.75 m/s, ΔT_{sup} = 20 °C, ΔT_{sub}=20 °C, and x/w=5 using the modified Zuber growth model to calculate the bubble growth rate.

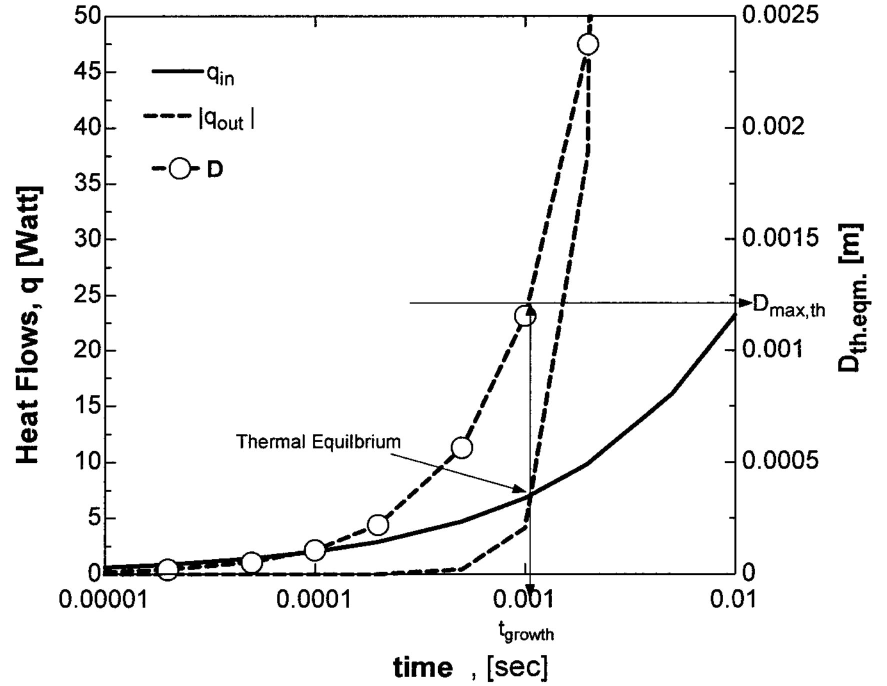

Figure 5. 5 Heat flows to and from a growing bubble and the maximum bubble diameter in the case of V_n=0.75 m/s, ΔT_{sup}=20 °C, ΔT_{sub}=20 °C, and x/w=5.

Figure 5.6 presents the variation of predicted maximum diameter at thermal equilibrium with jet velocity at various degrees of superheat. As the velocity is increased, the condensation heat transfer coefficient increases and so is $q_{b,cond}$. Also, the thermal boundary layer is thinner at higher jet velocities, which decreases the superheated layer thickness and contributes to the reduction of $D_{th,eqm}$. On the other hand, increasing the surface superheat results into larger δ_{sup}, according to Equations (5.15) and (5.16), which promotes bubble growth to larger diameters.

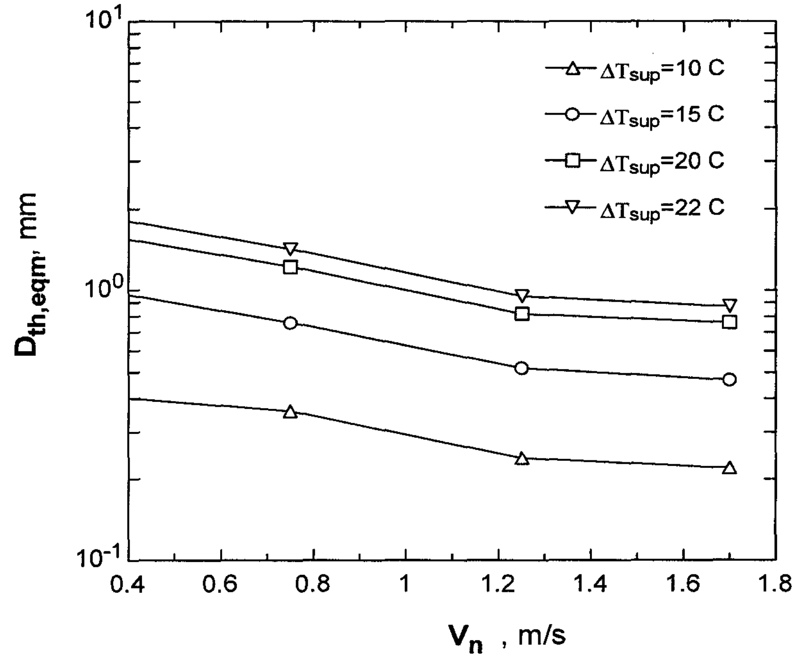

Figure 5.6 Variation of maximum bubble diameter under thermal equilibrium in the case of ΔT_{sub}=20 °C, and x/w=5)

5.4.2 Dynamic Equilibrium Model

The second part of the SIP is to determine the bubble diameter at which dynamic equilibrium is achieved, $D_{dyn,eqm}$. The forces acting on a growing bubble in jet impingement flow field are shown in Figure 5.7.

According to Zeng et al. (1993), the forces acting on a growing bubble on a horizontal heated surface are:

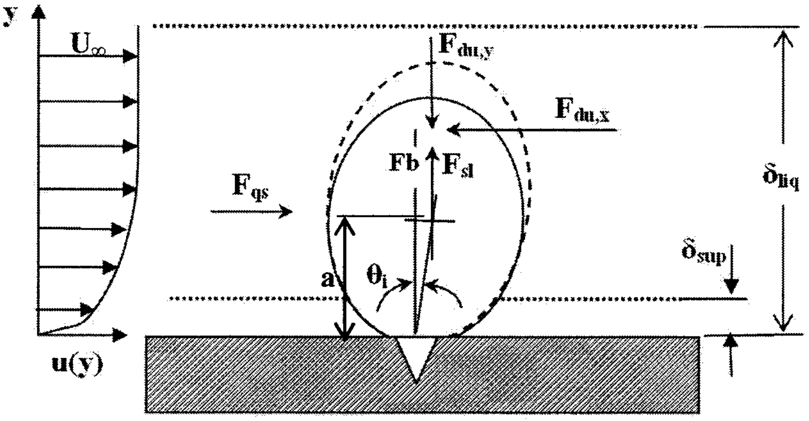

Figure 5.7 Velocity profile and forces acting on a growing bubble.

1. <u>A quasi-steady drag force,</u> ***F***

Equation (5.16) has been used to determine the instantaneous drag force, F_{qs} on a growing bubble of radius ***a***. This expression has been originally developed for unbounded flow over a sphere and was used by Klausner et al. (1993) in modeling of horizontal PFB in a closed conduit:

$$\frac{F_{qs}}{6\pi\rho_l \nu U_c a} = \frac{2}{3} + \left[\left(\frac{12}{\mathrm{Re}}\right)^n + 0.796^n\right]^{-1/n} \tag{5.16}$$

Where n=0.65 and

$$\mathrm{Re} = \frac{2U_c a}{\nu} \tag{5.17}$$

The velocity U_c in Equations (5.16) and (5.17) is the parallel flow velocity at the instantaneous center of the bubble, i.e. at $y=a$. In accordance with previous analysis of Zeng et al (1993), the following turbulent velocity profile for the parallel flow over flat plate has been used to calculate U_c.

$$\frac{u(y)}{u^*}=\frac{1}{\kappa}\ln\left(1+\kappa\frac{yu^*}{\nu}\right)+c\left[1-\exp\left(\frac{-yu^*}{\nu\chi}\right)-\left(\frac{-yu^*}{\nu\chi}\right)\exp\left(\frac{-0.33yu^*}{\nu}\right)\right] \tag{5.18}$$

Where $\kappa=0.41$, $\chi=11$, $c=7.4$ $\frac{u^*}{U}\approx 0.04$, and $U=\frac{V_n w}{2\delta_{liq.}}$ (5.19)

2. A growth force, ($\boldsymbol{F_{du}}$):

As bubbles grow on the heated surface, they attempt to displace the surrounding liquid. Due to its inertia, the liquid reacts to such displacement by a force F_{du} on the growing bubble. This force is, thus, responsible for maintaining the bubble at its nucleation site. The growth force, F_{du} can be calculated from Equation (5.20) proposed by Klausner et al. (1993):

$$F_{du}=-\rho_l\pi a^2\left(\frac{3}{2}\dot{a}^2+a\ddot{a}\right) \tag{5.20}$$

The growth force is decomposed into a horizontal component, $\boldsymbol{F_{dux}}$, that is opposite to the flow direction and a vertical component, $\boldsymbol{F_{duy}}$, in the normal direction pointing onto the heated surface. These two components have been calculated using Equations (5.21) and (5.22):

$$F_{dux} = F_{du} \sin\theta_i \tag{5.21}$$

$$F_{duy} = F_{du} \cos\theta_i \tag{5.22}$$

Due to the flow drag, a growing bubble is distorted in the flow direction with an angle θ_i. This angle of inclination is considered unknown and is determined simultaneously with dynamic equilibrium bubble diameter, $D_{dyn,eqm}$.

3. A buoyancy force, F_b:

Due to the density difference between vapour and liquid, a buoyancy force attempts to detach the bubble from the heated surface. F_b can be calculated from:

$$F_b = \frac{4\pi}{3} a^3 (\rho_l - \rho_v) g \tag{5.23}$$

4. A shear lift force, F_{sL}:

This force also acts on detaching the bubble from the surface in the normal direction as shown in Figure 5.7. Equation (5.24) has been used to determine the shear lift force. This Equation has been used in previous analysis by Zeng et al. (1993) and Klausner et al. (1993) for shear lift of a bubble on a solid surface:

$$\frac{F_{sL}}{\frac{1}{2}\rho_l U_l^2 \pi a^2} = 3.877 G_s^{0.5}\left[\mathrm{Re}^{-2} + 0.014 G_s^2\right]^{0.25} \tag{5.24}$$

Where G_S is a dimensionless shear rate:

$$G_s = \left|\frac{dU_l}{dy}\right| \frac{a}{U_l} \tag{5.25}$$

The values of all acting forces at the instant of dynamic equilibrium are plotted against the corresponding levels of jet velocity in Figure 5.8. The dynamic equilibrium diameter ($D_{dyn.,eqm}$) and the inclination angle θ_i at departure are determined from the solution of the following two simultaneous Equations the represent the force balance conditions:

$$\sum F_x = F_{qs} + F_{du} \sin\theta_i = 0 \tag{5.26}$$

$$\sum F_y = F_b + F_{du} \cos\theta_i + F_{sL} = 0 \tag{5.27}$$

In the aforementioned analysis of the acting forces on a growing bubble, the surface tension has been assumed to be negligible small because of the small circumference corresponding to the contact area with the heated surface under the assumption of spherical bubble shape which was confirmed from the visual observations. Such assumption was also supported by the analysis provide by Zeng et al. (1993). Once the diameter value is known, it can be substituted in the growth model Equation (i.e., Equation (5.7) or Equation (5.8)) to determine the time required to reach dynamic equilibrium. The variation of the dynamic equilibrium bubble diameter, $D_{dyn,eqm}$, with jet velocity is shown in Figure 5.9. An increase in jet velocity decreases $D_{dyn,eqm}$. This is because as the free stream velocity increases, the velocity boundary layer thickness decreases, and the free stream velocity is reached at relatively closer distance to the surface. This results in higher drag and shear lift forces. In addition, condensation loss is promoted at higher jet velocities which will reduce the bubble growth rate. Reaction to liquid displacement due to bubble growth is less under slowed growth rate. Thus, liquid inertia force, F_{du} would be less at higher jet velocity.

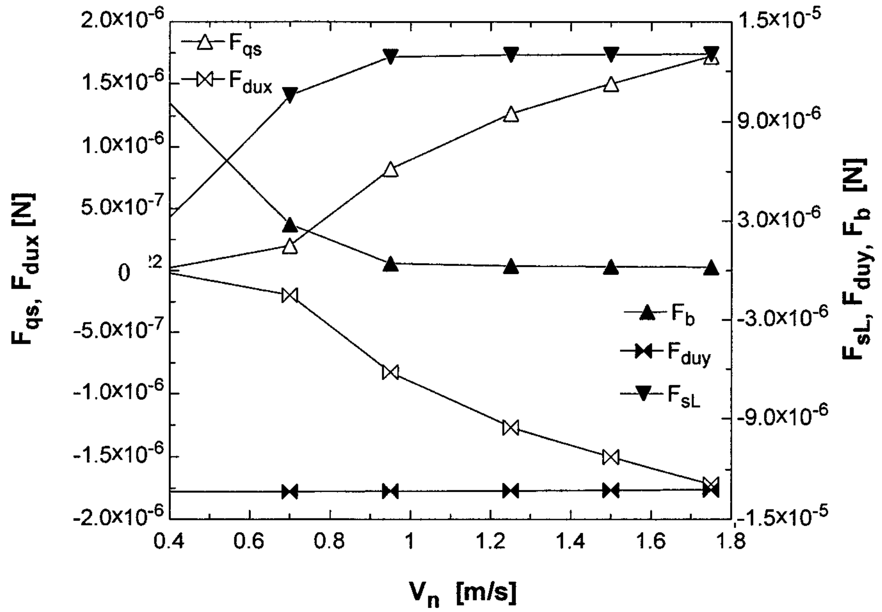

Figure 5. 8 Variation of forces acting on a bubble at dynamic equilibrium. (Case: ΔT_{sup}=15 °C, ΔT_{sub}=20 °C)

As drag force increases with the velocity, dynamic equilibrium is reached at relatively small bubble diameters. On the contrary, if at a certain jet velocity, the surface superheat is increased; it would promote the bubble growth rate. In reaction to the accelerated liquid displacement due to the increase in bubble growth rate, the growth resistance forces (i.e., F_{dux} and F_{duy} due to liquid inertia), would increase. Drag force may thus not be able to balance the liquid inertia force until relatively larger bubble diameter is reached under the elevated surface superheat.

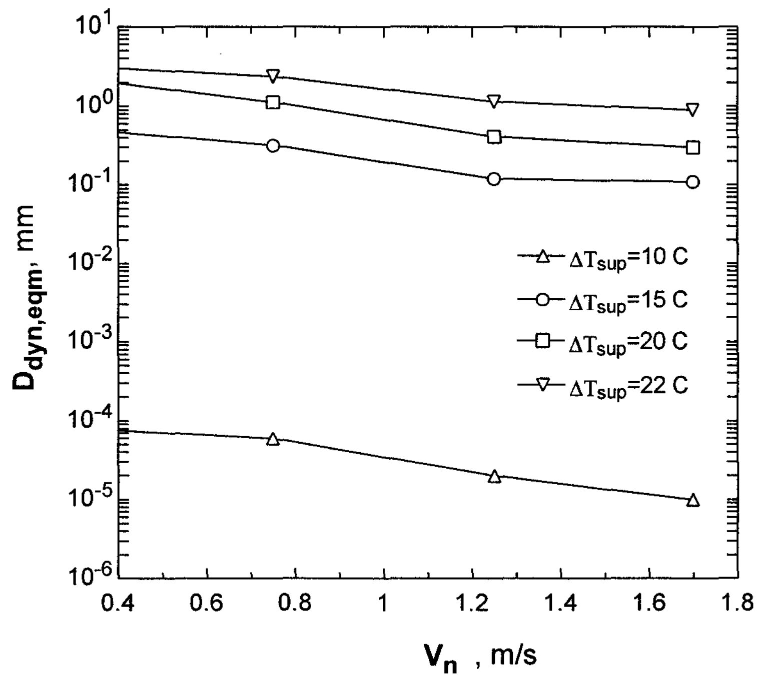

Figure 5. 9 Variation of Ddyn with jet velcocity and degree of superheat in the case of ΔT_{sub}=20 °C and x/w=5

5.4.3 Closure of SIP

To implement the proposed SIP in determining the thermal and dynamic bubble diameters in nucleate JIB, the mean liquid film velocity, U_l needs to be calculated at the bubble nucleation site. As discussed in chapter 3, free impingement liquid film velocity in the parallel direction to the heated surface is affected by the variation of liquid film thickness and the possible formation of hydraulic jumps. This has to be considered in the proposed SIP calculations. As presented in chapter 3, the location of the hydraulic jump, X_{hj}, measured from jet stagnation, has been correlated as:

$$\frac{X_{hj}}{w} = 6.51 \cdot V_n^{2.67} \tag{5.28}$$

If the nucleation site is at a distance less than X_{hj}, then it would be in the upstream region of the hydraulic jump, where the liquid film thickness is δ_1=w/2. Otherwise, the liquid film thickness, δ_2, downstream of the hydraulic jump can be calculated from the correlation discussed in chapter (3) and presented here in Equation (5.29):

$$\frac{\delta_2}{\delta_1} = 1 + 30.4e^{-3.25V_n} \tag{5.29}$$

Consequently, from the conservation of liquid mass, the mean liquid film velocity can be calculated downstream of the jump using Equation (5.30):

$$\frac{U_2}{U_1} = \frac{\delta_1}{\delta_2} \tag{5.30}$$

Where the mean liquid velocity upstream the jump, U_l is assumed to be equal to the jet velocity.

5.5 Model Validation

The agreement in the predicted bubble diameter and prevailed BGT scenario are the two criteria that have been used to validate the developed SIP. Details of four validation cases are presented below to demonstrate how the SIP predicts the maximum bubble diameter and the corresponding BGT scenario for a set of surface and jet conditions (i.e., a certain jet velocity, subcooling, surface superheat) and at a certain nucleation site located upstream or downstream of a hydraulic jump.

Case 1:

- V_n=0.4 m/s, ΔT_{sub}=10 °C, ΔT_{sup}=20 °C, x/w=5.
- Experimental observations: location is downstream a hydraulic jump, $D_{max,avg}$~2.4 mm. Observed termination scenario: Bubble Collapse prevailed.
- Model Prediction: $D_{max}=D_{th.eqm}$=2 mm, predicted termination scenario: Bubble Collapse as thermal equilibrium preceded the dynamic equilibrium. ($D_{dyn,eqm}$=2.7mm)

Case 2:

- V_n=0.75 m/s, ΔT_{sub}=20 °C, ΔT_{sup}=20 °C, x/w=2
- Experimental observations: location is upstream a hydraulic jump, $D_{max,avg}$~0.25 mm. Observed termination scenario: more likely bubbles slide few diameters downstream before collapse.
- Model Prediction: $D_{max}=D_{dyn,eqm}$=0.4 mm, predicted termination scenario: Bubbles slide as dynamic equilibrium is reached first. (whereas $D_{th,eqm}$=0.8 mm)

Case 3:

- V_n=0.75, ΔT_{sub}=20 °C, ΔT_{sup}=20 °C, x/w=5
- Experimental observations: location is downstream a hydraulic jump, $D_{max,avg}$=0.76 mm. Observed termination scenario: Bubble Collapse and sliding are both observed at relatively equal frequencies.
- Model Predictions: $D_{max}=D_{dyn,eqm}$=1.15 mm, predicted termination Scenario: Bubble Slide.

In this particular case, both diameters were close to each other. $D_{th,eqm}$=1.22 mm, which indicates the qualitative agreement with the experimental observations.

Case 4:

- V_n=1.25, ΔT_{sub}=20 °C, ΔT_{sup}=15 °C, x/w=5
- Experimental observations: No hydraulic jump observed, $D_{max,avg}$ = 0.15 mm. Observed termination scenario: Bubble sliding prevailed.
- Model Prediction: D_{max}=$D_{dyn,eqm}$=0.12, predicted termination scenario: Bubble Sliding ($D_{th,eqm}$= 0.52 mm)

Testing of the uncertainty in the predictions of the maximum attainable diameter are shown in Figure 5.10 for twenty validation cases under various flow conditions. Figure 5.10 shows the effect of the bubble growth model by comparing the predictions of three growth models: Zuber model, modified Zuber model and the Power growth model, on the predictions of the SIP. Using the modified Zuber model with *b=0.3,* the maximum value obtained for the coefficient of determination R^2 was 0.68 using the modified Zuber growth model.

Table 5.1 lists the experimental and predicted BGT scenarios for the twenty validation cases shown in Figure 5.10. In table 5.1, whenever the SIP prediction of the BGT scenario is not in accordance with the experimentally observed scenario, an (X) has been added next to the SIP prediction. Using the modified Zuber model has resulted in the best success rate of predicting the right BGT scenario with an agreement of about 80% with the experiments.

A pragmatic approach to improve the SIP predictions, by using trial and error was implemented to modify Zuber model such that for the free JIB configuration in the current study, the value of ***b* = *0.3*** in Equation (5.7) resulted in agreement with 80% of the experimental observations.

To explain the effect of the various bubble growth models on the SIP predictions, it was evident that the higher the value of ***b*** in the Zuber model, the higher the growth rate becomes, which promotes F_{dux}, and F_{duy} . These forces act on keeping a growing bubble at its nucleation site. This resulted in delaying the dynamic equilibrium condition when using Zuber model; i.e., b =1, as reflected in Table 5.1 by having all the SIP predictions in favour of bubble collapse and by over predicting the bubble diameter, as shown in Figure 5.10.

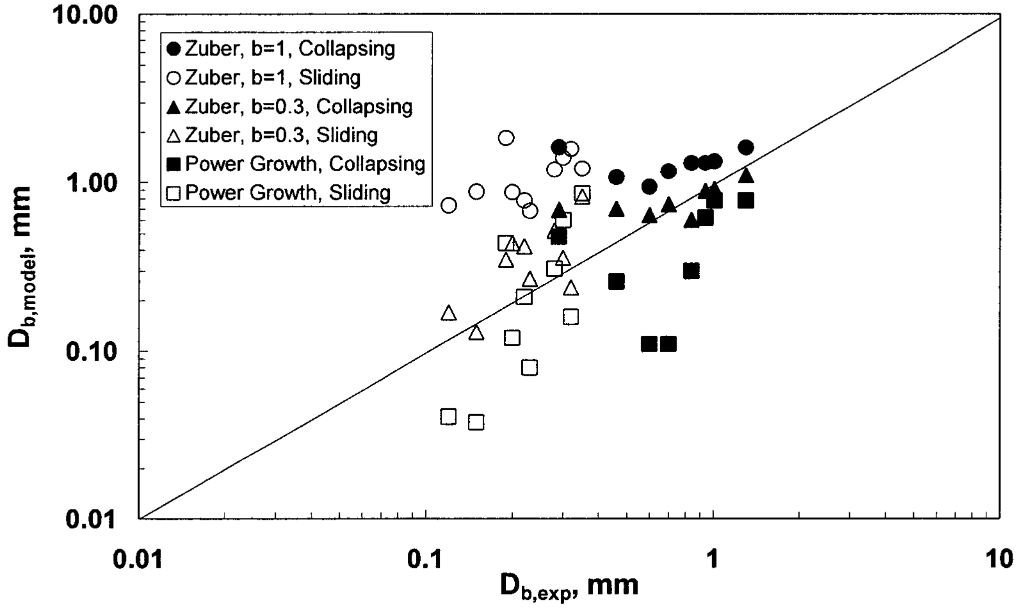

Figure 5. 10 SIP predictions of the maximum bubble diameter

On the other hand, using the power growth model has caused the SIP to predict bubble sliding as the BGT scenario in cases where experiments show bubbles collapsing at their nucleation site. This indicates an under prediction of the bubble growth rate using the power growth model such that the liquid inertia force are balanced by the drag force at smaller diameters than experimentally observed.

Table 5. 1 SIP predictions of BGT scenario

Re_w	Ja_{sub}	Ja_{sup}	Exp. BGT Scenario	SIP (Zuber, b=1)	SIP (Modified Zuber, b=0.3)	SIP (Power Growth Model)
1765	78.2	33.1	Collapsing	Collapsing	Collapsing	Sliding (X)
1818	78.1	50.2	Collapsing	Collapsing	Collapsing	Sliding (X)
1835	57.0	34.5	Collapsing	Collapsing	Sliding (X)	Sliding (X)
1886	57.0	51.0	Collapsing	Collapsing	Collapsing	Sliding (X)
1913	56.9	59.9	Collapsing	Collapsing	Collapsing	Collapsing
2510	66.1	40.5	Collapsing	Collapsing	Sliding (X)	Sliding (X)
2554	66.0	51.0	Collapsing	Collapsing	Collapsing	Sliding (X)
2563	23.0	39.1	Sliding	Collapsing (X)	Sliding	Sliding
2563	44.9	47.9	Collapsing	Collapsing	Sliding (X)	Sliding (X)
2584	51.0	42.9	Collapsing	Collapsing	Sliding (X)	Sliding (X)
2994	84.2	39.1	Sliding	Collapsing (X)	Sliding	Sliding
3088	84.1	57.1	Collapsing	Collapsing	Collapsing	Sliding (X)
3136	66.0	48.0	Sliding	Collapsing (X)	Sliding	Sliding
3183	45.0	36.0	Sliding	Collapsing (X)	Sliding	Sliding
3293	29.9	41.9	Sliding	Collapsing (X)	Sliding	Sliding
3341	29.9	50.9	Sliding	Collapsing (X)	Sliding	Sliding
4043	66.1	36.0	Sliding	Collapsing (X)	Sliding	Sliding
4105	66.0	45.0	Sliding	Collapsing (X)	Sliding	Sliding
4250	30.0	30.0	Sliding	Collapsing (X)	Sliding	Sliding
4416	29.9	53.9	Sliding	Collapsing (X)	Sliding	Sliding
Correct SIP Predictions %				**50 %**	**80%**	**55%**

Chapter 6

Wall Flux Partitioning Model of JIB Heat Transfer

6.1 Introduction

In this chapter, the details of a mechanistic model of JIB heat transfer are presented. The model has been developed to determine the distribution of the total wall heat flux along the heated surface using the wall flux partitioning (WFP) approach.. The total heat flux from the heated surface during nucleate JIB has been divided into two primary partitions: (1) the forced convection heat flux partition, which represents the amount of heat transfer that takes place on parts of the heated surface area where no bubbles are generated, and (2) the transient conduction heat flux partition, which represents the amount of heat transfer due to the replacement of the collapsed or departed bubbles by the liquid.

A hypothesis of *boiling reversed energy cascade* has been postulated in the current study to represent the heat flow from the heated surface to the fluid bulk. The word '*reversed*' here is used to describe the energy flow during JIB in analogy with the conventional energy cascade in turbulent flows from the fluid bulk to the wall, White (1996).

6.2 Physical Concept of the Present WFP Model

The present WFP model is based on the concept of mutual occurrence of different heat transfer mechanisms at different locations on the heated surface. The contribution of each partition to the total heat flux varies with the intensity of bubble generation. The basic foundation of the present model is similar to that of Basu (2003) which postulated that the total rate of heat transfer between the heated surface and the mean fluid flow is primarily due to sensible heating of the liquid. Vapor content of the flow in this heat transfer configuration would increase if the enthalpy of the mean flow is higher than that of saturated liquid, Carey (1992). As shown in Figure 6.1, three successive levels of heat transfer from the heated surface to the liquid bulk are hypothesized to take place during JIB forming a Boiling Reversed Energy Cascade (BREC). These levels are:

1- Level (1), direct sensible heating of the liquid in the vicinity of the heated surface by single-phase forced convection and transient conduction. Transient conduction only takes place as a consequence of bobble growth termination (BGT). Otherwise, only single-phase forced convection is responsible for heat transfer in Level (1).

2- Level (2), evaporation of superheated liquid in the vicinity of the heated surface at the interface of bubble embryos. Such evaporation is responsible for bubble growth.

3- Level (3), indirect sensible heating of liquid due to condensation of vapor bubbles as they protrude into the subcooled liquid layer.

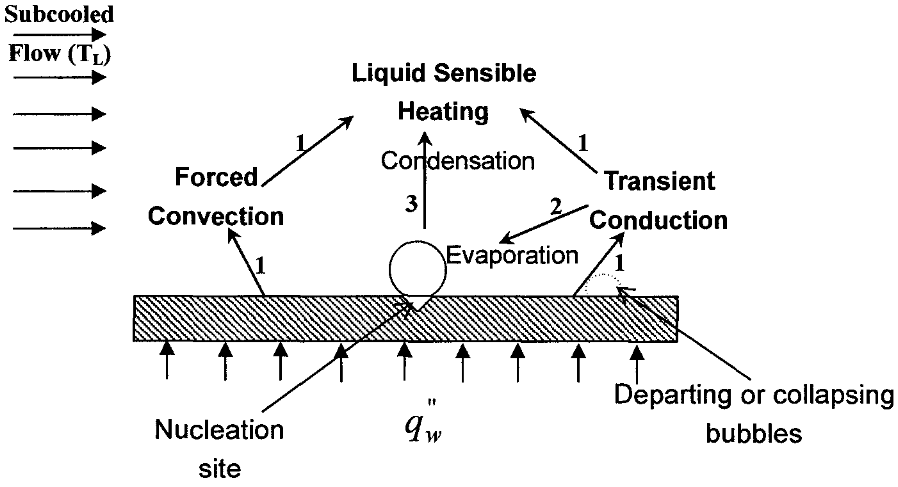

Figure 6. 1 Illustration of the proposed boiling reversed energy cascade (BREC) in JIB. Numbers on the arrows represent the BREC level.

The total wall heat flux can be obtained by determining the wall flux partitions of Level (1). This calculation requires that the area fractions of the heated surface and the duration of each mechanism are identified. The area fraction where transient conduction takes place can be determined by identifying the bubble population intensity, bubble diameter, and bubble growth termination scenario. Figure 6.2 shows a plan view of the heated surface downstream of the jet. The Figure shows the method used in the present wall flux partitioning model to calculate the transient conduction and forced convection areas. The calculation of these areas depends on whether the BGT process is thermal equilibrium dependent or dynamic equilibrium dependent.

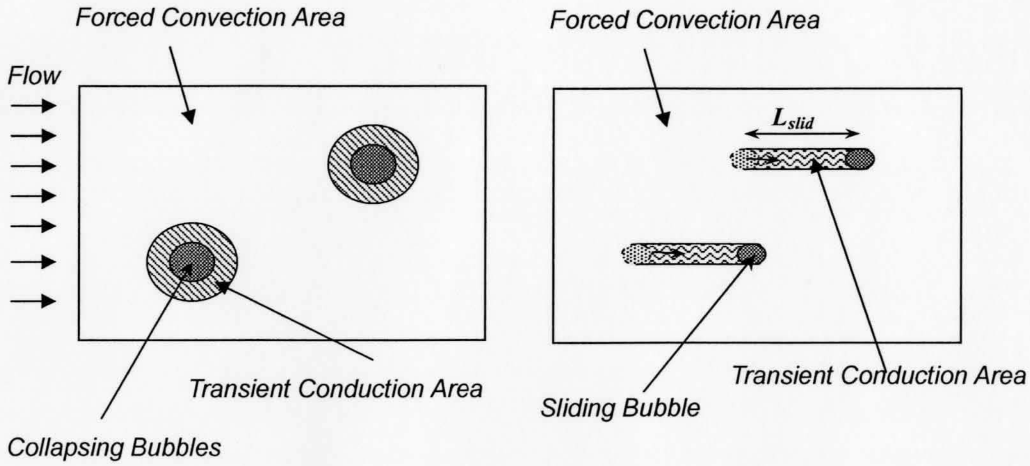

Figure 6. 2 The calculation of the transient conduction area in the present wall flux partitioning model, left: the case of collapsing bubbles without sliding, right: the case of sliding bubbles.

6.3 Modeling Assumptions

The following assumptions have been used to develop the JIB-WFP model:

1. Flow is incompressible and steady.
2. Bubble generation starts when the wall superheat reaches ΔT_{ONB}. This parameter has been modeled in terms of flow velocity, subcooling and distance from the jet stagnation in chapter 3, Equation (3.9).
3. Single phase heat transfer coefficient is enhanced due to bubble generation. The level of enhancement varies with nucleation intensity. This hypothesis is discussed later in this

chapter.

4. The greater of forced convection heat transfer rate and transient conduction heat transfer rate takes place over the area influenced by BGT. This assumption has been adopted previously by Basu (2003) to account for temporal changes in heat transfer mechanisms during long waiting periods on area fractions that are intermittently occupied by bubbles.

5. At stagnation, only bubble collapse is considered as the only possible BGT scenario where bubbles are exposed to normal jet flow and no flow drag parallel to the surface is acting on them. At downstream locations, the BGT scenario is determined based on the local flow velocity and surface superheat.

6.4 Mathematical formulation of the Present WFP Model

At level (1) of the BREC, the wall heat flux, q_w'', is assumed to be transferred to the liquid bulk through two mechanisms: forced convection and transient conduction. The later starts to take place as bubble nucleation starts. Consequently, the wall heat flux can be expressed by Equation (6.1)

$$q_w'' = q_{fc}'' + q_{tc}'' \tag{6.1}$$

The forced convection heat flux partition, q_{fc}'', is calculated using Newton's cooling law, i.e.,:

$$q''_{fc} = h_{fc} * A_{fc} * (T_s - T_L) \tag{6.2}$$

The transient heat conduction partition, q''_{tc}, is determined by assuming a sudden change in the surface temperature of the liquid film due to one dimensional heat conduction from the heated surface. The instantaneous transient conduction heat flux is calculated using Equation (6.3), Incropera and DeWitt (1996):

$$q''_{tc}(t) = \frac{\sqrt{k_l \rho_l c_{p,l}}}{\sqrt{\pi t}}[A_{tc}(T_s - T_L)] \tag{6.3}$$

Since transient conduction heat transfer follows bubble departure or collapse, this heat flux partition takes place on an area fraction $0 < A_{tc} < 1$ of the heated wall that is equal to the bubble projected area or the bubble sliding area. The calculation of A_{tc} depends on the BTG scenario as follows:

i- in case of a collapsing bubble:

$$A_{tc} = A_{tc,col} = N''(\frac{\pi}{4} D^2_{\max}) \tag{6.4}$$

ii- in case of a sliding bubble:

$$A_{tc} = A_{tc,sl} = N'' L_{slid} D_{\max} \tag{6.5}$$

Consequently, the forced convection area $A_{fc}=1-A_{tc}$ is the remaining fraction of the heated surface areas that is subjected *permanently* to forced convection.

Comparing Equations (6.2) and (6.3), it is evident that as q''_{fc} remains constant with time and $q''_{tc}(t)$ starts at high value and decays with time, there is a period of time, t_{TC}, over which transient conduction is more significant than forced convection.

This period can be greater, equal, or less than the waiting time, t_w, which is the period between a bubble collapse or departure and the start of the next bubble growth.

Depending on the difference in the instantaneous values of the two heat flux partitions, either only transient conduction takes place on A_{tc}, or if heat transfer rate due to transient conduction is less than single-phase forced convection heat transfer rate, the latter will also take place on A_{tc} for the remainder of the t_W; i.e., for a period equals to (t_w-t_{TC}). The present WFP model takes these possibilities into account.

The present WFP model, thus, encompasses two types of partitioning: spatial partitioning of the whole heated surface area into A_{fc} and A_{tc}, and temporal partitioning of A_{tc}, when necessary. The total wall heat flux will be the time averaged flux from both partitions over a bubble life cycle $t_{cycle}=t_w+t_g$.

Transient conduction heat flux is averaged as shown in Equation (6.6)

$$q''_{tc,avg}=\frac{1}{t_{cycle}}\int_0^{t_{TC}}\frac{\sqrt{k_l\rho_l c_{p,l}}}{\sqrt{\pi\, t}}[A_{tc}(T_s-T_L)]d\tau \tag{6.6}$$

Although forced convection is not changing with time, it always takes place at A_{fc} and under some conditions at A_{tc} for part of t_w. To account for all cases, forced convection heat flux is assumed to be composed of two sub-partitions:

$$q''_{fc}=q''_{fc1}+q''_{fc2} \tag{6.7}$$

Where:

$$q''_{fc1} = h_{fc} A_{fc} (T_s - T_L) \tag{6.8}$$

And

$$q''_{fc2} = h_{fc} A_{tc} (T_s - T_L)(\frac{t_w - t_{TC}}{t_{cycle}}) \tag{6.9}$$

To determine if q''_{fc2} shall be considered, the transient conduction domination period (t_{TC}) has been calculated by equating Equations (6.2) and (6.3).

$$\frac{\sqrt{k_l \rho_l c_{p,l}}}{\sqrt{\pi\, t_{TC}}} [A_{tc}(T_s - T_L)] = h_{fc}[A_{tc}(T_s - T_L)] \tag{6.10}$$

t_{Tc} can be calculated using Equation (6.11), which is determined by solving Equation (6.10) for t_{Tc}.

$$t_{TC} = \frac{1}{\pi \alpha_l} \left(\frac{k_l}{h_{fc}} \right)^2 \tag{6.11}$$

The temporal partitioning cases are determined as follows:

Case 1: if $t_{TC} > t_{cycle}$

In this case, t_{TC} is limited to t_w and hence q''_{fc2} is zero. This is typical in the case of high superheat, where large bubble sizes and/or high bubble release frequency prevail.

The wall heat flux can be calculated in this case using Equation (6.12):

$$q''_w = q''_{fc1} + q''_{tc} = \left(h_{fc} A_{fc} + \frac{2k_l A_{tc} \sqrt{t_w}}{t_{cycle} \sqrt{\pi \alpha_l}} \right) (T_s - T_L) \tag{6.12}$$

Case 2: if $t_w < t_{TC} < t_{cycle}$

This case is similar to case 1 above and hence the total heat flux is calculated using Equation (6.12).

Case 3: if $t_{TC} < t_w$

There will be a period of time equal to $(t_w - t_{TC})$ over which forced convection q''_{fc2} will take place at A_{tc} until the next bubble starts to grow. The wall heat flux in this case is calculated using Equation (6.13)

$$q''_w = q''_{fc1} + q''_{fc2} + q''_{tc} = \left[h_{fc} \left(A_{fc} + A_{tc} \left(\frac{t_w - t_{TC}}{t_{cycle}} \right) \right) + \frac{2k_l A_{tc} \sqrt{t_{TC}}}{t_{cycle} \sqrt{\pi \alpha_l}} \right] (T_s - T_L)$$

(6.13)

6.5 Model Closure

In order to determine which case of heat flux partitioning applies and hence which of Equations (6.12) or (6.13) should be used to calculate the total wall heat flux, the values of h_{fc}, A_{tc}, A_{fc}, t_{TC}, t_{cycle} and t_w must be determined as functions of jet velocity, V_n, liquid temperature, T_L, surface temperature, T_s, and location from the stagnation point. x, The forced convection heat transfer coefficient, h_{fc} at downstream locations from the jet can be determined as a function of the stagnation heat transfer coefficient, h_o by applying the shape factor discussed in section 3.2. to account for the experimentally observed waviness in the spatial distribution of the forced convection heat transfer coefficient. This procedure can be summarized as follows:

1. The heat transfer coefficient at stagnation is calculated suing Equation (6.14).

$$Nu_{o,w} = \frac{h_o w}{k_f} = 0.68\,\mathrm{Re}_w^{0.53}\,\mathrm{Pr}^{0.375} \tag{6.14}$$

2. The normalized local heat transfer coefficient λ_{eff} is calculated from Equation (6.15).

$$\frac{h_x}{h_o} = \lambda_{eff} = 0.4\lambda_1 + 0.6\lambda_2 \tag{6.15}$$

Where the two functions λ_1 and λ_2 are calculated form Equations (6.16) and (6.17).

$$\lambda_1 = [0.33\cdot\cos(0.5\pi\frac{x}{w}) + 0.67]\cdot e^{(-0.015\frac{x}{w})} \tag{6.16}$$

$$\lambda_2 = [0.25\cdot\sin(0.2\pi\frac{x}{w}) + 1]\cdot e^{(-0.148\frac{x}{w})} \tag{6.17}$$

3. The effect of bubble-generation enhancement on forced convection is introduced in the effective forced convection coefficient, h_{fc}, which is calculated using

Equation (6.18)

$$h_{fc} = \eta_{fc} \cdot h_x \tag{6.18}$$

Where the enhancement factor, η_{fc}, due to bubble generation has been modeled as a function of the bubble population intensity, N'', using Equation (6.19):

$$\eta_{fc} = \left(\frac{N''}{10^5} \right)^{0.15} \tag{6.19}$$

The enhancement factor is only used when the surface superheat is greater than or equal to the superheat corresponding to the onset of nucleate boiling, ΔT_{ONB}. ΔT_{ONB} is calculated using the model discussed in chapter 3 and presented here in Equation (6.20).

$$\Delta T_{ONB} = 10 \cdot \left(\frac{U_l}{V_n} \right)^{0.15} \cdot Ja_{sub}^{0.05} \cdot e^{(-0.014\frac{x}{w})} \tag{6.20}$$

Based on the value of h_{fc}, the transient conduction domination period, t_{TC}, is determined from Equation (6.11). As mentioned in the previous section, the determination of which temporal partitioning case should be used to represent the heat transfer process, both t_w and t_{cycle} must be determined and compared with the value of t_{TC}. According to Equation (3.13), the waiting period, t_w, is determined by calculating the growth time t_g and the bubble release frequency, f, using the constitutive sub- models of both t_g and f:

$$t_g = \frac{0.13 \cdot e^{(-0.002 \cdot \mathrm{Re}_w)}}{Ja_{\sup}^{1.07}} \tag{6.21}$$

$$f = (5.015x10^7) \frac{Ja_{\sup}^{1.82}}{\mathrm{Re}_w^{1.89}\, Ja_{sub}^{1.69}} \tag{6.22}$$

The most probable values of bubble population *N”* in addition to the bubble sliding distance, L_{slid}, have been calculated using the constitutive sub-models developed using the experimental data and discussed in chapter 3:

$$\begin{aligned} N'' = &-1.04786 \times 10^7 + 2339 \cdot \mathrm{Re}_w - 0.4306 \cdot \mathrm{Re}_w^2 + 260409 \cdot Ja_{sub} \\ &- 2520 \cdot Ja_{sub}^2 + 52291 \cdot Ja_{\sup} + 276.2 \cdot Ja_{\sup}^2 \end{aligned} \tag{6.23}$$

$$L_{slid} = 3D_b \tag{6.24}$$

The values of *N”* and L_{slid} are used to calculate the value of A_{tc} using Equation (6.4) or Equation (6.5), depending on the most probable bubble growth termination (BGT) scenario.

Level (2) of the energy cascade during JIB represents the heat used for phase change. Evaporation heat flux can be determined independently using Equation (6.25)

$$q_{ev}'' = fN'' \rho_v \frac{\pi}{6} D_b^3 h_{fg} \tag{6.25}$$

Consequently, since:

$$q_w'' = q_{fc}'' + q_{tc}'' = q_{liq}'' + q_{ev}'' \tag{6.26}$$

The amount of sensible heating of liquid is determined as:

$$q_{liq}'' = q_w'' - q_{ev}'' \tag{6.27}$$

6.6 Implementation procedure of the Present WFP Model

The following procedure summarizes the steps to determine the total wall heat flux using the present wall flux partitioning model. The present WFP model has been validated by comparing the results obtained using this procedure with the experimentally obtained heat flux values. Such validation is presented in the next section.

1- Define the input local values to the WFP model, which are: V_n, ΔT_{sub}, ΔT_{sup}, and *x*.

2- Calculate liquid properties at the average liquid film temperature, $T_f = (T_s + T_L)/2$. and vapor properties at T_{sat}. Calculate Re_w and local Ja_{sub} and Ja_{sup}.

3- Using Equation (3.6), determine X_{hj} and check if the location of interest, *x*, is upstream or downstream the hydraulic jump, if one was to appear on the heated length of interest (i.e., if X_{hj} is less than the heater length on one side of the jet.).

4- Using Equations (3.7) and (3.8), determine the liquid film thickness, δ, and the mean liquid velocity, U_l,.

5- Substitute Equations (6.15) and (6.19) into Equation (6.18) to calculate h_f

6- Determining the boiling onset superheat, ΔT_{ONB}. From Equation (3.9)

7- Compare ΔT_{ONB} with the local superheat, ΔT_{sup},. Consider the following cases:

a. If $\Delta T_{sup} < \Delta T_{ONB}$, heat transfer calculation will be due to single-phase forced convection heat transfer.

b. If at given location x, $\Delta T_{sup} \geq \Delta T_{ONB}$, then boiling onset has occurred, calculate D_b, N", f, t_g, t_w, and t_{TC} (Equation (6.11)). Determine the BGT scenario, and L_{slid} ,if bubbles would slide.

c. Calculate t_w, t_{cycle}, A_{tc}, A_{fc} (where $A_{fc}=1-A_{tc}$).

8- Compare t_{TC} with t_w and calculate $t_{cycle}=t_w+t_g$. Accordingly, determine the temporal partitioning case as per details presented in section 6.4. Determine which Equation of (6.12) or (6.13) should be used to estimate q''_w.

9- The fraction of the wall flux used for evaporation q''_{ev} and consequently the fraction used for liquid sensible heating q''_{liq} are determined from Equations (6.26) and (6.27), respectively.

The proposed WFP model can be used with either the surface superheat or the wall heat flux as an input to the model. The procedure described above assumes the local superheat to be known and the wall heat flux could be thus directly obtained. If the wall superheat is to be determined at given heat flux value the above procedure would be applied iteratively.

The closure of the present WFP model has been carried out using the constitutive sub-models developed for single-phase heat transfer and bubble dynamics, discussed in chapter 3, and using other closure relations that are presented in this chapter. The agreement with the physics of the JIB heat transfer process and the validation of the WFP model are presented later in this chapter. The model has been validated using the experimental data presented in chapter 3.

The model can be used to identify the location on the surface where the enthalpy of the fluid bulk exceeds that of the saturation. Starting at x=0, the procedure of calculating the local heat flux described above can be applied successively at downstream locations to calculate the incremental increase in the liquid enthalpy, assuming negligible losses at the free surface to the ambient air. It is postulated here that downstream the location where the liquid enthalpy reaches the saturation criterion, there would be net vapor generation in the flow. According to Zeitoun (1994), this location could be defined as the onset of significant void (OSV). In the current study, the identification of the OSV location and the corresponding wall superheat and heat flux under various cooling conditions have not been investigated. However, visual observation have revealed that for wide range of velocity and subcooling, bubbles generated near the heated surface edge, approximately at x/w>8, could slide for longer distances than proposed by Equation (6.24) towards the end of the heater length and would decay only after leaving the heated surface where the liquid bulk was not receiving energy anymore.

6.7 Model Verification

This section presents the verification of the present WFP model in terms of its ability to predict the expected trends of the various heat transfer mechanisms present in the case of JIB heat transfer. The predicted variation of the percentage primary heat flux partitions (i.e., the percentage forced convection (Q_fc%) and percentage transient conduction (Q_tc%) heat flux partitions) as a function of wall superheat is shown in Figure 6.3 for 3 cases: V_n=1.7 m/s, and ΔT_{sub}=22 °C, V_n= 1.7 m/s and ΔT_{sub}=10 °C, and V_n=0.75 m/s, ΔT_{sub}=22 °C at x/w =0, 4, and 8. For the same cases, Figure 6.4 illustrates the predicted variations of the percentage secondary heat flux partitions (i.e., the percentage evaporation heat flux (Q_ev%) and percentage sensible liquid heating flux (Q_liq%)) the sum of which represents 100% of the total heat transfer to the fluid bulk. From both Figures the following could be concluded on the predictions of the proposed WFP model:

The percentage of the wall heat flux transferred by forced convection, Q_fc%, is dominant at low superheat, approximately in all cases at ΔT_{sup}<10 °C only forced convection takes place at all locations. The value of Q_fc% then drops gradually as the fraction of the wall heat flux removed by transient conduction Q_tc% starts to increase with the onset of bubble generation. The model predicts slightly earlier onset at lower subcooling and that has been more obvious farther from the stagnation (e.g: about 2 °C).

The reduction in jet velocity allowed the escalation of the bubble dynamic role within narrower range of the wall superheat (e.g.: at x/w=0 the increase of Q_tc% to 4% occurred within 2 °C at the lower velocity as compared to 6 oC at the higher velocity). The WFP model was also able to capture the suppressing effect of jet impingement on bubble nucleation and bubble growth as evident from the almost flat profile of the Q_fc% at x/w=0 and the slight reduction at relatively high wall superheat. Such effect degraded with distance from stagnation and, subsequently, the contribution of transient conduction to the total wall heat flux has increased away from stagnation as evident by comparing the cases of V_n=1.7 m/s and ΔT_{sub}=22 °C at x/w=0 (Q_tc%~18% at ΔT_{sup}=24 °C) and x/w=8 (Q_tc%~45% at ΔT_{sup}=24 °C).

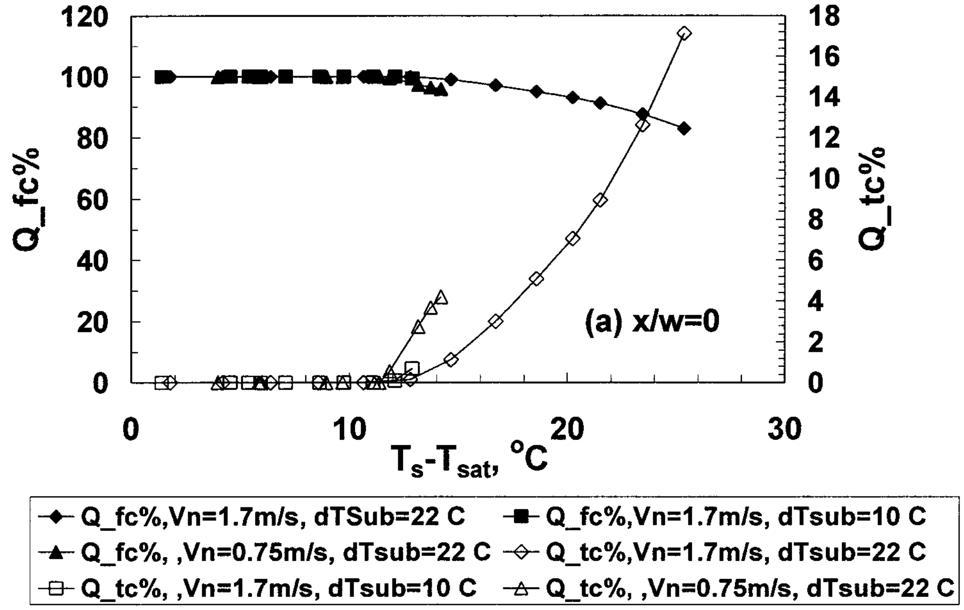

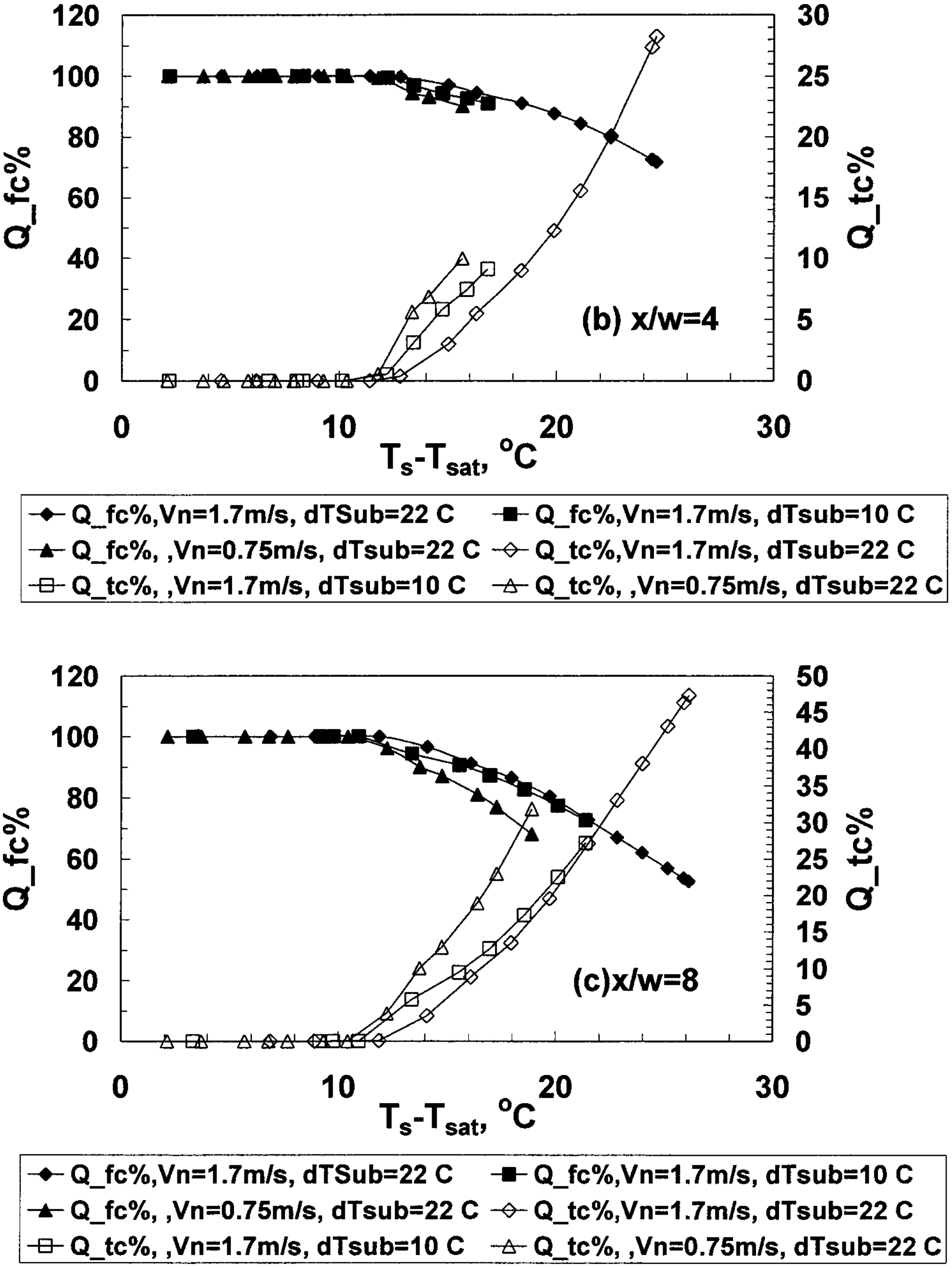

Figure 6. 3 Predicted variation of the primary heat flux partitions.

The predicted trends show on in Figure 6.4 indicate that as surface superheat increases, more liquid superheat is available for evaporation. In the vicinity of jet stagnation the original liquid subcooling is maintained such that sensible heating is dominant. As liquid temperature increases downstream of jet stagnation, it becomes more convenient for bubble growth, and hence more energy is utilized in phase change.

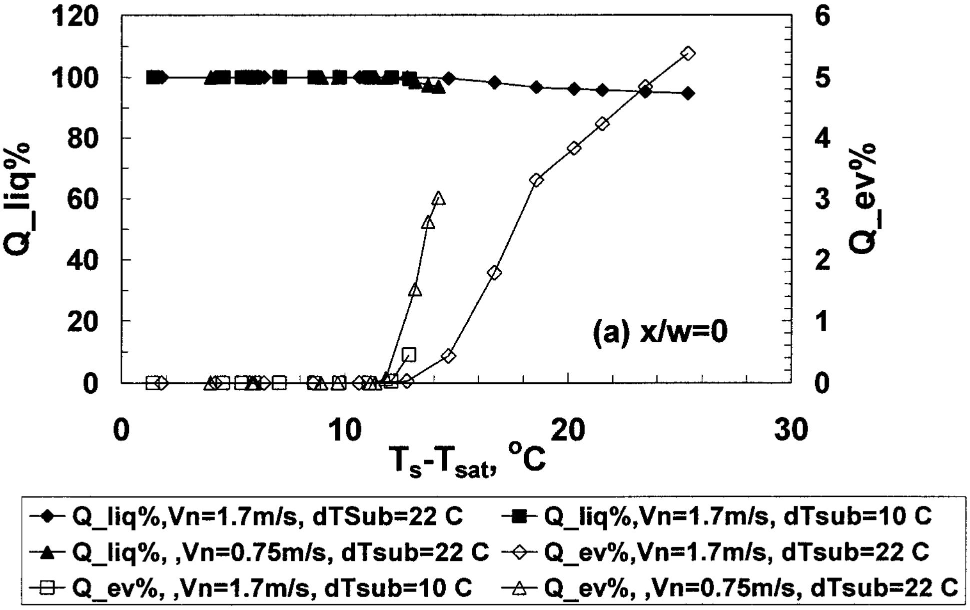

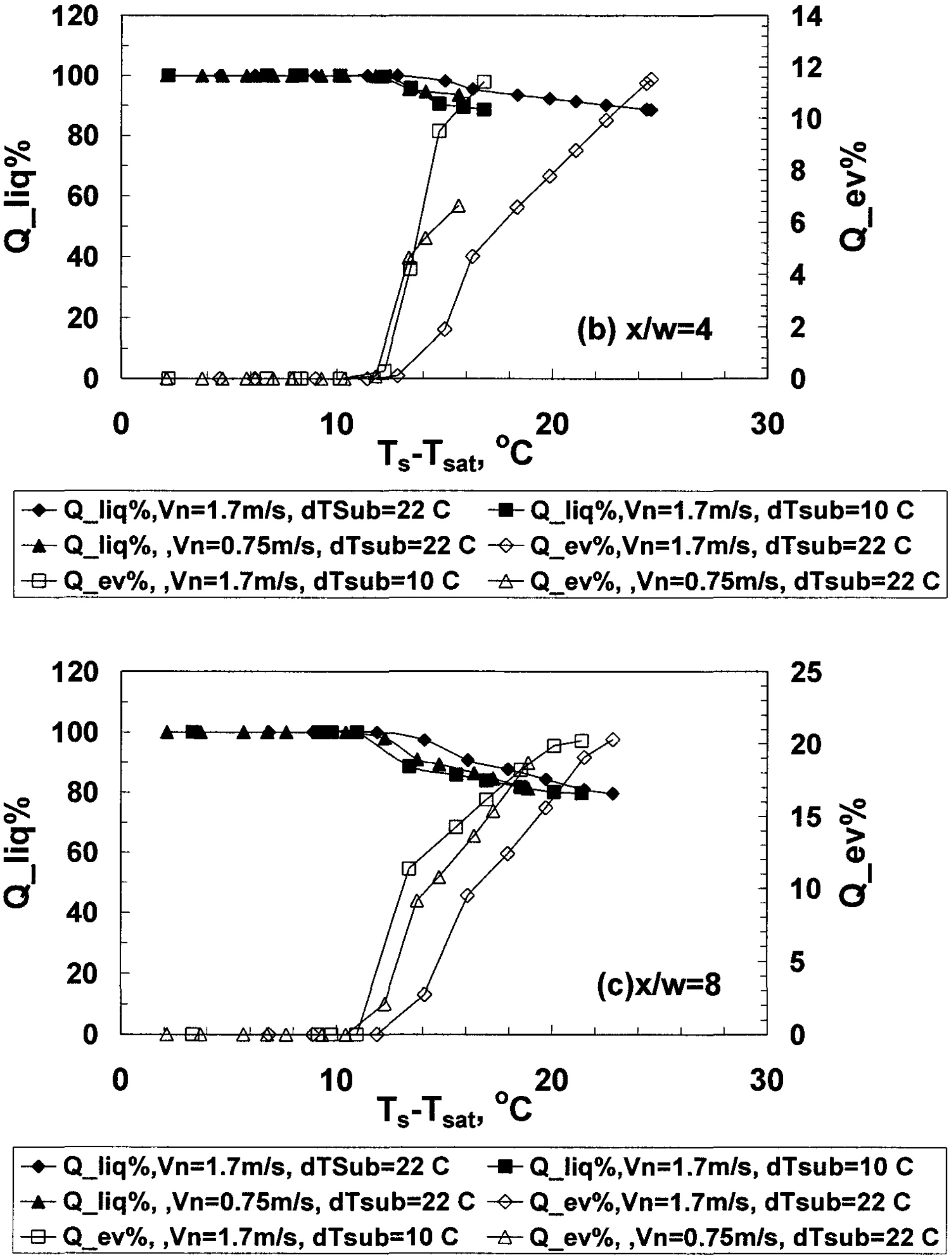

Figure 6. 4 Predicted variations of the secondary heat flux partitions.

At stagnation, the predicted contribution of evaporation (Q_ev%) is less than 5% of the total wall heat flux, while the remaining 95% is due to liquid heating. Slight increase is predicted in evaporation with the distance from stagnation as well as with reduction in jet velocity and or the liquid subcooling. Maximum share of evaporation heat transfer has been predicted for the lowest liquid subcooling and jet velocity at the farthest location (i.e. at x/w=8) where Q_ev% has slightly exceeded 20% at wall superheat around 21 °C. Average Q_ev% value however would remain around 10%.

Considering these results, it is evident that the present WFP model is capable of capturing the expected JIB physics and is capable of predicting the trends of various wall heat flux partitions and energy utilization in sensible heating and vapor generation under JIB conditions. Since no such analysis of the trends of various heat flux partitions has been found in available literature for JIB, in the following paragraphs, a discussion is presented on similar findings of Basu (2003) on these trends in PFB in vertical upward flow boiling. Figure 6.5 illustrates the trends of variation of the primary heat flux partitions for flow velocity at approximately 0.4 m/s, with the mass velocity G=346 kg/m^2.s and at 0.9 m/s, where G=868 kg/m^2.s. For both cases the degree of liquid subcooling at the inlet was maintained at 7.4 °C. Figure the percentage transient conduction. Figure 6.6 illustrates the corresponding trends in the secondary partitions for the same flow conditions. Comparing Figures 6.5a with 6.5b, it can be concluded that the increase in flow velocity has slightly suppressed the increase in transient conduction flux partition with the wall superheat, e.g.: at $\Delta T_W \sim 21$ °C, this partition was reduced to approximately 90% of the total wall heat flux at the higher velocity from close to 95% at the lower velocity. However this share of the transient conduction is much higher than the prediction of the WFP in JIB configuration. This could be attributed to the relatively higher value of the forced convection heat transfer coefficient in the JIB which ranged between twice to thrice the values reported by Basu (2003) in PFB configurations.

In Figure 6.6, the percentage of the heat flux that was utilized in evaporation has reached as high as 33% at wall superheat of 24 °C at the lower flow velocity. This share was limited to approximately 25% at the higher velocity. These values of the evaporation heat transfer are in agreement with the findings of the current study as discussed above.

It is expected from the findings of the current study and of the study of Basu (2003) that at higher jet velocity and with the forced convection heat transfer coefficient at much higher values in case of JIB than in case of PFB, that evaporation heat flux would be much less in the JIB configuration and hence the primary role that can be attributed to bubble growth in determining the overall heat transfer rate is the enhancement to single phase heat transfer either by forced convection or by transient conduction from the heated surface to the liquid bulk.

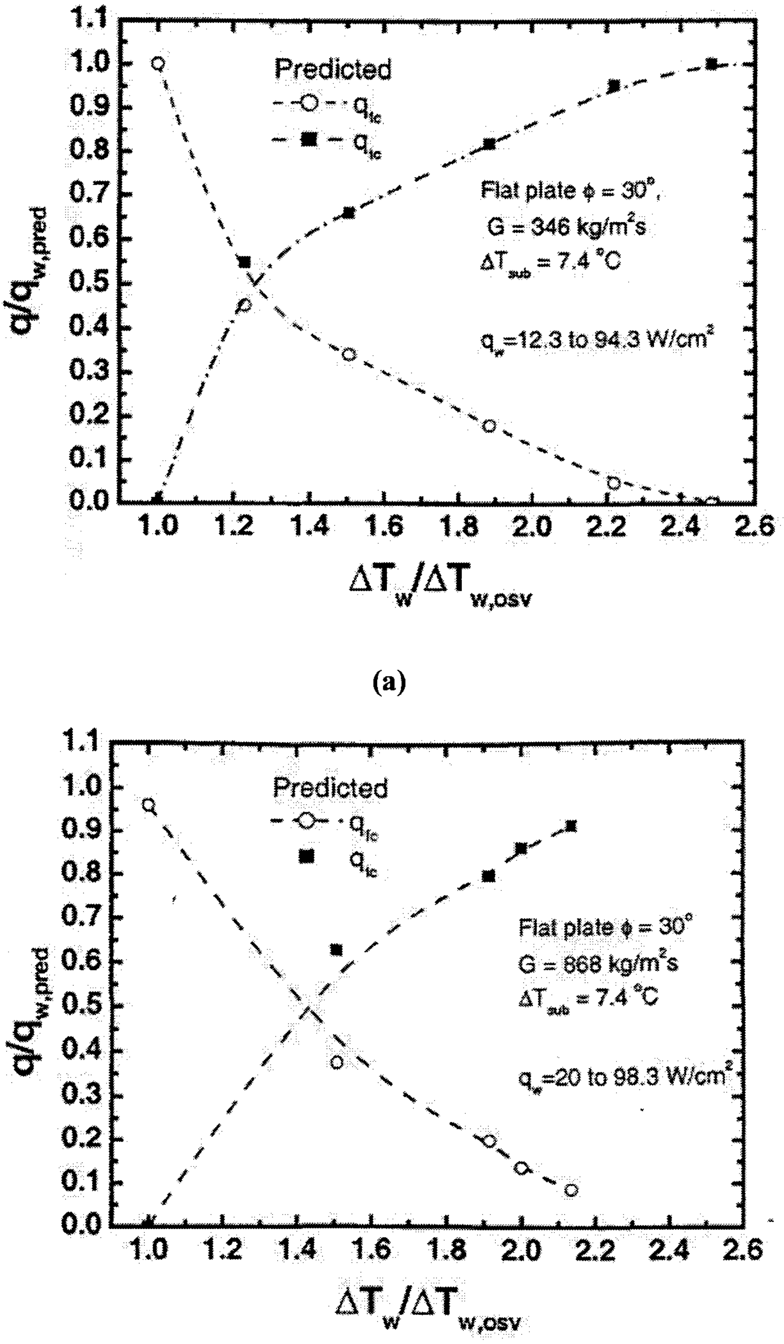

(a)

(b)

Figure 6. 5 Trends of primary heat flux partitions with wall superheat and flow velocity in PFB configuration, Basu (2003)

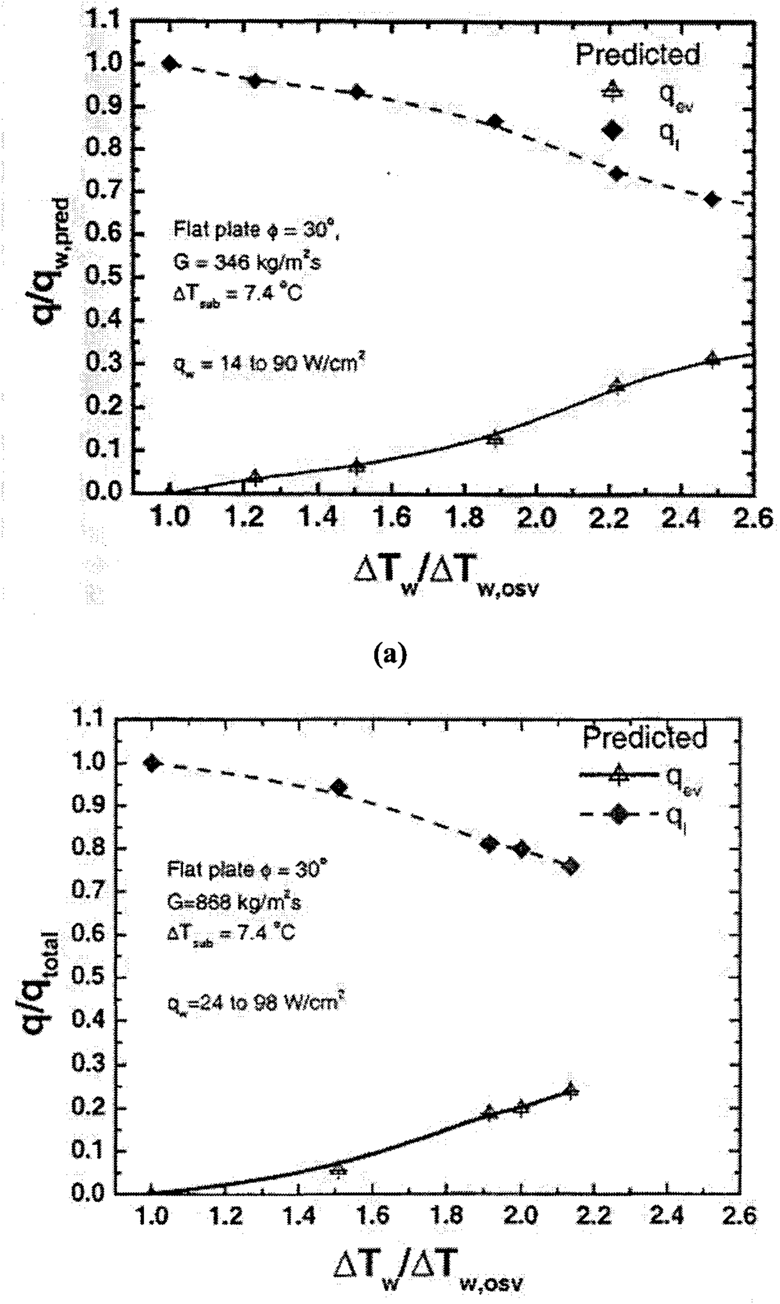

(a)

(b)

Figure 6. 6 Trends of secondary heat flux partitions with wall superheat and flow velocity in PFB configuration, Basu (2003)

6.8 WFP Model Validation

It is very important to assess the agreement between the WFP model predictions of the total wall heat flux and the corresponding experimental heat flux data presented in chapter 3. Figures 6.7 to 6.12 illustrates such agreement at various locations from stagnation, namely, at: x/w = 0, 2, 4, 6, 8, and 10. Considering a set of 150 data points that covers the entire experimental range considered in the current study, i.e., jet velocity from 0.4 m/s to 1.7 m/s, degree of subcooling from 10 °C to 28 °C, and wall temperature from 75 °C to 125 °C, the overall agreement between the experimental results and the predictions of the wall flux partitioning model is ± 30%. It is worthy to note that the agreement with this set of 150 points has been achieved using the constitutive closure submodels that have been developed using about 25 data points for bubble dynamics submodels and 50 points for the single-phase heat transfer coefficient model.

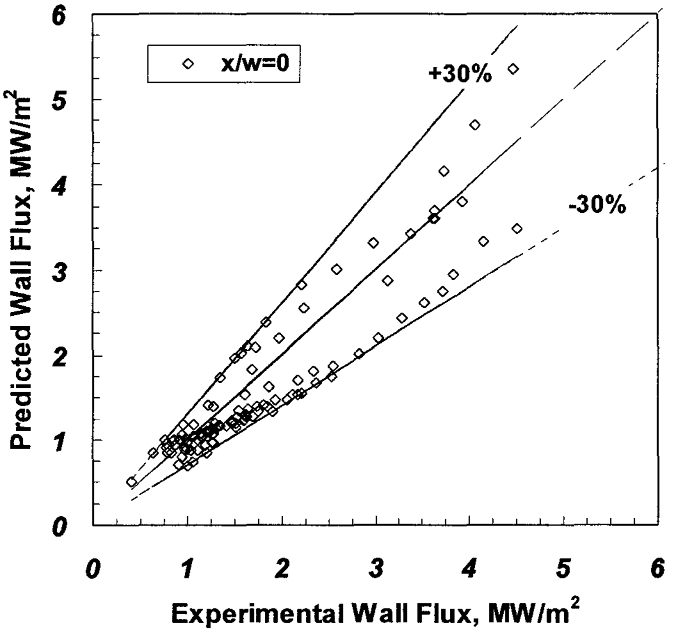

Figure 6. 7 Wall Flux Predictions at x/w=0

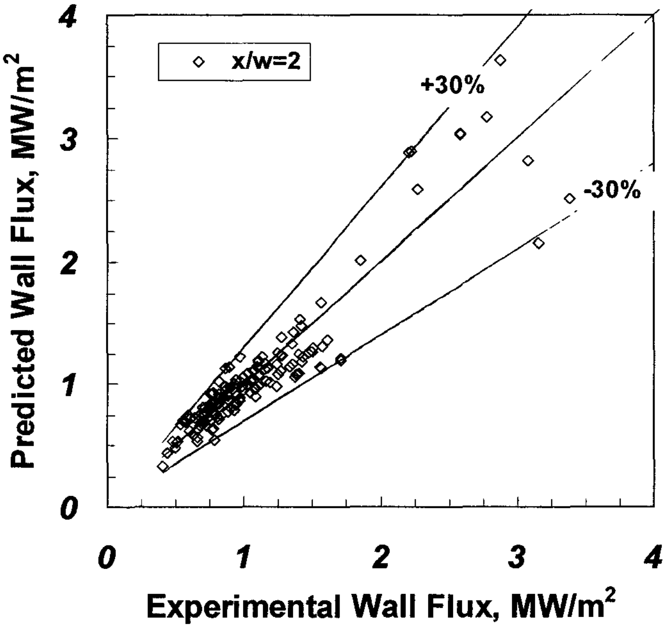

Figure 6. 8 Wall Flux Predictions at x/w=2

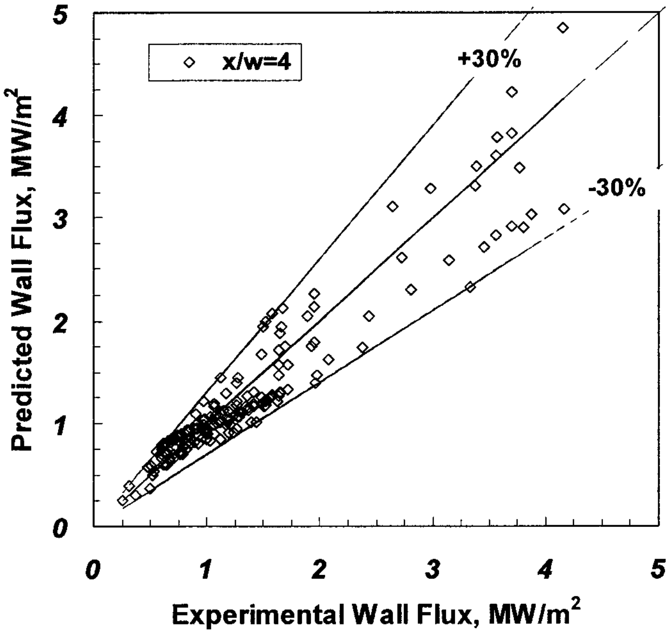

Figure 6. 9 Wall Flux Predictions at x/w = 4.

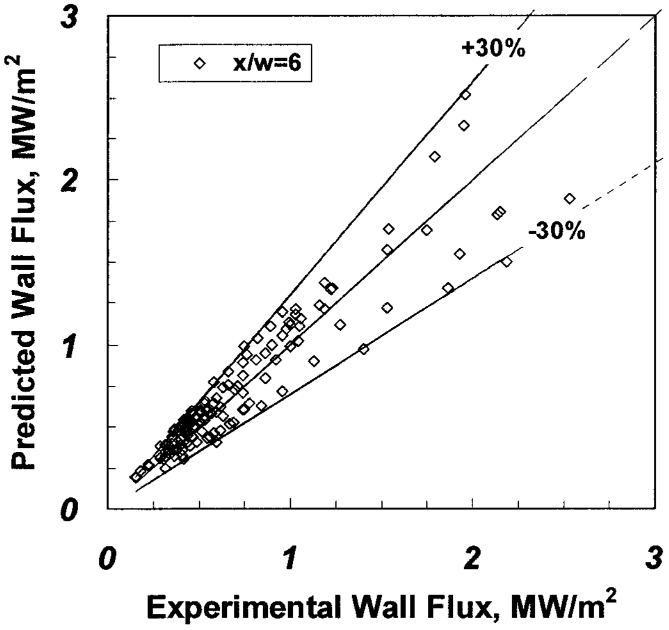

Figure 6. 10 Wall Flux Predictions at x/w = 6

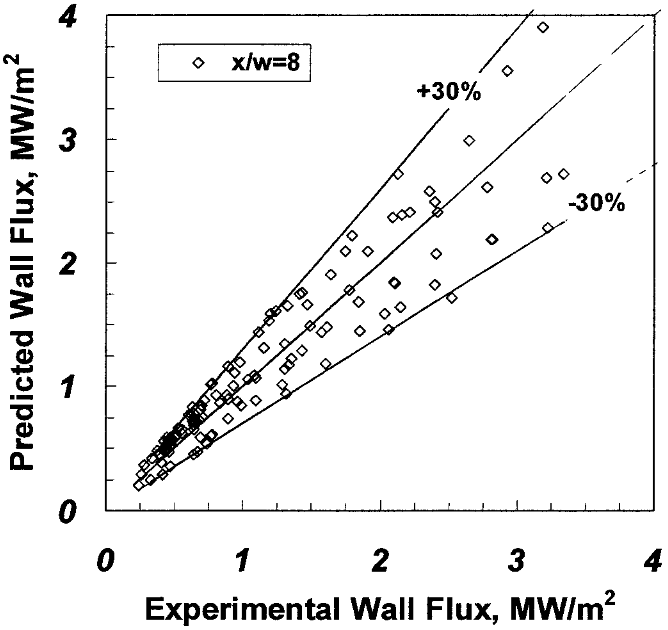

Figure 6. 11 Wall Flux Predictions at x/w = 8.

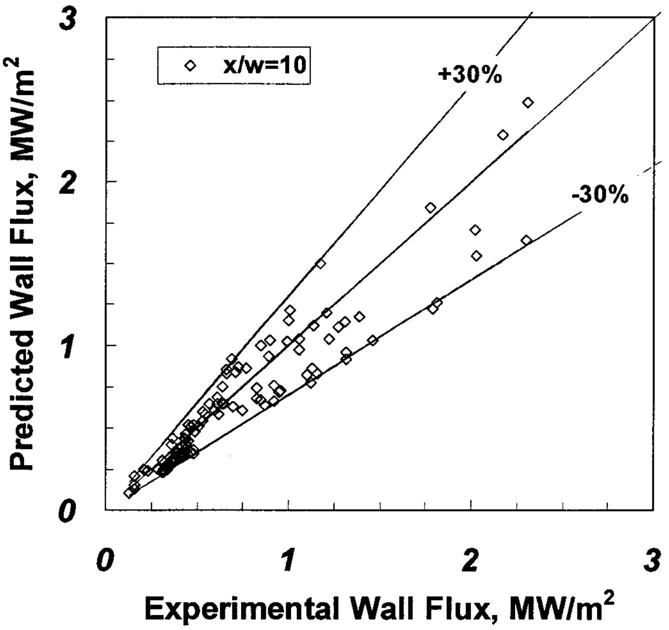

Figure 6. 12 Wall Flux Predictions at x/w = 10.

6.9 Effect of Flow Velocity and Subcooling on the WFP Model Predictions

This section is intended present a discussion on the individual effects of jet velocity and subcooling as well as the surface superheat on the response of the WFP model and hence the agreement between its predictions and the experimentally obtained values of the wall heat flux. These separate effects are important to understand and to determine the limitations of the proposed model in its current state and so future improvements in the measurement techniques and/or in the analysis and development approaches of the closure submodels can alleviate such limitations.

In Figure 6.13, three cases have been used to discuss these effects where variation in agreement with the velocity is illustrated at two levels of jet velocity.

In all the three figures, the plot of the fraction of each of the primary heat flux partitions was aimed to highlight that nucleation has been predicted by the WFP model over the range of interest of the wall superheat. This will help understanding the response with each of the velocity and liquid subcooling in the range of the boiling curve where the bubble dynamics rule is to be considered. The dashed lines on the figures represent the slope of the experimental boiling curve in this range of interest.

6.9.1 Effect of jet velocity

By Comparing Figures 6.13a and 6.13b, it is concluded that the model response to jet velocity is sound both in predicting the fraction of the single phase heat transfer fraction where higher values where maintained at the higher velocity level and also the increase in the slope which represents the model predictions of the additional effect of the bubble dynamics were well in agreement with the experimental slopes. The fluctuation between underestimation and overestimation are attributed to the inherent levels of uncertainty of the submodels which was presented in chapter 3.

6.9.2 Effect of liquid subcooling:

Contrary to the aforementioned response of the WFP model to changes in jet velocity, the increase in experimental boiling curve slope when the degree of subcooling was reduced from 22 °C to 10 °C was not well captured by the model when comparing Figures 6.13b and 6.13c. The model sensitivity to changes in subcooling is lower as evident from comparing the share of transient conduction between the two cases where it remained almost the same at given wall heat flux, e.g.: Q_tc%~ 2% at 15 °C superheat. Since the submodel of the forced convection heat transfer coefficient is slightly sensitive to liquid subcooling, it is postulated here that further improvement could be applied to the proposed bubble dynamics submodels to improve the sensitivity of the WFP model to changes in subcooling.

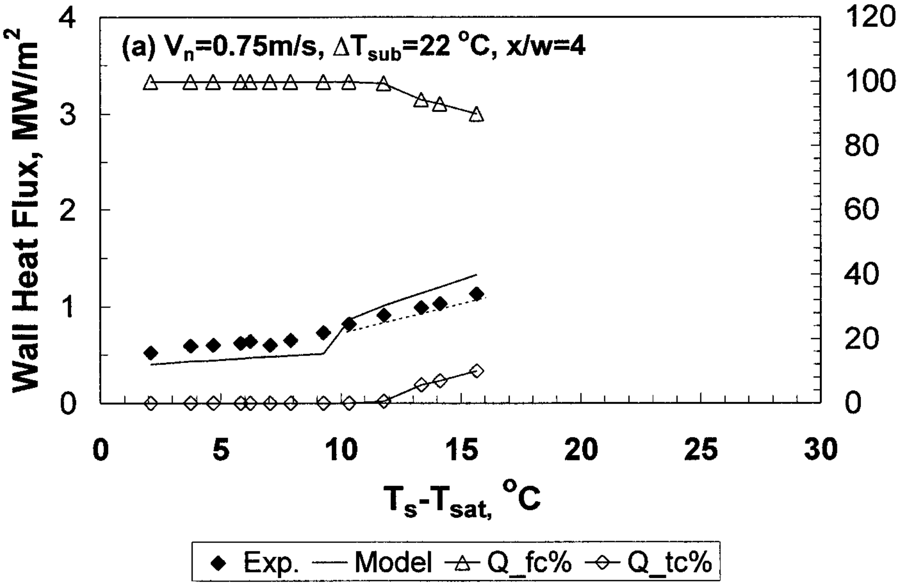
(a) V_n=0.75m/s, ΔT_{sub}=22 °C, x/w=4
Wall Heat Flux, MW/m^2
0
1
2
3
4
Q_fc%, Q_tc%
0
20
40
60
80
100
120
0
5
10
15
20
25
30
T_s-T_{sat}, °C
◆ Exp.
— Model
-△- Q_fc%
-◇- Q_tc%

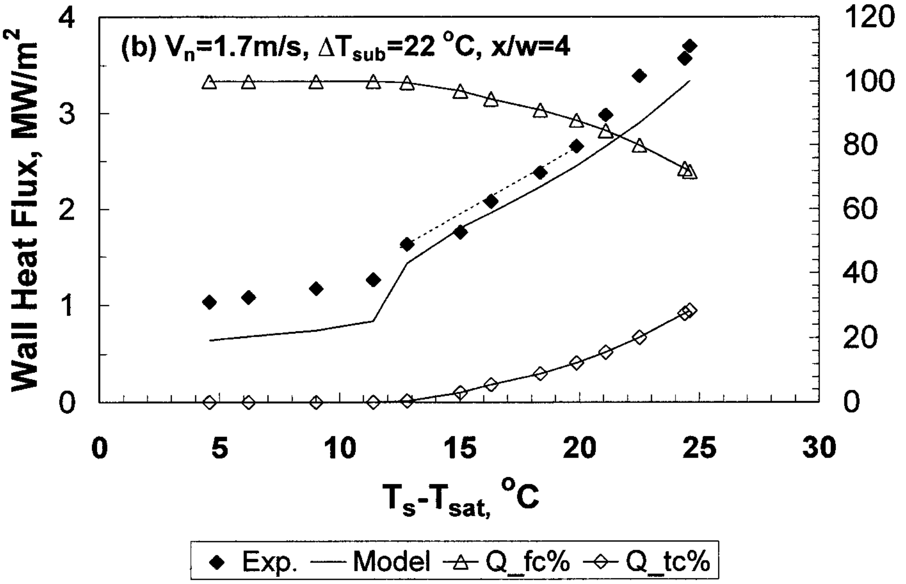
(b) V_n=1.7m/s, ΔT_{sub}=22 °C, x/w=4
Wall Heat Flux, MW/m^2
0
1
2
3
4
Q_fc%, Q_tc%
0
20
40
60
80
100
120
0
5
10
15
20
25
30
T_s-T_{sat}, °C
◆ Exp.
— Model
-△- Q_fc%
-◇- Q_tc%

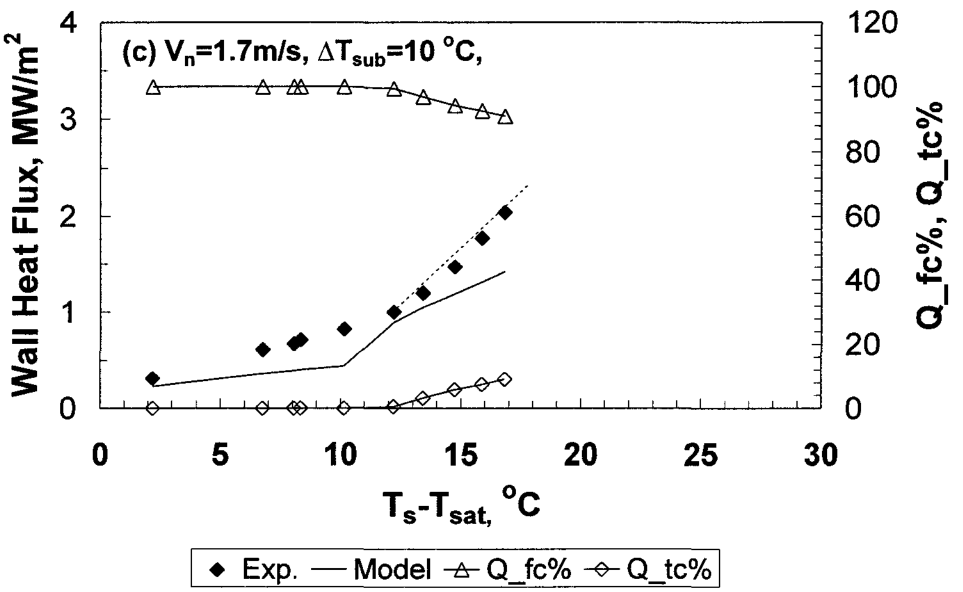

Figure 6. 13 Effect of jet velocity and subcooling on WFP model agreement

It is postulated here that bubble release frequency and bubble population submodels could be the major contributors to the shown deviations in the heat flux due to their relatively large uncertainty level and also due to the limitation of the current measurements where bubble population was obtainable over partial range of the wall superheat and at relatively high subcooling to allow for the identification of individual bubbles. Also, it is noteworthy that with the use of intrusive measurements being in its infancy, where the current study is the second of its kind to implement this technique in JIB investigations, there is further work that needs to be done towards the method of probe preparation and signal analysis to obtain better representation of the bubble release frequency and growth time during JIB.

Chapter 7

Summary, Conclusions and Recommendations for Future Work

7.1 Summary

Jet impingement boiling (JIB) heat transfer under a free water jet impinging on a flat surface kept at atmospheric pressure has been investigated experimentally. The effect of wall superheat, jet velocity, and liquid subcooling, on JIB heat transfer has been considered.

The current study presents three models that have been developed for the prediction of the total wall heat flux as a function of the flow conditions, surface temperature and the associated variation in nucleate boiling bubble dynamics.

The first model is an analytical/empirical global model that has been developed to address the effect of bubble dynamics on wall heat flux at jet stagnation. The model has been developed using an effective diffusivity similar to the concept of eddy diffusivity used in turbulence modeling. The effective diffusivity is the sum of an additional bubble-induced diffusivity (BID) that accounts for the effect of bubble protrusion into liquid flow bulk and the molecular diffusivities. The effective diffusivity has been introduced in the diffusion terms of the momentum and energy conservation Equations. It has been modeled as a function of the flow velocity, subcooling and surface superheat using the bubble diameter as a characteristic length.

The second model is a scenario identification procedure (SIP) that has been developed for the identification of the mechanism governing the bubble growth termination (BGT) process. The developed SIP determines which equilibrium condition, the thermal or the dynamic, is fulfilled first by the growing bubble. Accordingly, the SIP determines the corresponding BGT scenario. The SIP thus allows for improved determination of the area of influence of the various heat transfer mechanisms that considers possibility of occurrence of various BGT scenarios over a wide range of flow velocity, subcooling and surface temperature. The developed SIP accounts for the effect of bubble protrusion into the subcooled liquid layer and the effect of any abrupt increase in the liquid film thickness downstream of jet stagnation due to hydraulic jumps.

The third model is a mechanistic model that has been developed to predict the wall heat flux distribution along the heated surface from the stagnation point up to ten times the jet width. The model has been developed using the wall flux partitioning (WFP) concept. Boiling Reversed Energy Cascade (BREC) has been proposed and used in this model to describe the sequence of primary and secondary heat transfer mechanisms from the heated surface to the liquid bulk. It has been postulated that the wall heat flux is primarily due to forced convection and transient conduction and that the existence of a superheated liquid layer in the vicinity of the heated surface is the sole factor that assists bubble growth wherever active nucleation sites exist. The closure of the wall flux partitioning model has been carried out by introducing a set of constitutive sub-models of the spatial distribution of single-phase heat transfer, liquid film thickness, boiling onset surface superheat, maximum bubble diameter, bubble population area density, bubble release frequency and bubble growth time.

The model of the SIP has been utilized to determine the BGT scenario, i.e., whether BGT is associated with a local collapse or with a departure and sliding. The most probable BGT scenario has been used to determine the area of influence of each of the primary heat transfer mechanisms, as well as to independently quantify the rate of evaporation heat transfer.

The development and validation of these three models have been carried out using experimental data. A set of experiments has been conducted to study jet impingement boiling heat transfer and the associated characteristics of bubble dynamics under a planar water jet considering both the single-phase and nucleate boiling regimes. The data covered in the experimental study have been obtained considering the following range of flow conditions, surface temperature and locations from the jet stagnation:

1. Jet velocity, V_n=0.4-1.7 m/s.

2. Water Subcooling ΔT_{sub}= 10-28 °C.
3. Wall superheat, ΔT_{sup}-= 25-30 °C.
4. Distance from stagnation point with respect to jet width, x/w, = 0-10.

Investigations of single-phase heat transfer in the above range of x/w showed that secondary peaks exist downstream of heat transfer coefficient exist at the stagnation around x/w=4 and to a less extent at x/w=8. These variations of the heat transfer coefficient are likely attributed to cyclic changes in the flow velocity direction downstream the jet stagnation before it becomes parallel to the heated surface. A generalized heat transfer coefficient model which captures the variations for all examined locations along the heated surface has been developed. This has been achieved by developing a shape factor that consists of two trigonometric functions to relate the value of the heat transfer coefficient at downstream locations to that at the stagnation.

In the wall flux partitioning model, an empirical submodel has been proposed to address the effect of bubble generation density on the single phase heat transfer coefficient in the nucleate boiling regime. The expected bubble-induced improvement has been modeled in term of the bubble population intensity. The proposed submodel is applicable for partial and fully developed nucleate boiling.

The characteristics of bubble dynamics have been investigated using intrusive optical probe in addition to non-intrusive high speed imaging technique. Jet velocity and degree of liquid subcooling have, in general, a suppressive effect on the onset of bubble generation and bubble growth. However, wall superheat has a promoting effect that assisted in extending bubble growth to larger diameters, activating larger number of nucleation sites and increasing bubble growth rate. Experimental observations showed that, over the range of flow velocity, water subcooling and surface superheat considered in this study, bubble growth rate is strongly impacted by the wall superheat, and to much less extent by the jet velocity. The waiting time has been obtained from the measured growth time and release frequency. The waiting time has been generally one order of magnitude higher than the growth time, which supported the assumption that primary heat transfer mechanism in jet impingement boiling is basically due to sensible heating of liquid, while evaporation represents a promoting factor rather than a primary heat transfer mechanism.

7.2 Conclusions

- Comparison with experimental data showed that the bubble induced diffusion (BID) analytical/empirical model is in agreement within -15% and +30% with the experimental data of stagnation heat flux.
- The Bubble Growth Termination Scenario Identification Procedure (BGT-SIP) has predicted the correct scenario of bubble growth termination (BGT) observed experimentally in about 80% of the investigated cases.

- The wall flux partitioning model has shown an overall agreement of ±30% of the experimental heat flux data for range of distance, x from jet stagnation between $0 < x/w < 10$, where w is the jet width.

7.3 Recommendations for Future Work

Future work should be directed towards improvement of the proposed submodels as follows:

- The use of a higher number of frames per seconds, e.g., 5000 frames/s, is highly recommended in order to obtain more details of the growth history of individual bubbles and to improve the prediction of the maximum bubble diameter, as well as the sliding distance, whenever bubble departure takes place.
- An extension to the current study in the direction of investigating the effect of other surface conditions, such as surface roughness and surface material on the nucleation process could improve the predictability of the wall heat flux models for various types of commercial surfaces.
- Further research could be directed towards the investigation of the effect of surface curvature on the spatial variation of heat transfer rate and bubble dynamics under liquid jet impingement. This could include the investigation of jet impingement heat transfer on concave and convex surfaces with various radii of curvature.

- As some industrial applications may not be using water for cooling, the effect of changing the type of liquid could be investigated under jet impingement conditions. For example, considering their superior thermal properties, the use of nano fluid jets could be of interest.

REFERENCES

Bartoli, C., Di Marco, P. and Faggiani, S. 1997, "Heat Transfer And Flow Pattern At A Cylinder Impinged By A Slot Jet During Incipient And Nucleate Boiling", Experimental Thermal and Fluid Science, Vol. 15, n. 2, pp. 101-108.

Basu, N. 2003, "Modeling and Experiments for Wall Heat Flux Partitioning During Subcooled Flow Boiling of Water at Low Pressures", PhD Thesis, University of California, Los Angeles.

Basu, N., Warrier, G. and Dhir, V.K. 2002, "Wall Heat Flux Partitioning During Flow Boiling: Part I:-Model Development", J. of Heat Transfer, Vol. 127, pp. 131:140.

Basu, N., Warrier, G. and Dhir, V.K. 2005, "Onset of Nucleate Boiling and Active Site Density During Subcooled Flow Boiling", J. of Heat Transfer, Vol. 124, pp. 717:728.

Bogdanic, L., Auracher, H. and Ziegler, F. 2007, "Two-Phase Structure above Hot Surfaces in Jet Impingement Boiling, International Journal of Heat and Mass Transfer", Special Issue.

Carey, V.P. 1992, "Liquid-Vapor Phase-Change Phenomena", Series in Chemical and Mechanical Engineering, Publisher: Taylor& Francis.

Chang H., Lienhard J. H.(V), Younis, H.F., Dahbura, R. S., and Michels D. 1998, "Liquid Jet-Array Cooling Modules For High Heat Fluxes", AIChE Journal, Vol. 44, n 4, pp. 769:779.

Chang, Y. P. 1956, "A Theoretical Analysis of Heat Transfer in Natural Convection and in Boiling", ASME-HTD, presented at the Power Division Annual Meeting, 1956, pp. 1501:1513.
Dhir, V. K., Abarajith, H. S. and Li, D. 2007, "Bubble Dynamics And Heat Transfer During Pool And Flow Boiling", Heat Transfer Engineering, Vol. 28, n 7, pp. 608-624.

Dukle, N.M. and Hollingsworth, D.K. 1996, " Liquid Crystal Images of the

Transition from Jet Impingement Convection to Nucleate Boiling. Part II: Non-monotonic Distribution of the Convection Coefficient", Experimental Thermal and Fluid Science, Vol. 12, n. 3, pp. 288-297.

Ferret, C., Falk, L., D'Ortona, U., Chenu, A. and Veenstra, T.T. 2004, " Introduction of Image Analysis for the Quantification of the Boiling Flow Heat Transfer", Chemical Engineering Journal, Vol. 101, pp. 357:365.

Hahne, E., Barthau, G., 2006, "Heat Transfer and Nucleation in Pool Boiling", Int. J. Thermal Sciences, Vol. 45, pp. 209-216.

Hammad, J., Mitsutake, Y. and Monde, M. 2004, "Movement of Maximum Heat Flux and Wetting Front During Quenching Of Hot Cylindrical Block", Int. J. Thermal Sciences, Vol. 43, pp.743:752.

Hsu, Y.Y. 1962, "On the Size Range of Active Nucleation Cavities on a Heating Surface", J. of Heat Transfer, Vol. 84, p.207.

Incropera, F.P. and DeWitt, D.P. 1996, "Introduction to Heat Transfer", 3rd edition, Publisher: John Wiley & Sons.

Ishigai, S., Nakanishi, S. and Ochi, T. 1978, "Boiling Heat Transfer for a Plane Water Jet Impinging on a Hot Surface", 6th International Heat Transfer Conference, Toronto, Canada, pp. 445:450.

Judd, R.L. and Hwang, K.S. 1976, "Comprehensive Model for Nucleate Pool Boiling Heat Transfer Including Microlayer Evaporation", J. of Heat Transfer, Vol. 98, Sr. c, n. 4, pp. 623-629.

Kandula, M. 1990, "Mechanisms And Predictions Of Burnout In Flow Boiling Over Heated Surfaces With An Impinging Jet", Int. J. Heat and Mass Transfer, Vol. 33, n.9, pp. 1795:1803.

Kataoka, I., Uchida, K. and Matsumoto, T. 1999, " Simulation of Turbulence Induced by Bubble Growth and Collapse in Forced Convective Boiling", PVP-Vol. 397-1, Computational Technologies for Fluid/Thermal/Structural/Chemical Systems with Industrial Applications- Vol. 1, ASME, pp. 157:164.

Katto, Y. and Shimizu, M. 1979, “Upper Limit Of CHF In Saturated Forced Convection Boiling On A Heated Disk With A Small Impinging Jet”, J. Heat Transfer, Vol. 101, pp. 265:269.

Katto, Y. and Shimizu, M. 1979, “Upper Limit Of CHF In The Saturated Forced Convection Boiling On A Heated Disk With A Small Impinging Jet”, Trans. of ASME. J. of Heat Transfer, Vol. 101, n 2, pp. 265:269.

Katto, Y. and Yokoya, S. 1988, “Critical Heat Flux on a Disk Heater Cooled by a Circular Jet of Saturated Liquid Impinging at the Center”, Int. J. of Heat and Mass Transfer, Vol.31, n.2, pp. 219-227.

Klausner, J.F., Mei, R., Bernhard, D.M. and Zeng, L.Z.1993, “Vapour Bubble Departure in Forced Convection Boiling”, Int. J Heat and Mass Transfer, Vol. 36, pp. 651-662.

Koumoutsos, N., Moissis, R. and Spyridonos, A. 1968, “A Study of Bubble Departure in Forced Convection Boiling”, J. of Heat Transfer, Vol. 90, pp. 223-230.

Lahey Jr., R.T. 1978, “A Mechanistic Subcooled Boiling Model”, 6th International Heat Transfer Conference, Toronto, Canada, pp. 293:297.

Lienhard (V) J.H. 1995, “Liquid Jet Impingement”, Annual Review of Heat Transfer, Vol. 6, Chapter 4, pp. 199-270.

Liu, X. and Lienhard (V), J.H. 1993, “The Hydraulic Jump in Circular Jet Impingement and in Other Thin Liquid Films”, Experiments in Fluids, Vol.15, pp. 108-116.

Liu, Z. and Wang, J. 2001, “Study On Film Boiling Heat Transfer For Water Jet Impinging On High Temperature Flat Plate”, Int. J. Heat and Mass Transfer, Vol. 44, pp. 2475:2481.

Liu, Z.D., Fraser, D., Samarasekera, I.V. and Lockhart, G.T. 2002, “Experimental Observations And Modelling Of Thermal History Within A Steel Plate During Water Jet Impingement”, Canadian Metallurgical Quarterly, Vol. 41, n. 1, pp. 75:86.

Ma, C.F. and Bergles, A.E. 1986, "Jet Impingement Nucleate Boiling, Int. J. of Heat and Mass Transfer, Vol.29, n.8, pp. 1095:1101.

Mat, M., Kaplan, Y. and Ilegbusi, O. 1999, "Application of A Bubble-Induced Turbulence Model to Subcooled Boiling in a Vertical Pipe", MD-Vol.89, The Science, Automation, and Control of Material Processes Involving Coupled Transport and Rehology Changes, ASME.

Maurus, R., Ilchenko, V. and Sattelmayer, T., " Study of the Bubble Characteristics and the Local Void Fraction in Subcooled Flow Boiling Using Digital Imaging and Analysis Techniques", Experimental Thermal and Fluid Science, Vol. 26, pp. 147:155.

Mikic, B.B., Rohsenow, W.M. and Griffith, P. 1970, "On Bubble Growth Rates", Int. J. Heat and Mass Transfer, Vol. 13, pp. 657-666.

Mikielewicz, J., Mikielewicz, D. and Barnik, D. 2007, "Modeling of Nucleate Boiling Heat Transfer in a Film Formed by an Impingement Jet", Heat Transfer Research, Vol. 38, n. 4, pp. 313-323.

Mitsutake, Y. and Monde, M. 2001, "Heat Transfer During Transient Cooling Of High Temperature Surface With An Impinging Jet", Int. J. Heat and Mass Transfer, Vol. 37, pp. 321:328.

Moffat, R.J., 1985, "Using uncertainty analysis in the planning of an experiment", J. of Fluids Engineering, Vol.107, pp.173–178.

Monde, M. and Katto, Y. 1978, "Burnout In A High Heat-Flux Boiling System With An Impinging Jet", Int. J. of Heat and Mass Transfer, Vol. 21, n 3, pp. 295-305.

Monde, M., and Okuma, Y. 1985, "Critical Heat Flux In Saturated Forced Convective Boiling On A Heated Disk With An Impinging Jet: CHF In L-Regime", Int. J. Heat and Mass Transfer, Vol. 28, n. 3: pp. 547:552.

Montout, M., Haynes, P. and Colin, C. 2007, "Bubble Diameter Models at a Heated Wall for Subcooled Boiling Flow and Numerical CFD Simulations of the Impact of the Bubbles Sliding on the Heat Flux Repartition", Proc. 6th Int. Conference on Multiphase Flow, ICMF 2007, Leipzig, Germany, July 9-13, 2007, S5_Mon_C_9.

Mozumder, A.K., Monde, M. and Woodfield, P.L. 2005, "Delay Of Wetting Propagation During Jet Impingement Quenching For A High Temperature Surface", Int. J. Heat and Mass Transfer, Vol. 48, n.25-26, pp.5395-5407.

Munson, B., Young, D. and Okishi, T. 1990, "Fundamentals of Fluid Mechanics", Publisher: John Wiley and Sons.

Narumanchi, S., Troshko, A., Bharathan, D. and Hassani, V. 2008, "Numerical Simulations of Nucleate Boiling in Impinging Jets: Applications in Power Electronic Cooling", Int. J. of Heat and Mass Transfer, Vol.51, n. 1-2, pp. 1-12.

Omar A.M.T., Hamed, M.S. and Shoukri M. 2009, "Modeling of Nucleate Boiling Heat Transfer Under An Impinging Free Jet", Int. J. Heat and Mass Transfer, Vol. 52, pp. 5557-5566.

Petrovic, S., Robinson, T., Judd, R.L., 2004, " Marangoni Heat Transfer in Subcooled Nucleate Pool Boiling", Int. J. Heat and Mass Transfer, Vol. 47, pp. 5115-5128.

Podowski, R.M., Drew, D.A, Lahey Jr., R.T. and Podowski, M.Z. 1997, "A Mechanistic Model of The Ebullition Cycle in Forced Convection Subcooled Boiling", 8th International Topical Meeting on Nuclear Reactor Thermal-Hydraulics (NURETH-8), Koyoto-Japan, Sept. 30-Oct. 4, pp. 1535-1542.

Qiu, Y. and Liu, Z. 2005, "Critical Heat Flux Of Steady Boiling For Saturated Liquids Jet Impinging On The Stagnation Zone", Int. J. Heat and Mass Transfer, Vol. 48, n. 21-22, pp. 4590:4597.

Robidou, H., Auracher,H., Gardin, P., Lebouch, M. and Bogdanic, L. 2003, "Local Heat Transfer From A Hot Plate To A Water Jet", Int. J. Heat and Mass Transfer, Vol. 39, pp. 861:867.

Robidou, H., Hein Auracher, H., Gardin, P., and Lebouch, M. 2002, "Controlled Cooling Of A Hot Plate With A Water Jet", Experimental Thermal Sciences, Vol. 26, pp.123:129.

Rohsenow W., Hartnett J., and Cho Y., 1998, "The Handbook of Heat Transfer", 3rd edition, McGraw Hill.

Schafer D., Incropera F. P. and Ramadhyani, S. 1991, "Planar liquid jet impingement cooling of multiple discrete heat sources", J. of Electronic Packaging, Vol. 113, n. 4, pp. 359-366.

Seiler-Marie, N., Seiler, J. and Simonin, O. 2004," Transition Boiling At Jet Impingement", Int. J. Heat and Mass Transfer, Vol. 47, pp. 5059:5070.

Sernas, V. and Hooper, F.C. 1969, "The Initial Vapor Bubble Growth on a Heated Wall During Nucleate Boiling", Int. J. Heat and Mass Transfer, Vol. 12, pp. 1627:1639.

Shoukri M., Judd, R.L., 1978, " On the Influence of Surface Conditions in Nucleate Boiling- The Concept of Bubble Flux Density", J. Heat Transfer, Vol. 100, n. 4, pp. 618-623.

Situ, R., Mi, Y., Ishii, M. and Mori, M. 2004, " Photographic Study of Bubble Behaviours in Forced Convection Subcooled Boiling", Int. J. of Heat and Mass Transfer, Vol. 47, pp. 3659:3667.

Steiner, H., Kobor, A. and Gebhard, L. 2005, "A Wall Heat Transfer Model for Subcooled Boiling Flow", Int. J. of Heat and Mass Transfer, Vol. 48, pp. 4161-4173.

Timm, W., Weinzierl, K. and Leipertz, A. 2003, "Heat Transfer in Subcooled Jet Impingement Boiling at High Wall Temperature", Int. J. of Heat and Mass Transfer, Vol. 46, pp. 1385:1393.

Unal, H.C. 1976, "Maximum Bubble Diameter, Maximum Bubble-Growth Time and Bubble-Growth Rate During The Subcooled Nucleate Flow Boiling of Water Up to 17.7 MN/m2", Int. J. of Heat and Mass Transfer, Vol.19, pp. 643-648.

Vader, D.T., Incropera, F.P. and Viskanta, R. 1991, "Local Convective Heat Transfer From A Heated Surface To An Impinging, Planar Jet Of Water", Int. J. Heat and Mass Transfer, Vol. 34, n. 3, pp. 611:623.

Vader, D.T., Incropera, F.P. and Viskanta, R. 1992, "Convective Nucleate Boiling On A Heated Surface Cooled By An Impinging, Planar Jet Of Water", J. of Heat Transfer, Transaction of the ASME, Vol. 114, pp. 152:160.

Vandervort, C.L., Bergles, A.E. and Jensen, M.K. 1992, "Heat Transfer Mechanisms in Very High Heat Flux Subcooled Boiling", ASME Trans., HTD-

Vol. 217, Fundamentals of Subcooled Flow Boiling, pp. 1-9.

Wang, D., Yu, E. and Przekwas, A. 1999, "A Computational Study Of Two Phase Jet Impingement Cooling Of An Electronic Chip", 5th Annual IEEE Semiconductor Thermal Measurement and Management Symposium (Cat. No.99CH36306), pp. 10-15.

Warrier, G.R. and Dhir, V.K. 2006, "Heat Transfer and Wall Heat Flux Partitioning During Subcooled Flow Nucleate Boiling- A Review", J. of Heat Transfer, Vol.128, pp. 1243-1255.

White, F.M. 1991, "Viscous Fluid Flow", 2nd edition, Publisher: McGraw-Hill Science/Engineering/Math.

Wolf, D.H., Incropera, F.P. and Viskanta, R. 1993, "Jet Impingement Boiling", Advances in Heat Transfer, Vol. 23, pp. 1:132.

Wolf, D.H., Incropera, F.P. and Viskanta, R. 1996, "Local Jet Impingement Boiling Heat Transfer", Int. J. of Heat and Mass Transfer, Vol. 39, n. 7, pp. 1395:1406.

Woodfield, P.L., Monde, M and Mitsutake, Y. 2006, "Implementation Of An Analytical Two-Dimensional Inverse Heat Conduction Technique To Practical Problems", Int. J. Heat and Mass Transfer, Vol. 49, pp. 187:197.

Woodfield, P.L., Monde, M., and Mozumder, A.K. 2005, "Observations Of High Temperature Impinging-Jet Boiling Phenomena", Int. J. Heat and Mass Transfer, Vol. 48, pp. 2032:2041.

Yeoh, G.H. and Tu, J.Y. 2005, " Thermal-Hydrodynamic Modeling of Bubbly Flows with Heat and Mass Transfer", Fluid Mechanics and Transport Phenomena, Journal Review, Vol. 51, n.1, pp. 8:26.

Zeitoun, O. 1994, "Subcooled Flow Boiling and Condensation", Ph. D. Thesis, McMaster University, Hamilton, Ontario.

Zeng, L.Z., Klausner, J.F., Bernhard, D.M., and Mei, R. 1993, "A Unified Model for the Prediction of Bubble Detachment Diameter In Boiling Systems-II: Flow Boiling", Int. J. of Heat and Mass Transfer, Vol. 36, n. 9, pp. 2271-2279.

Zumbrunnen, D.A. 1991, "Convective Heat and Mass Transfer in the Stagnation Region of a Laminar Planar Jet Impinging on a Moving Surface", J. of Heat Transfer, Vol. 113, pp. 563:570.

APPENDIX A: Uncertainty Analysis

A.1. Wall Heat Flux

The uncertainty in the average wall flux at the flat surface is based on the 1D heat conduction analysis, Basu (2003):

$$q''_{w,avg} = -k_{cu}\frac{dT}{dy} \tag{A.1}$$

Where y is the normal distance from the heater surface and k_{cu} is the copper surface thermal conductivity.

The percentage uncertainty in the wall heat flux is estimated according to Moffat et al. (1985):

$$\frac{\varpi_{q_{w,avg}}}{q''_{w,avg}} = \sqrt{\left(\frac{\varpi_{k_{cu}}}{k_{cu}}\right)^2 + \left(\frac{\varpi_{\Delta y}}{\Delta y}\right)^2 + \left(\frac{\varpi_T}{T}\right)^2} \tag{A.2}$$

The uncertainty in the interior temperatures using high precession thermocouples is ±0.25 °C. For maximum attainable temperature of 150 °C the percentage uncertainty in the temperature becomes 0.17%. At lower values of the heat flux and interior temperature readings (e.g. T~100 °C) this percentage becomes 0.25%. A constant value of the copper thermal conductivity was used in the calculations as it varies within 3% of the maximum and minimum values over the operating temperature range. The uncertainty in the location of the thermocouples is ±2.54E-6m which is constant for all conditions and results in uncertainty percentage of 0.13%.

The above uncertainty values produced an average uncertainty of 3% in the average wall flux. This very low value of the uncertainty is due to the precise placement of the thermocouples that have also limited error band wires.

A.2. Surface Temperature

The data fit with a second degree polynomial of the interior temperature as shown in chapter 2 proven to coincide to the temperature profile at all conditions. Thus, the uncertainty of the extrapolated surface temperature is in accordance with that of the thermocouples readings at the interior locations, i.e.; ±0.25 °C.

A.3. Single Phase Heat Transfer Coefficient

The value of the experimental heat transfer coefficient is based upon the Newton's cooling law:

$$h = \frac{q_w''}{\Delta T} \tag{A.3}$$

So the percentage uncertainty in the calculated heat transfer coefficient is:

$$\frac{\varpi_h}{h} = \sqrt{\left(\frac{\varpi_{q_{w,avg}''}}{q_{w,avg}''}\right)^2 + \left(\frac{\varpi_{\Delta T}}{\Delta T}\right)^2} \tag{A.4}$$

The water temperature thermocouple has higher uncertainty (±0.5 °C) so the estimated uncertainty in the temperature difference is ±0.4 °C. For a range of the temperature difference between the wall and the liquid of 10-50 °C, this uncertainty range is highest at ±5% and drops to ±3.1%, respectively. Similar approach has been adopted by Basu (2003).

A.4. Bubble Release Frequency and Growth Time

Due to the large difference between the peak and base voltage levels of the optical probe signal, the uncertainty in the frequency value (number of peaks per unit time) is assumed to be less than 1%. However the width of this signal that reflects the bubble growth time varies according to the value of the voltage threshold. Thus an estimated uncertainty was determined from the difference in the growth time at voltage threshold of 0.15 and at 0.25. The average change in the growth time was ±15%.

A.5. Bubble Diameter

The actual dimensions of the focus area in the visual observation were 8 mm x 8 mm. the pixel size of the same focus area was 225 x 225 pixel. This means that one pixel represents 0.035 mm of the actual size. In other words, the resolution in determining the bubble diameter is 28 pixels/ mm. So, an error of two pixel, one on each side of the bubble perimeter, represents an error of 0.07 mm in the diameter. For the range of diameter values obtained from the visual observation, the uncertainty of the average bubble diameter ranges between ±4.6% for the bubble diameter of 1.5 mm and ±34% for bubble diameters of 0.2 mm.

A.6. Bubble Population

Based on the number counted of the bubbles within the focus area, the uncertainty in this parameter will be determined. When missing the counting of one bubble, the uncertainty will depend on the corresponding total number of bubbles. The uncertainty in the partial boiling regime is very high (~100%) for very low number of bubbles is observable. However when only few bubbles are being generated miscounting is highly unlikely. Conservative assumption of miscount has been adopted at low superheat such that the uncertainty has been estimated to be around ±30. Uncertainty in terms of the number of miscounted bubbles with respect to the total number of bubbles is expected to decrease with boiling intensity as the total number of bubbles increases. In fully developed boiling, uncertainty due to one bubble miscount can be as low as 0.4%. However, this is difficult to confirm as the number of missed counts increases with the increase of total number of bubbles and bubble merging in addition to the increased vapor generated at the film surface that degrades the resolution of the images. An estimate of ±25% uncertainty is suggested at high boiling intensity (in the fully developed boiling) as recommended in previous studies of PFB, e.g.: Basu (2003).